CONTROL AND FAULT TOLERANCE IMPROVEMENT OF THE CLASS OF MODULAR MULTILEVEL CONVERTERS

A Dissertation
Presented to
The Academic Faculty

By

Qichen Yang

In Partial Fulfillment
of the Requirements for the Degree
Doctor of Philosophy in the
School of Electrical and Computer Engineering

Georgia Institute of Technology

December 2018

CONTROL AND FAULT TOLERANCE IMPROVEMENT OF THE CLASS OF MODULAR MULTILEVEL CONVERTERS

Approved by:

Dr. Maryam Saeedifard, Advisor
School of Electrical and Computer Engineering
Georgia Institute of Technology

Dr. Thomas G. Habetler
School of Electrical and Computer Engineering
Georgia Institute of Technology

Dr. Lukas Graber
School of Electrical and Computer Engineering
Georgia Institute of Technology

Dr. A. P. Meliopoulos
School of Electrical and Computer Engineering
Georgia Institute of Technology

Dr. Mehdi Narimani
Department of Electrical and Computer Engineering
McMaster University

Dr. Santiago Carlos Grijalva
School of Electrical and Computer Engineering
Georgia Institute of Technology

Date Approved: November 1, 2018

To my Parents

ACKNOWLEDGEMENTS

I would like to express my sincere gratitude to my advisor, Professor Maryam Saeedifard. She is a great professor who cares about her students. Her patient guidance, insightful instructions, and enthusiastic encouragement supported and helped me significantly along the whole journey of my doctoral studies. It has been an honor and a pleasure to work with her. I appreciate all her contributions of precious time, stimulating ideas, and funding support during my Ph.D. experience.

I would like to thank Professor Thomas G. Habetler, Professor Lukas Graber, Professor A. P. Meliopoulos, Professor Mehdi Narimani, and Professor Santiago Carlos Grijalva for serving on my thesis committee and for their insightful comments and suggestions to my thesis. I am especially grateful to Professor Ronald Harley for his impressive and constructive comments to my dissertation proposal. I would like to thank Professor Lukas Graber again for his elaborate suggestions and friendly support in our collaborative research. I am also grateful to Dr. Ray Ridley for the insights and helpful instructions from the aspect of industry and Professor Dionysios Aliprantis for the impressive lectures and warm encouragement.

The members of the power groups have contributed immensely to my personal and professional time at both Georgia Tech and Purdue University. Special appreciation goes to Dr. Jiangchao Qin, Dr. Hao Chen, and Dr. Zhaoyu Wang for their insightful discussions and friendly help. I also would like to thank my friends Dr. Heng Yang, Dr. Chanyeop Park, Dr. Suman Debnath, Dr. Yi Deng, Dr. Minyu Cai, Dr. Nan Liu, Dr. Chen Jiang, Dr. Lijun He, Dr. Jie Dang, Sufei Li, Sheng Zhang, Cheng Gong, Liyao Wu, Jingfan Sun, Hang Shao, Xiangyu Han, Liran Zheng, Zheng An, Chunmeng Xu, Jia Wei, and Jingyuan Tian for their friendship and help.

I appreciate the unconditioned support and love from my parents. Although I cannot list all the people I appreciate, I do appreciate everybody who helped me.

TABLE OF CONTENTS

LIST OF TABLES

LIST OF FIGURES

LIST OF FIGURES

SUMMARY

The family of the modular multilevel converters (MMCs) has become the most promising class of converters for medium/high-power energy conversion systems, because of salient features including modularity, scalability, high efficiency, superior harmonic performance, easy realization of the redundancy, and absence of DC-link capacitors. The salient features of the MMCs can potentially be exploited for various applications at medium- and high-voltage levels including adjustable speed drives, solid-state transformers, grid integration of renewable energy resources, etc. However, for each application, unique operational and control challenges are imposed. As a result, unique control strategies and design considerations are required to guarantee proper operation of the MMCs, achieve high power density, efficiency, and reliability. Over the past decade, significant research has been performed to address the technical challenges associated with control and operation of various MMC topologies and to unveil their full promises. This thesis is in continuation of this endeavor.

On the control aspect, a sliding mode control-based method is proposed for the DC-AC MMC. Based on the analysis of system dynamics under the proposed control method, relations among the control parameters and their validity conditions are obtained, which provide a guidance for the systematic controller design. In addition, an active thermal loading control method is also proposed, where a multi-objective optimization problem is formulated and solved to establish a trade-off between the total power losses and the power loss of the semiconductor devices with the highest thermal loading. The Pareto optimal solutions determine the optimal values of the circulating currents, output common-mode voltage, and capacitor voltage reference.

On the reliability and fault-tolerance front, a clustering algorithm-based fault detection and locating method is proposed to detect the abnormal curve characteristics of any faulty submodule (SM) of a DC-AC MMC and pinpoint the faulty SM(s). Without any

additional sensor, the proposed method can accurately detect and locate the faulty SMs within a reasonable time. Subsequent to bypassing the faulty SMs, the maximum attainable terminal voltage of the faulty phase of the DC-AC MMC is reduced. To maximize the available output line-to-line voltages under the condition, a fault-tolerant control method based on adaption of the neutral-shift strategy and the supporting circulating current suppression method are proposed. For an AC-AC MMC, fault-tolerant control methods for external line-to-ground faults as well as internal SM faults are proposed. Under any external line-to-ground fault, the input-side current regulation, capacitor voltage balancing, and capacitor voltage fluctuation mitigation methods are redesigned to countermeasure the adverse impact of the negative-sequence voltage components in the input side. To address the internal SM fault, the SM capacitor voltages of the faulty cluster are modified to keep the voltage output capability of the faulty cluster.

To address the technical challenges associated with low-frequency operation of the DC-AC MMC, a hybrid MMC-derived topology along with its supporting control strategy are proposed to suppress the large SM capacitor voltage fluctuations without injecting any load-side common-mode voltage. In addition, an AC-AC MMC-based topology is developed to eliminate the large capacitor voltage ripple issue of the conventional AC-AC MMC and to enable the AC-AC MMC for partially-rated solid-state transformers.

CHAPTER 1
INTRODUCTION AND BACKGROUND

1.1 Background

The family of the modular multilevel converters (MMCs) has become the most promising class of converters for medium/high-power energy conversion systems [1, 2, 3]. Compared to other multilevel converter topologies, the salient features of the MMCs include: 1) modularity and scalability to meet any voltage level requirements, 2) high efficiency, which is of significant importance for high-power applications, 3) superior harmonic performance, specifically for high-voltage applications, where a large number of identical submodules (SMs) with low-voltage ratings are stacked up, thereby the size of passive filters can be reduced, 4) easy realization of the redundancy, and 5) absence of DC-link capacitors. Over the past decade, significant research has been performed to address the technical challenges associated with control and operation of various MMC-derived converter topologies and to broaden their applications.

1.2 Literature Survey

1.2.1 Relevant research on the DC-AC MMC

Figure. 1.1 shows the schematic diagram of a three-phase DC-AC MMC. The MMC consists of two arms per phase, where each arm comprises N series-connected, nominally identical, half-bridge SMs, and a series-connected inductor. The arm resistor models the power losses within each arm of the MMC [1]. In principle, each arm represents a controllable voltage source. By controlling those controllable voltage sources, i.e., the switching states of the SMs within each arm, the MMC outputs multilevel AC voltages [4, 5, 6, 7]. Similar to any other multilevel converter topology, the MMC needs an active voltage bal-

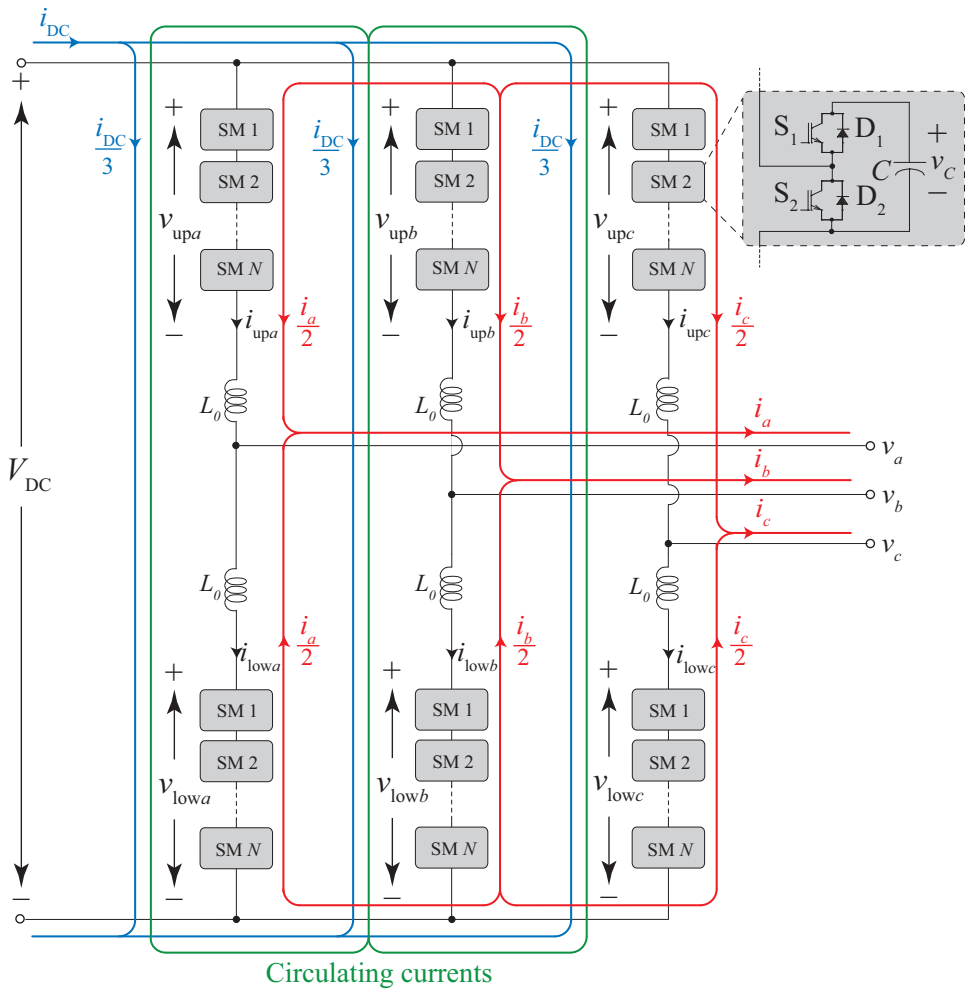

Figure 1.1: Schematic representation of a DC-AC MMC.

ancing strategy to balance and maintain the SM capacitor voltages at V_{dc}/N. The most widely accepted voltage balancing strategy is based on a sorting method [8, 9]. Over the past few years, extensive research has been done to address the technical challenges associated with the operation and control of the MMC and to improve its performance [10, 11, 12, 13, 14]. The most common applications of the MMC are the high-voltage DC transmission, flexible AC transmission controllers, and medium-voltage electric drive systems.

As illustrated in Fig. 1.1, currents in the MMC contain three components, i.e., AC-side output components (in red), DC-side output components (in blue), and circulating components (in green). Through its AC- and DC-side output components, the MMC exchanges real power, while the circulating currents only correspond to the internal power

flows within the three-phase legs of the MMC. For efficiency reason, circulating currents are either suppressed by an active circulating current control strategy [15, 16, 17, 18, 19, 20] or controlled as degrees of freedom for some specific objectives [21, 22, 23, 24, 25]. In addition to the circulating currents, another common degree of freedom in the MMC is the AC-side common-mode voltage.

In this section, the existing literature about the concerned topics of the thesis are reviewed, including the nonlinear control methods, active thermal loading control, open-circuit fault detection methods, fault-tolerant control methods, and hybrid topologies of the DC-AC MMC.

Nonlinear control methods for the DC-AC MMC

To effectively control the MMC, several control strategies based on classical linear controllers, e.g., proportional-integral (PI) and proportional-resonant (PR) controllers, have been proposed [26, 27, 28, 15, 29, 30, 18]. Although these controllers have been able to control the internal dynamics of the MMC, the nonlinear multi-input multi-output (MIMO) dynamics of the MMC with strong coupling among its states necessitates adoption of more advanced control strategies. Concomitantly, various nonlinear control strategies have been proposed and investigated, including direct and indirect model-based predictive control [31, 32, 33, 34], Lagrange multipliers-based optimized control [35], model-based input-output linearization [36], and feedback linearization [37, 38]. However, the existing nonlinear-controller-based strategies rely on the exact mathematical model of the system, which may not be necessarily available. Furthermore, the model-predictive control-based methods suffer from significant computational burden, which hinders their implementation in real time [31, 32, 33, 34].

Active thermal control of the MMC

Uneven power loss distribution and thermal loading among the semiconductor devices of each submodule (SM) compromise the reliability and lifetime of the converter [39, 40, 41, 42, 43]. Active thermal control is a promising method to manage the thermal loading and address the uneven power loss distribution among the semiconductor devices without any additional hardware [44]. The semiconductor power loss calculation, thermal loading, and lifetime and reliability issues of the MMC are presented in [45, 46], and circulating currents have been identified as a degree of freedom to control the temperature variations of the semiconductor devices [47]. Nevertheless, injecting the circulating currents improve the MMC performance only along a single objective, i.e., temperature variations of semiconductor devices while the overall power of the MMC is compromised.

Open-circuit fault detection methods for the DC-AC MMC

The most commonly adopted SM circuits for the MMCs are based on the half- and full-bridge circuit topologies consisting of wire-bound IGBT modules along with their corresponding anti-parallel diodes and a capacitor [1]. Consequently, an open-switch failure in any of the IGBT modules, which can be due to wire-bond lift-off or rupture, gate driver failure, or any other reason. [48, 49], distorts the voltage and current waveforms of the converter. In addition, an open-switch failure of an IGBT module may cause the capacitor voltage of the corresponding SM to continuously increase over time. Therefore, any open-switch failure should be detected and located so that the corresponding faulty SM can be bypassed as fast as possible. In the technical literature, switch failure detection of a power electronic converter has been investigated based on the following methods:

- Hardware-based/invasive methods in which the converter switching devices or the gate driving circuits are equipped with additional sensors. These methods have been mainly used for short-circuit/over-current protection of IGBTs [48, 50]. The short-circuit protection functions are integrated into commercial gate drivers, which in case of any short-circuit

detection, are capable of shutting down the IGBTs within a short period of time to protect the IGBTs and other components from the destructive damages [48, 49].

• Software-based/non-invasive methods in which the unique signature characteristics of either the converter waveforms or a set of pre-specified fault indicators are analyzed/processed to detect and locate the faulty switch [48, 49]. Since subsequent to an open-switch failure, the current and voltage waveforms of the faulty system become distorted, these methods are suitable for detecting open-switch failures [51, 52, 53, 54, 55, 56, 57, 58, 59, 60] and can be categorized into signal processing-based and model-based methods [48, 49]. In the signal processing-based methods, a set of concerned variables are analyzed and compared against their values/trajectories under normal conditions [52, 53, 54, 55, 56]. In the model-based methods, a mathematical model of the converter is developed. By comparison of the estimated values of fault indicator variables, which are estimated based on the developed mathematical model, and their corresponding measured values, a fault occurrence can be detected [57]. Although the methods for the conventional two-level voltage source converters and active neutral-point-clamped converters in [52, 53, 54] are capable of pinpointing specific location of the faulty switch, they are not applicable to advanced converter topologies such as the MMC. To detect open-switch switch failure(s) in a cascaded H-bridge converter, whose structure is similar to the MMC, a method based on analysis of the output voltage of each phase is proposed in [55]. However, its application is restricted to the phase-shifted carrier pulsewidth modulation strategy. The proposed neutral network-based method in [56] is not sufficiently accurate and requires a large diversity of training.

In the context of the MMC, a sliding mode observer (SMO) has been proposed and investigated to detect the faulty SMs [57]. The drawback of this method is its significant computational effort and complexity, which grows exponentially as the number of SMs increases. In [58], a Kalman filter is used to detect the faulty phase, and a method relying on the SM capacitor voltages is proposed to pinpoint the faulty SMs within the faulty phase. However, an inevitable delay time of Δt may affect the robustness and accuracy of

the method. In [61], a state observer is employed to detect the faulty arm, and a method depending on the SM capacitor voltages is developed to locate the single faulty SM. Nevertheless, the method is not suitable for multiple switch faults.

Fault-tolerant control of the DC-AC MMC

Subsequent to any SM failure, the faulty SM(s) must be bypassed using bidirectional switches at their output terminals [51]. Consequently, the maximum attainable terminal voltage of the faulty phase is reduced, resulting in voltage asymmetry, deteriorated power quality, and reduced power transfer capability.

A common practice in improving fault tolerance of the MMC and counteracting the adverse impact of any SM failure is to consider a number of redundant SMs within each arm of the MMC [62, 63]. Upon any SM failure, the faulty SMs are replaced by the redundant ones allowing the MMC to continue its normal conditions. In [64], an energy balancing control strategy is proposed to control the converter. In the strategy, subsequent to bypassing the faulty SMs, the capacitor voltages of the remaining healthy SMs of the faulty arm are increased, imposing more stress on the SM components. To enhance fault tolerance of the cascaded H-bridge converter, a neutral-shift strategy is proposed in [55, 65, 66, 67], which enables continued operation of the converter under faulty conditions. In the neutral-shift strategy, the phase angles of three-phase voltage references are appropriately displaced from 120° so that the attainable balanced line-to-line voltages are maximized.

Low-frequency operation of the DC-AC MMC

The MMC suffers from large SM capacitor voltage fluctuation under low output frequency operating conditions [21]. An effective solution to the problem is to inject circulating currents and a common-mode voltage to cancel the unbalanced low-frequency power among upper- and lower-arms [21, 22, 23, 24, 25]. However, the intentionally injected common-mode voltage will be imposed on motor winding, which may deteriorates the

winding insulation over time, leading to the premature failure of winding insulation. Additionally, the large common-mode voltage applying to the stray capacitor (between rotor and frame) may cause leakage current, which also bring negative effect to motor [68]. Methods that are independent of the common-mode voltage are also proposed and investigated [69, 70, 71, 72, 73, 74]. The method in [69] depends on proper adjustment of the SM capacitor voltage reference and fails when the output frequency is extremely low. In [71], a flying capacitor is added to provide an extra power path to balance the power between the upper and lower arms, which, however, could limit the output voltage range. The methods in [70, 73, 72] depends on extra full-bridge (FB)-based SM arms to provide extra power path to suppress large SM capacitor voltage fluctuations. In [74], an extra switch is added into the DC-link to remove unbalanced power between the upper and lower arms. However, the method in [74] is limited by a prerequisite that the magnitude of load-side sinusoidal voltage is proportional to the rotating frequency of the electric machine, i.e., a special $V - I$ characteristic of the load.

1.2.2 Overview of the research on the AC-AC MMC

Figure. 1.2 shows a schematic diagram of a three-to-three-phase AC-AC MMC. The AC-AC MMC consists of nine clusters, where each cluster comprises N series-connected, normally identical, full-bridge SMs, and a series-connected inductor. In principle, each cluster of the AC-AC MMC is manipulated as a controllable voltage source to shape the desired multilevel voltages.

Proper operation of the AC-AC MMC necessitates the SM capacitor voltages among the clusters to be balanced. The overall capacitor voltage can be controlled through regulating the input and/or output power of the converter, while the conventional sorting-based and pulse width modulation (PWM)-based voltage balancing methods still work within each cluster of the AC-AC MMC. The existing methods for the capacitor voltage balancing are based on the $\alpha\beta$-transformation [75, 76, 77, 78]. In [75], internal dynamics of the

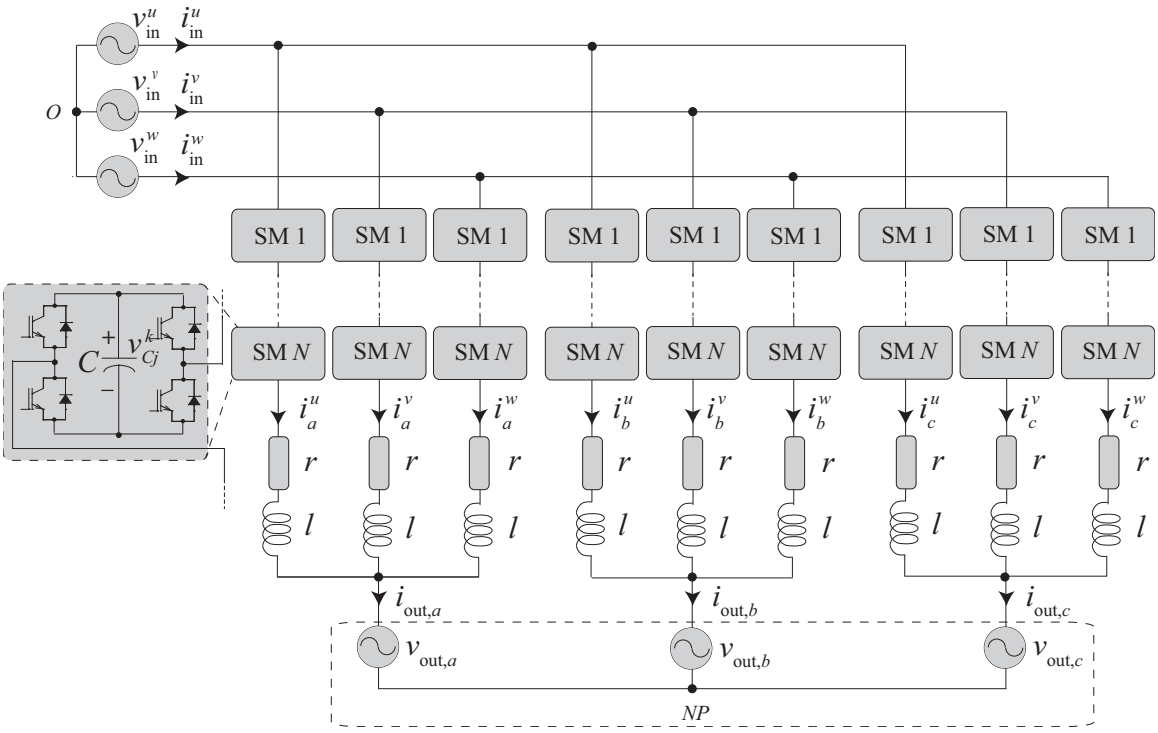

Figure 1.2: Schematic representation of a AC-AC MMC.

AC-AC MMC are described by a 3×3 differential equation matrix. Based on the double-$\alpha\beta$-frame, the cluster currents are categorized into three groups to control input-side power flow, output-side power flow, and power flow among the clusters separately. By injecting double-$\alpha\beta$-based circulating currents, the capacitor voltages among the clusters are maintained balanced. If the output-side frequency is close to the input-side frequency, the power of the clusters contain low-frequency components, causing large fluctuation of the SM capacitor voltages [79]. To mitigate the capacitor voltage fluctuations, circulating currents and/or a common-mode voltage are injected [79, 75, 80, 3, 81]. To suppress the voltage fluctuations when the frequencies of two sides are close, the "instantaneous power mode" is proposed in [79]. However, the voltage fluctuations become significantly pronounced when the output-side frequency is one third of the input-side frequency under the instantaneous power mode [75]. To solve the problem, reference [75] proposes a method, which adjusts not only instantaneous active power but also the instantaneous reactive power. Nevertheless, the method proposed in [75] fails when the frequencies of both sides are close [80].

Reference [80] proposes a method to regulate the input-side reactive power, such that the sum of the input-side and output-side reactive powers is zero. The method in [80] works under both the two aforementioned situations. In [81], reactive power of the output-side is adjusted to maintain the two sides reactive power opposite and a fluctuation mitigation method based on both circulating currents and common-mode voltage is proposed.

1.2.3 Research on the Partially-Rated Solid-State Transformer (PSST)

The increasing penetration rate of dynamic sources such as renewable energy resources together with the emergence of new dynamic loads such as electric vehicles, necessitate more flexible, efficient, and economical operation of the power grid. To maximize utilization of the power system infrastructure in an efficient and economical way, significant efforts have been made to actively control real and reactive power flows. To this end, among the proposed power electronics-based solutions, solid-state transformer (SST) has become one of the emerging technologies [82, 83, 84]. However, the application/deployment of SST has been limited due to high cost and reliability issues. To combine the flexibility provided by the power electronics and reliability of the conventional magnetic transformer, an alternative method, i.e., partially-rated solid-state transformer (PSST), has emerged [85], in which a power electronics converter is integrated into the conventional magnetic transformer. Even if the power electronics part of the PSST fails, the conventional magnetic transformer is still able to transfer power, thereby preserving the reliability aspect. Furthermore, since the majority portion of power in a PSST is still transfered by the main magnetic part, the power electronics part does not need to be fully rated. The power electronics part of a PSST can be realized by a DC-AC or an AC-AC converter [86, 87]. Since the AC-AC converter, including the back-to-back connected AC-DC-AC converter, has two AC ports, it is capable of simultaneously adjusting the voltage and current of the grid. Therefore, an AC-AC converter-based PSST can provide most functionalities including power flow control, voltage sag/swell compensation, and current harmonics filtering.

In [86], various possible configurations of the PSST are discussed. An optimized design of a PSST is presented in [87], with an emphasis on differential mode filter design. The direct matrix converter and buck-boost matrix-reactance choppers are integrated for the PSST in [88] and [89]. A modular transformer converter-based power flow controller is proposed in [90]. In [91], the power electronics module is auto-connected to the secondary-side of the line frequency transformer to compensate the voltage sags and swells. Design considerations, evaluation criteria, and some candidate topologies are provided in [92].

1.3 Summary of the Contribution

The research focuses on improving the performance of the DC-AC and AC-AC MMCs from the aforementioned aspects, which is summarized as summarized in the following:

- Proposed and verified a sliding mode control-based control method (Chapter 2);
- Proposed and verified an optimized control method to improve the thermal loading performance of the MMC (Chapter 3);
- Proposed and verified a clustering algorithm-based method to detect open-circuit faults in the active switches of the MMC (Chapter 4);
- Proposed and verified a neutral shift-based fault-tolerant method for the DC-AC MMC under any SM failure, as well as a control method for the AC-AC MMC under an external line-to-ground fault (Chapter 5);
- Proposed and verified a hybrid DC-AC MMC topology to enable low-frequency operation (Chapter 7);
- Proposed and verified an MMC-based partially-rated solid-state transformer to control the power flow (Chapter 8).

CHAPTER 2

SLIDING MODE CONTROL OF THE DC-AC MMC

In this chapter, a sliding mode control (SMC)-based method is proposed for the MMC. The SMC-based strategies have been applied to a wide range of electric drives and power converters [93, 94]. The basic idea of the SMC is to use references of controlled variables to divide the state space into several subspaces, where each subspace corresponds to a unique control structure. In each subspace, the unique control structure is applied to force the controlled variables to slide along the boundaries of the subspaces, i.e., references, which could provide excellent dynamic response. The proposed method, compared to the conventional linear controllers provides a faster dynamic response and comparable steady-state performance. Compared to the model predictive control-based method, it does not compromise the calculation burden or the requirement for precise system models. Based on analysis of system dynamics under the proposed control method, relations among control parameters and their validity conditions are obtained, which provide a guidance for systematic controller design. Simulation studies in the PSCAD/EMTDC software environment are carried out to validate the performance and effectiveness of the proposed control method.

2.1 Dynamics of the MMC

The circuit diagram of a three-phase MMC is shown in Fig. 2.1. The MMC consists of two arms per phase where each arm is comprised of N series-connected, nominally identical half-bridge (HB) SMs and a series-connected arm inductor. Dynamics of the

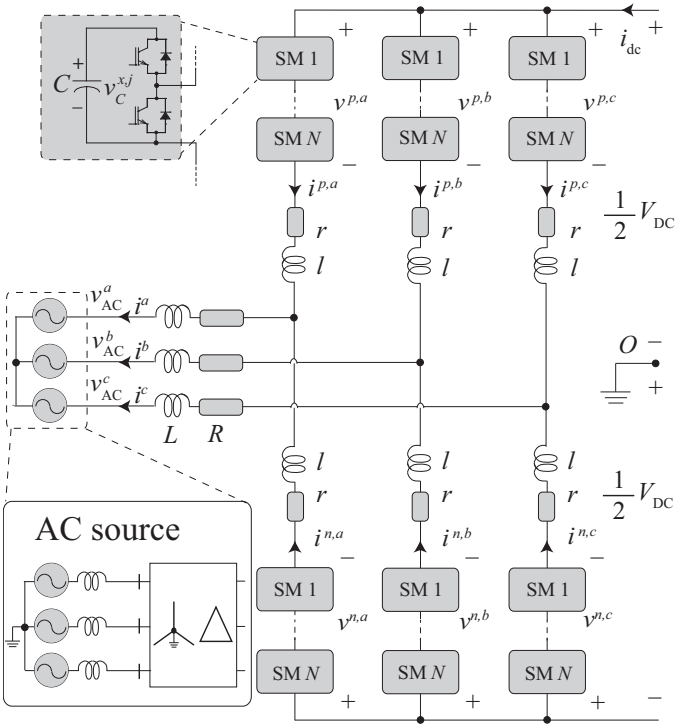

Figure 2.1: Circuit diagram of the DC-AC MMC.

MMC can be summarized by [17, 95]:

$$
\begin{aligned}
\tfrac{1}{2}V_{\mathrm{dc}} - n^{p,j}v_C^{p,j} - ri^{p,j} - l\tfrac{di^{p,j}}{dt} - Ri^{j} - L\tfrac{di^{j}}{dt} - (V_{\mathrm{AC}}\sin(\theta-\phi^{j}) + v_{\mathrm{AC}}^{0}) = 0,\\
-\tfrac{1}{2}V_{\mathrm{dc}} - n^{n,j}v_C^{n,j} - ri^{n,j} - l\tfrac{di^{n,j}}{dt} - Ri^{j} - L\tfrac{di^{j}}{dt} - (V_{\mathrm{AC}}\sin(\theta-\phi^{j}) + v_{\mathrm{AC}}^{0}) = 0,\\
C\tfrac{dv_C^{p,j}}{dt} = \tfrac{n^{p,j}}{N}i^{p,j},\\
C\tfrac{dv_C^{n,j}}{dt} = -\tfrac{n^{n,j}}{N}i^{n,j},
\end{aligned}
\tag{2.1}
$$

where $n^{x,j}$, $i^{x,j}$, and $v_C^{x,j}$ are the number of inserted SMs, current, and equivalent SM capacitor voltage in the x arm of phase j ($x = p, n$ and $j = a, b, c$), V_{dc} is the DC-link voltage, V_{AC} is the peak value of line-to-neutral voltage of the AC voltage source, i^{j} is the phase j current, v_{AC}^{0} is the zero-sequence component of the AC-side terminal voltages, and ϕ^{j} is the phase angle of the phase j of the AC voltage source. In this section, $v_{\mathrm{AC}}^{0,\mathrm{ref}}$ is assumed to

be zero. Generally, the control inputs are obtained based on

$$\begin{aligned} n^{p,j}v_C^{p,j} - n^{n,j}v_C^{n,j} &\approx \left(n^{p,j} - n^{n,j}\right) V_C^{\text{ref}} \triangleq f\left(\cdot\right) + h_{\text{com}}\left(\cdot\right), \\ n^{p,j}v_C^{p,j} + n^{n,j}v_C^{n,j} &\approx \left(n^{p,j} + n^{n,j}\right) V_C^{\text{ref}} \triangleq g\left(\cdot\right) + h_{\text{dif}}, \end{aligned} \tag{2.2}$$

where V_C^{ref} is the capacitor voltage reference, $f\left(\cdot\right)$ is the function to control the AC-side currents of the MMC, $g\left(\cdot\right)$ is the function to control the circulating currents of the MMC, $h_{\text{com}}\left(\cdot\right)$ is the feed-forward component to control the AC-side currents of the MMC, h_{dif} is the fed-forward component to control the circulating currents of the MMC. Common- and differential-mode components are defined as:

$$\begin{bmatrix} z_{\text{com}}^j \\ z_{\text{dif}}^j \end{bmatrix} \triangleq \frac{1}{2} \begin{bmatrix} 1 & 1 \\ 1 & -1 \end{bmatrix} \begin{bmatrix} z^{p,j} \\ z^{n,j} \end{bmatrix}, \tag{2.3}$$

where z_{com}^j is the common-mode component of $z^{p,j}$ and $z^{n,j}$, and z_{dif}^j is the differential-mode component of $z^{p,j}$ and $z^{n,j}$ ($z^{x,j}$ is the general designation of $i^{x,j}$, $v_C^{x,j}$, and $n^{x,j}$). Based on (2.3), i_{com}^j is half of i^j. Substituting (2.2) and (2.3) for $i^{p,j}$, $i^{n,j}$, $n^{p,j}$, $n^{n,j}$, $v_C^{p,j}$ and $v_C^{n,j}$ in (2.1) yields

$$\frac{d}{d\theta} \begin{bmatrix} i_{\text{com}}^j \\ i_{\text{dif}}^j \\ v_{C,\text{com}}^j \\ v_{C,\text{dif}}^j \end{bmatrix} = \begin{bmatrix} A_{11} & A_{12} \\ A_{21} & A_{22} \end{bmatrix} \begin{bmatrix} i_{\text{com}}^j \\ i_{\text{dif}}^j \\ v_{C,\text{com}}^j \\ v_{C,\text{dif}}^j \end{bmatrix} - \begin{bmatrix} \frac{v_{\text{AC}}^j}{\omega L_{\text{AC}}} \\ -\frac{V_{\text{dc}}}{2\omega l} \\ 0 \\ 0 \end{bmatrix}, \tag{2.4}$$

where L_{AC} equals to $2L + l$, R_{AC} equals to $2R + r$,

$$
\begin{aligned}
A_{11} &= \begin{bmatrix} -\frac{R_{\mathrm{AC}}}{\omega L_{\mathrm{AC}}} & 0 \\ 0 & -\frac{r}{\omega l} \end{bmatrix}, \\
A_{12} &= \begin{bmatrix} -\frac{n^j_{\mathrm{dif}}}{\omega L_{\mathrm{AC}}} & \frac{n^j_{\mathrm{com}}}{\omega L_{\mathrm{AC}}} \\ \frac{n^j_{\mathrm{com}}}{\omega l} & -\frac{n^j_{\mathrm{dif}}}{\omega l} \end{bmatrix}, \\
A_{21} &= \frac{1}{\omega NC} \begin{bmatrix} n^j_{\mathrm{dif}} & -n^j_{\mathrm{com}} \\ -n^j_{\mathrm{com}} & n^j_{\mathrm{dif}} \end{bmatrix}, \\
A_{22} &= 0,
\end{aligned}
\tag{2.5}
$$

and

$$n^j_{\mathrm{dif}} = \frac{f^j(\cdot) + h^j_{\mathrm{com}}(\cdot)}{2V_C^{\mathrm{ref}}}, \tag{2.6a}$$

$$n^j_{\mathrm{com}} = \frac{g^j(\cdot) + h^j_{\mathrm{dif}}}{2V_C^{\mathrm{ref}}}. \tag{2.6b}$$

2.2 The Proposed Sliding Mode Control

In the proposed SMC-based method, common- and differential-mode currents are actively controlled and two control structures are designed for each actively-controlled variable. The two control structures are applied alternatively for a certain time length, i.e., Δt, to force the corresponding variable to slide along the boundary of the two structures within a hysteresis range, i.e., $\pm\Delta i^j_{\mathrm{com}}$ or $\pm\Delta i^j_{\mathrm{dif}}$.

2.2.1 Single-phase MMC

Since a single-phase MMC has only one phase, the superscript j of variables is removed in the following analysis. To control i_{com} and i_{dif} in a single-phase MMC, each of $f(\cdot)$ and

$g(\cdot)$ in (2.2) corresponds to two structures, i.e.,

$$f(\cdot) = F\mathrm{sgn}\left(i_{\mathrm{com}} - i_{\mathrm{com}}^{\mathrm{ref}}\right) = F\mathrm{sgn}\left(e_{\mathrm{com}}\right), \tag{2.7a}$$

$$g(\cdot) = G\mathrm{sgn}\left(i_{\mathrm{dif}} - i_{\mathrm{dif}}^{\mathrm{ref}}\right) = G\mathrm{sgn}\left(e_{\mathrm{dif}}\right), \tag{2.7b}$$

where F and G are the magnitudes of the commended excitations, e_{com} is the error between i_{com} and its reference, and e_{dif} is the error between i_{dif} and its reference. Based on (2.7), the two structures within each pair alternate based on comparison between actively-controlled currents and their references. Besides, to generate n_{com}^{j} and n_{dif}^{j}, the feed-forward components in (2.2) are

$$\begin{aligned} h_{\mathrm{com}}(\cdot) &= -2V_{\mathrm{AC}}\sin(\theta), \\ h_{\mathrm{dif}} &= -V_{\mathrm{DC}}. \end{aligned} \tag{2.8}$$

In a well-designed MMC, the magnitudes of ripple components of each SM capacitor voltage are regulated within a limited range, i.e.,

$$\begin{aligned} -\Delta v_{C,\mathrm{com}} \le v_{C,\mathrm{com}} - V_C^{\mathrm{ref}} \le \Delta v_{C,\mathrm{com}}, \\ -\Delta v_{C,\mathrm{dif}} \le v_{C,\mathrm{dif}} \le \Delta v_{C,\mathrm{dif}}, \end{aligned} \tag{2.9}$$

where $\Delta v_{C,\mathrm{com}}$ and $\Delta v_{C,\mathrm{dif}}$ are the magnitudes of the ripples in $v_{C,\mathrm{com}}$ and $v_{C,\mathrm{dif}}$, and

$$\begin{bmatrix} v_{C,\mathrm{com}} \\ v_{C,\mathrm{dif}} \end{bmatrix} = \frac{1}{2}\begin{bmatrix} 1 & 1 \\ 1 & -1 \end{bmatrix}\begin{bmatrix} v_C^p \\ v_C^n \end{bmatrix}. \tag{2.10}$$

A typical scenario is that the controlled variable, i.e., i_{com} is forced from the upper boundary of the hysteresis range to the lower boundary of the hysteresis range within one Δt, e.g.,

$$\begin{aligned} i_{\mathrm{com}}(\theta_0) &= i_{\mathrm{com}}^{\mathrm{ref}}(\theta_0) + \Delta i_{\mathrm{com}}, \\ i_{\mathrm{com}}(\theta_0 + \Delta\theta) &= i_{\mathrm{com}}^{\mathrm{ref}}(\theta_0 + \Delta\theta) - \Delta i_{\mathrm{com}}, \end{aligned} \tag{2.11}$$

where Δi_{com} is the magnitude of the ripple in i_{com}, and $\Delta\theta$ is $\omega\Delta t$. In the scenario, substi-

tuting (2.6a), (2.7a), (2.8), and (2.9) for n_{com}, n_{dif}, $v_{C,\mathrm{com}}$, and $v_{C,\mathrm{dif}}$ in (2.4) yields

$$\frac{di_{\mathrm{com}}}{d\theta} = -\frac{R_{\mathrm{AC}}}{\omega L_{\mathrm{AC}}} i_{\mathrm{com}} - \frac{1}{2\omega L_{\mathrm{AC}}} U_{\mathrm{com}}, \tag{2.12}$$

where

$$U_{\mathrm{com}} = F \pm \frac{\Delta v_{C,\mathrm{com}} F}{V_C^{\mathrm{ref}}} \mp \frac{\Delta v_{C,\mathrm{com}} v_{\mathrm{AC}}}{V_C^{\mathrm{ref}}} \mp \frac{\Delta v_{C,\mathrm{dif}} (\pm G + V_{\mathrm{DC}})}{V_C^{\mathrm{ref}}}. \tag{2.13}$$

Based on (2.13), the range of U_{com} is

$$F - \epsilon_{\mathrm{com}} \leq U_{\mathrm{com}} \leq F + \epsilon_{\mathrm{com}}, \tag{2.14}$$

where

$$\epsilon_{\mathrm{com}} = \frac{\Delta v_{C,\mathrm{com}} \left(F + V_{\mathrm{AC}}\right) + \Delta v_{C,\mathrm{dif}} \left(G + V_{\mathrm{DC}}\right)}{V_C^{\mathrm{ref}}}. \tag{2.15}$$

In a well-designed MMC, $\Delta v_{C,\mathrm{com}}$ and $\Delta v_{C,\mathrm{dif}}$ are much smaller than $V_{C,\mathrm{ref}}$. Therefore, ϵ_{com} is much smaller than F, i.e.,

$$\epsilon_{\mathrm{com}} \ll F. \tag{2.16}$$

Furthermore, (2.12) is approximately equivalent to

$$\frac{di_{\mathrm{com}}}{d\theta} \approx -\frac{R_{\mathrm{AC}}}{\omega L_{\mathrm{AC}}} i_{\mathrm{com}} - \frac{F}{2\omega L_{\mathrm{AC}}}. \tag{2.17}$$

Solving (2.17) for i_{com} yields

$$i_{\mathrm{com}}(\theta) = i_{\mathrm{com}}(\theta_0) \exp\left(-\tfrac{R_{\mathrm{AC}}}{\omega L_{\mathrm{AC}}}(\theta - \theta_0)\right) + \tfrac{F}{2R_{\mathrm{AC}}}\left(\exp\left(-\tfrac{R_{\mathrm{AC}}}{\omega L_{\mathrm{AC}}}(\theta - \theta_0)\right) - 1\right). \tag{2.18}$$

By substituting (2.11) into (2.18) for $i_{\mathrm{com}}(\theta)$ and $i_{\mathrm{com}}(\theta_0)$ and reorganizing the equation, (2.18) can be transformed into

$$\exp\left(-\tfrac{R_{\mathrm{AC}}}{\omega L_{\mathrm{AC}}}\Delta\theta\right) = \tfrac{2R_{\mathrm{AC}}\left(i_{\mathrm{com}}^{\mathrm{ref}}(\theta_0+\Delta\theta) - \Delta i_{\mathrm{com}}\right)+F}{2R_{\mathrm{AC}}\left(i_{\mathrm{com}}^{\mathrm{ref}}(\theta_0)+\Delta i_{\mathrm{com}}\right)+F}, \tag{2.19}$$

where

$$i_{\mathrm{com}}^{\mathrm{ref}}(\theta) = I_{\mathrm{com}}^{\mathrm{ref}} \sin\left(\theta + \phi_{I,\mathrm{com}}^{\mathrm{ref}}\right), \tag{2.20}$$

$I_{\mathrm{com}}^{\mathrm{ref}}$ is the magnitude of $i_{\mathrm{com}}^{\mathrm{ref}}$, and $\phi_{I,\mathrm{com}}^{\mathrm{ref}}$ is the phase angle of $i_{\mathrm{com}}^{\mathrm{ref}}$. Expanding $\exp\left(-\frac{R_{\mathrm{AC}}}{\omega L_{\mathrm{AC}}}\Delta\theta\right)$ in (2.19) into Taylor-series yields

$$\exp\left(-\frac{R_{\mathrm{AC}}}{\omega L_{\mathrm{AC}}}\Delta\theta\right) \approx 1 - \frac{R_{\mathrm{AC}}}{\omega L_{\mathrm{AC}}}\Delta\theta, \tag{2.21}$$

where the validity condition to remove the high-order terms in (2.21) is

$$\frac{1}{2}\left(\frac{R_{\mathrm{AC}}}{\omega L_{\mathrm{AC}}}\Delta\theta\right)^2 \ll 1. \tag{2.22}$$

Linearizing $\sin\left(\theta + \phi_{I,\mathrm{com}}^{\mathrm{ref}}\right)$ in (2.20) around θ_0 based on Taylor series yields

$$i_{\mathrm{com}}^{\mathrm{ref}}(\theta_0 + \Delta\theta) \approx i_{\mathrm{com}}^{\mathrm{ref}}(\theta_0) + I_{\mathrm{com}}^{\mathrm{ref}} \cos\left(\theta_0 + \phi_{I,\mathrm{com}}^{\mathrm{ref}}\right)\Delta\theta, \tag{2.23}$$

where the validity condition of the linearization is

$$I_{\mathrm{com}}^{\mathrm{ref}} \left|\sin(\theta_0)\right| \frac{\Delta\theta^2}{2} \ll I_{\mathrm{com}}^{\mathrm{ref}} \left|\sin(\theta_0)\right| \left(\text{i.e., } \frac{\Delta\theta^2}{2} \ll 1\right). \tag{2.24}$$

Substituting (2.20), (2.21), and (2.23) in (2.19) and simplifying, the relation among F, Δt, and Δi_{com} can be obtained as:

$$\Delta t = \frac{2\Delta i_{\mathrm{com}}}{\frac{F}{L_{\mathrm{AC}}} + \omega I_{\mathrm{com}}^{\mathrm{ref}} \cos\left(\theta_0 + \phi_{I,\mathrm{com}}^{\mathrm{ref}}\right) + \frac{R_{\mathrm{AC}}}{L_{\mathrm{AC}}} i_{\mathrm{com}}^{\mathrm{ref}}(\theta_0)} \approx \frac{2L_{\mathrm{AC}}\Delta i_{\mathrm{com}}}{F}. \tag{2.25}$$

The validity condition of the approximation in (2.25) is

$$F \gg I_{\mathrm{com}}^{\mathrm{ref}} \sqrt{(\omega L_{\mathrm{AC}})^2 + (R_{\mathrm{AC}})^2}. \tag{2.26}$$

Similarly, another typical scenario is that the controlled variable, i.e., i_{dif} is forced from

the upper boundary of the hysteresis range to the lower boundary of the hysteresis range within one Δt,

$$\begin{aligned} i_{\mathrm{dif}}(\theta_0) &= i_{\mathrm{dif}}^{\mathrm{ref}}(\theta_0) + \Delta i_{\mathrm{dif}}, \\ i_{\mathrm{dif}}\left(\theta_0 + \Delta\theta\right) &= i_{\mathrm{dif}}^{\mathrm{ref}}(\theta_0 + \Delta\theta) - \Delta i_{\mathrm{dif}}, \end{aligned} \tag{2.27}$$

where Δi_{dif} is the magnitude of ripple components of i_{dif}. In this scenario, dynamics of i_{dif} can be expressed as:

$$\frac{di_{\mathrm{dif}}}{d\theta} \approx -\frac{r}{l} i_{\mathrm{dif}} - \frac{U_{\mathrm{dif}}}{2\omega l}, \tag{2.28}$$

where

$$G - \epsilon_{\mathrm{dif}} \leq U_{\mathrm{dif}} \leq G + \epsilon_{\mathrm{dif}} \tag{2.29}$$

and

$$\epsilon_{\mathrm{dif}} = \frac{\Delta v_{C,\mathrm{com}}\left(G + V_{\mathrm{DC}}\right) + \Delta v_{C,\mathrm{dif}}\left(F + V_{\mathrm{AC}}\right)}{V_C^{\mathrm{ref}}} \ll G. \tag{2.30}$$

Since ϵ_{dif} is much smaller than G, (2.28) is approximately equivalent to

$$\frac{di_{\mathrm{dif}}}{d\theta} \approx -\frac{r}{l} i_{\mathrm{dif}} - \frac{G}{2\omega l}. \tag{2.31}$$

Solving (2.31) for i_{dif} yields

$$\begin{aligned} i_{\mathrm{dif}}\left(\theta\right) = i_{\mathrm{dif}}\left(\theta_0\right) &\exp\left(-\tfrac{r}{\omega l}\left(\theta - \theta_0\right)\right) \\ &+ \tfrac{G}{2r}\left(\exp\left(-\tfrac{r}{\omega l}\left(\theta - \theta_0\right)\right) - 1\right). \end{aligned} \tag{2.32}$$

To remove high-order terms of the Taylor series of the exponential terms in (2.32), a validity condition is needed:

$$\frac{1}{2}\Big(\frac{r}{\omega l}\Delta\theta\Big)^2 \ll 1. \tag{2.33}$$

Expanding the exponential terms of (2.32) into Taylor series and removing high-order

terms, relation among G, Δt, and $\Delta i_{\rm dif}$ is

$$\Delta t = \frac{2l\Delta i_{\rm dif}}{r\left(i_{\rm dif}^{\rm ref} + \Delta i_{\rm dif}\right) + G} \approx \frac{2l\Delta i_{\rm dif}}{G}, \tag{2.34}$$

where the validity condition of the approximate equation is

$$G \gg r i_{\rm dif}^{\rm ref}. \tag{2.35}$$

2.2.2 Three-phase MMC

In a three-phase MMC, the three-phase circulating currents are independent. Therefore, $g(\cdot)$ and $h_{\rm dif}(\cdot)$ of a three-phase MMC are the same as those of a single-phase MMC in (2.7), i.e.,

$$g^j\left(\cdot\right) = G{\rm sgn}\left(i_{\rm dif}^j - i_{\rm dif}^{j,{\rm ref}}\right) = G{\rm sgn}\left(e_{\rm dif}^j\right), \tag{2.36a}$$

$$h_{\rm dif}^j = -V_{\rm DC}. \tag{2.36b}$$

However, dynamics of three-phase $i_{\rm com}^j$ is different from that in a single-phase MMC as the three-phase currents are not independent. Therefore, $f(\cdot)$ and $h_{\rm com}(\cdot)$ of a three-phase MMC need to be modified based on the dq transformation by

$$\begin{bmatrix} n_{\rm dif}^a \\ n_{\rm dif}^b \\ n_{\rm dif}^c \end{bmatrix} = \frac{1}{2V_C^{\rm ref}} \begin{bmatrix} f^a\left(\cdot\right) \\ f^b\left(\cdot\right) \\ f^c\left(\cdot\right) \end{bmatrix} + \frac{1}{2V_C^{\rm ref}} \begin{bmatrix} h_{\rm com}^a \\ h_{\rm com}^b \\ h_{\rm com}^c \end{bmatrix}, \tag{2.37}$$

where

$$\begin{aligned}
\begin{bmatrix} f^a(\cdot) \\ f^b(\cdot) \\ f^c(\cdot) \end{bmatrix} &= -T^{-1} \begin{bmatrix} f^q(\cdot) \\ f^d(\cdot) \end{bmatrix}, \\
\begin{bmatrix} h^a_{\mathrm{com}} \\ h^b_{\mathrm{com}} \\ h^c_{\mathrm{com}} \end{bmatrix} &= -2 \begin{bmatrix} v^a_{\mathrm{AC}} \\ v^b_{\mathrm{AC}} \\ v^c_{\mathrm{AC}} \end{bmatrix} - \tfrac{4\sqrt{3}\omega L_{\mathrm{AC}}}{3} \begin{bmatrix} 0 & -1 & 1 \\ 1 & 0 & -1 \\ -1 & 1 & 0 \end{bmatrix} \begin{bmatrix} i^a_{\mathrm{com}} \\ i^b_{\mathrm{com}} \\ i^c_{\mathrm{com}} \end{bmatrix},
\end{aligned} \tag{2.38}$$

and

$$f^{\xi}(\cdot) = F\mathrm{sgn}\left(i^{\xi} - i^{\xi,\mathrm{ref}}\right) \quad (\xi = q, d). \tag{2.39}$$

A typical scenario of controlling the three-phase line currents is that both i^d_{com} and i^q_{com} are at their upper boundary of hysteresis range,

$$\begin{aligned}
i^q_{\mathrm{com}} &= I^{q,\mathrm{ref}}_{\mathrm{com}} + \Delta i^q_{\mathrm{com}}, \\
i^d_{\mathrm{com}} &= I^{d,\mathrm{ref}}_{\mathrm{com}} + \Delta i^d_{\mathrm{com}},
\end{aligned} \tag{2.40}$$

where i^{ξ}_{com} is the ξ-axis component of i^j_{com}, $I^{\xi,\mathrm{ref}}_{\mathrm{com}}$ is the references of i^{ξ}_{com}, and $\Delta i^{\xi}_{\mathrm{com}}$ is the magnitude of ripple components of i^{ξ}_{com}. In this scenario, line current of phase a is

$$i^a_{\mathrm{com}} = \left(I^{q,\mathrm{ref}}_{\mathrm{com}} + \Delta i^q_{\mathrm{com}}\right)\cos(\theta) + \left(I^{d,\mathrm{ref}}_{\mathrm{com}} + \Delta i^d_{\mathrm{com}}\right)\sin(\theta). \tag{2.41}$$

Meanwhile, physical significance of the approximation in (2.17) and (2.31) is that $\Delta v_{C,\mathrm{com}}$ and $\Delta v_{C,\mathrm{dif}}$ are significantly smaller than V^{ref}_C in a well-designed MMC. Therefore, the excitations to control the currents, i.e., U_{com} and U_{dif}, are dominated by F and G, which means that ϵ_{com} and ϵ_{dif} are negligible. Substituting (2.36), (2.37), and (2.41) for $g^j(\cdot)$, h^j_{dif}, n^j_{dif}, and i^a_{com} in (2.4) and repeating the approximation in Section 2.2.1, dynamics of i^a_{com}

in the typical scenario is

$$\frac{d}{d\theta}i^a_{\rm com} = -\frac{R_{\rm AC}}{\omega L_{\rm AC}}i^a_{\rm com} + \frac{\sqrt{3}}{3}\left(-i^b_{\rm com} + i^c_{\rm com}\right) - \frac{F}{2\omega L_{\rm AC}}\left(\cos\left(\theta\right) + \sin\left(\theta\right)\right). \tag{2.42}$$

Expressing $i^j_{\rm com}$ with $i^d_{\rm com}$ and $i^q_{\rm com}$ based on dq transformation, the dynamics of $i^a_{\rm com}$ in (2.42) can be decoupled into

$$\begin{aligned} \tfrac{d}{d\theta}i^d_{\rm com} &\approx -\tfrac{R_{\rm AC}}{\omega L_{\rm AC}}i^d_{\rm com} - \tfrac{F}{2\omega L_{\rm AC}}, \\ \tfrac{d}{d\theta}i^q_{\rm com} &\approx -\tfrac{R_{\rm AC}}{\omega L_{\rm AC}}i^q_{\rm com} - \tfrac{F}{2\omega L_{\rm AC}}. \end{aligned} \tag{2.43}$$

Solving for $i^q_{\rm com}$ and $i^d_{\rm com}$ based on (2.43) and simplifying the results based on approximations result in

$$\Delta\theta = \frac{2\omega L_{\rm AC}\Delta i^\xi_{\rm com}}{F + R_{\rm AC}\left(I^{\xi,\rm ref}_{\rm com} + \Delta i^\xi_{\rm com}\right)} \approx \frac{2\omega L_{\rm AC}\Delta i^\xi_{\rm com}}{F}. \tag{2.44}$$

The validity conditions of (2.44) are

$$V^{\rm ref}_C \gg \Delta v_{C,\rm dif}, \Delta v_{C,\rm com}, \tag{2.45a}$$

$$\tfrac{1}{2}\left(\tfrac{R_{\rm AC}}{\omega L_{\rm AC}}\Delta\theta\right)^2 \ll 1, \tag{2.45b}$$

$$F \gg R_{\rm AC}\left(I^{\xi,\rm ref}_{\rm com} + \Delta i^\xi_{\rm com}\right), \tag{2.45c}$$

where (2.45a) guarantees that F and G are dominant in $U_{\rm com}$ and $U_{\rm dif}$ and the equations in (2.43) are valid, (2.45b) keeps that exponential terms of the solution of (2.43) can be removed, and (2.45c) guarantees the validity of the approximate equation of (2.44). To guarantee the validity conditions of (2.16), (2.30), and (2.45a), the SM capacitance, C, needs to be sufficiently large to limit the magnitude of the ripple components. Since the impedances of the inductors, i.e., $\omega L_{\rm AC}$ and ωl, are usually much larger than the corresponding resistances, $R_{\rm AC}$ and r, the validity conditions of (2.22), (2.33), and (2.45b) hold true in general.

Since the current references, i.e., i^{ξ}_{com} and i^{j}_{dif}, can be regarded to be constant in steady state, by combining (2.36a), (2.39), (2.31), and (2.43), dynamics of the controlled variables is summarized to be:

$$\frac{d}{d\theta}\mathbf{e} = -\frac{1}{\omega}\mathbf{B}\mathbf{i} - \frac{1}{2\omega}\mathbf{C}\text{sgn}(\mathbf{e}), \tag{2.46}$$

where

$$\begin{aligned}\mathbf{B} &= \text{diag}\left(\tfrac{R_{\text{AC}}}{L_{\text{AC}}}, \tfrac{R_{\text{AC}}}{L_{\text{AC}}}, \tfrac{r}{l}, \tfrac{r}{l}, \tfrac{r}{l}\right), \\ \mathbf{C} &= \text{diag}\left(\tfrac{F}{L_{\text{AC}}}, \tfrac{F}{L_{\text{AC}}}, \tfrac{G}{l}, \tfrac{G}{l}, \tfrac{G}{l}\right).\end{aligned} \tag{2.47}$$

The implementation block diagram of the proposed SMC-based method for a three-phase MMC is summarized in Fig. 2.2.

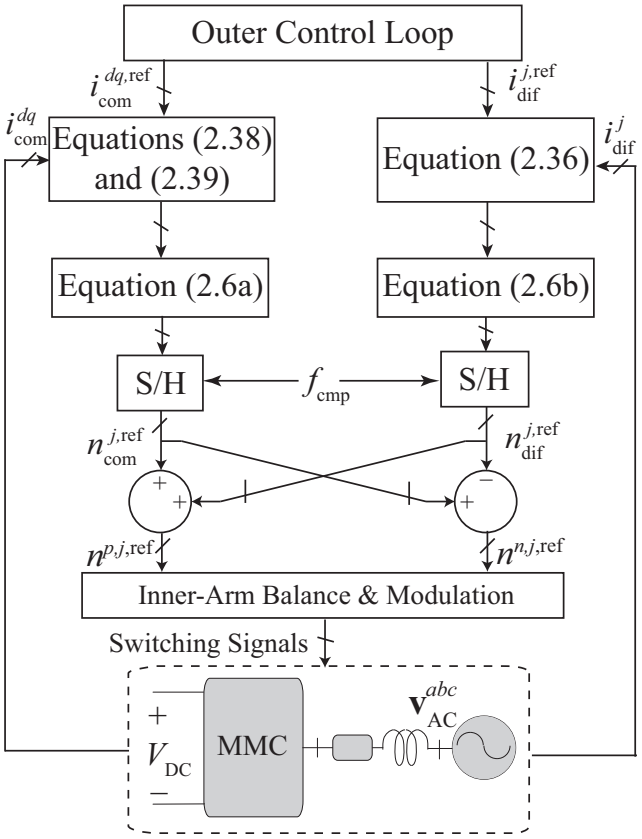

Figure 2.2: Block diagram of the proposed SMC-based method.

2.2.3 Fixed-frequency comparison

To prevent gating signals varying too frequently, $i^{\xi}_{\rm com}$ and $i^{j}_{\rm dif}$ are compared with their references at a fixed frequency, i.e., $f_{\rm cmp}$. Since the fixed frequency comparison could create a time-variable asymmetrical hysteresis range, the hysteresis range can be twice of those in (2.34) and (2.44). Therefore, considering (2.34) and (2.44), the fixed frequency is designed based on

$$f_{\rm cmp} \geq \max\left\{\frac{F}{L_{\rm AC}\Delta i^{\xi}_{\rm com}}, \frac{G}{l\Delta i^{\xi}_{\rm dif}}\right\}. \tag{2.48}$$

In addition, Δt should be sufficiently small to guarantee that the feed-forward components, i.e., $h^{j}_{\rm com}(\cdot)$ in (2.8) and (2.38) follow the sinusoidal variables in the plant closely. If one line period is divided into K divisions, the error can be estimated by $\sin(\frac{2\pi}{K})$. To limit the error within $0.5V^{\rm ref}_{C}$, the following requirement should be satisfied:

$$\sin(\frac{2\pi}{K}) = \sin\left(\frac{\omega}{f_{\rm cmp}}\right) < \frac{0.5V^{\rm ref}_{C}}{V_{\rm AC}}. \tag{2.49}$$

Therefore, another requirement to select $f_{\rm cmp}$ is:

$$f_{\rm cmp} > \arcsin\left(\frac{0.5\omega V_{\rm AC}}{V^{\rm ref}_{C}}\right) \approx \frac{0.5\omega V_{\rm AC}}{V^{\rm ref}_{C}}. \tag{2.50}$$

For a single-phase MMC, an extra requirement for Δt is to keep validity of (2.21) and (2.23). Maximum error between left and right sides of (2.23) is $\cos\left(\frac{\pi}{2} - \frac{\pi}{K}\right)\frac{2\pi}{K}$, which should satisfy its requirement. Besides, since $R_{\rm AC}$ is typically much smaller than $\omega L_{\rm AC}$, (2.21) and its validity condition, i.e., (2.22) will be satisfied in most cases if other requirements are reached.

Subsequent to determination of $f_{\rm cmp}$, $\Delta i^{\xi}_{\rm com}$ and $\Delta i^{j}_{\rm dif}$ are

$$\begin{aligned} \Delta i^{\xi}_{\rm com} &= \tfrac{F}{f_{\rm cmp}L_{\rm AC}}, \\ \Delta i^{j}_{\rm dif} &= \tfrac{G}{f_{\rm cmp}l}. \end{aligned} \tag{2.51}$$

Based on (2.51), under the fixed-frequency comparison, inductances $L_{\rm AC}$ and l, are inversely proportional to the current ripples. Therefore, if the actual inductances are larger than the theoretical values, the current slopes and ripples within each Δt are smaller than the designed values.

If the nearest-level modulation [96] is applied to an HVDC system, the average switching frequency, i.e., $f_{\rm sw}$ is lower than the execution frequency of inner-arm capacitor voltage balancing algorithm, i.e., $f_{\rm bal}$. Several methods to reduce the switching frequency have been proposed [97, 98]. In addition, $f_{\rm bal}$ can be lower than $f_{\rm cmp}$ as well. Therefore, $f_{\rm sw}$ can be reduced to hundreds of Hertz while $f_{\rm cmp}$ is thousands of Hertz, which satisfies both the low switching frequency and low current distortion requirements.

2.2.4 Comparison with the conventional PI-based control method

In the conventional PI-based control strategy, $K_{\rm I}$ is designed based on $R_{\rm AC}$, $L_{\rm AC}$, and $K_{\rm P}$:

$$R_{\rm AC}/L_{\rm AC} = K_{\rm I}/K_{\rm P}, \tag{2.52}$$

to cancel a pole at $s = -R_{\rm AC}/L_{\rm AC}$ [99]. Based on this principle, zero-state response of $i^{\xi}_{\rm com}$ to a step change of $i^{\xi,\rm ref}_{\rm com}$ from 0 to $I^{\xi,\rm ref,new}_{\rm com}$ is illustrated in (2.53), while the response of $i^{\xi}_{\rm com}$ under the proposed SMC-based control is illustrated in (2.54).

$$i^{\xi}_{\rm com} = \left(1 - \exp\left(-\frac{2K_{\rm P}t}{L_{\rm AC}}\right)\right) I^{\xi,\rm ref,new}_{\rm com} \tag{2.53}$$

$$i^{\xi}_{\rm com} \approx \frac{Ft}{2L_{\rm AC}} \tag{2.54}$$

To prevent over-modulation under a step-up change of $i^{q,\rm ref}_{\rm com}$ from $I^{q,\rm ref,pre}_{\rm com}$ to $I^{q,\rm ref,new}_{\rm com}$, $K_{\rm P}$ in the PI-based method and F^q in the SMC-based method are constrained by the following

upper limits:

$$F^q_{\max} \approx \sqrt{(0.575V_{\rm DC})^2 - (F^d)^2} - \left(V^q_{\rm AC} - \omega L_{\rm AC} I^{d,\rm ref}_{\rm com}\right), \tag{2.55a}$$

$$K_{\rm P,max} \approx \frac{\sqrt{(0.575V_{\rm DC})^2 - \left(V^{d,\rm ref}_{\rm tmn}\right)^2} - \left(V^q_{\rm AC} - \omega L_{\rm AC} I^{d,\rm ref}_{\rm com}\right)}{I^{q,\rm ref,new}_{\rm com} - I^{q,\rm ref,pre}_{\rm com}}, \tag{2.55b}$$

where

$$V^{d,\rm ref}_{\rm tmn} = \left(R_{\rm AC} I^{d,\rm ref}_{\rm com} + \omega L_{\rm AC} I^{q,\rm ref,pre}_{\rm com}\right). \tag{2.56}$$

Based on (2.53), as $i^{\xi}_{\rm com}$ converges $I^{\xi,\rm ref,new}_{\rm com}$, the convergence speed decreases exponentially under the PI-based control method. On the other hand, based on (2.54), under the proposed SMC-based method, decay rate of the error is a constant, which is not impacted by the difference between $i^{\xi}_{\rm com}$ and its reference. Meanwhile, based on (2.55b), $K_{\rm P,max}$ is inversely proportional to the step change magnitude, which also limits the speed of dynamic response of the PI-based control with large $\Delta I^{\xi}_{\rm com}$. On the contrary, $F_{\max}$ is not impacted by the step change magnitude. Therefore, the proposed SMC-based control can provide a higher speed of dynamic response over the conventional PI-based control.

2.2.5 Modifications of the proposed SMC-based control

Although a large F can potentially increase the speed of response during transients, the large excitation causes large current ripple during steady state based on (2.51). To solve the problem, an enhanced SMC-based method with variable F is proposed:

$$F = \begin{cases} F_{\max}, & \left|i^{\xi}_{\rm com} - i^{\xi,\rm ref}_{\rm com}\right| > i^{\xi,\rm thd}_{\rm com} \\ F_{\rm steady}, & \left|i^{\xi}_{\rm com} - i^{\xi,\rm ref}_{\rm com}\right| \le i^{\xi,\rm thd}_{\rm com} \end{cases}, \tag{2.57}$$

where

$$i^{\xi,\rm thd}_{\rm com} \triangleq \eta \frac{F_{\rm steady}}{L_{\rm AC} f_{\rm cmp}}. \tag{2.58}$$

In (2.57), $F_{\max}$ is designed by (2.55a), F^{steady} is designed based on (2.51), and η is slightly larger than one.

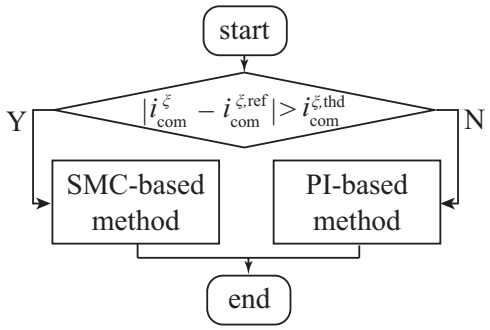

Figure 2.3: Hybrid control based on the PI- and SMC-based strategies.

Since the most significant advantage of the SMC-based method over the conventional PI-based method is its faster dynamic response, the proposed SMC-based method could be combined with the conventional PI-based method. As illustrated in Fig. 2.3, the SMC-based method is applied when large errors between currents and their references are detected.

Based on (2.46), R_{AC} and r of the system could result in a static error, since the resistive term in (2.46) always force $\mathbf{e}$ to the negative direction when the controlled currents are close to their references. In addition, since R_{AC} and r are small and depend on many factors in any certain application, obtaining the exact values of R_{AC} and r and removing the impact by applying feed-forward control signals is not straightforward. Therefore, if the impact of the resistive term cannot be neglected, the proposed SMC-based method needs to be modified to remove the static error. The most straightforward method is to apply large F and G to guarantee that the resistive term in (2.46) is much smaller than F and G. However, the too large excitation could create too large magnitude of current ripples based on (2.51). In addition, applying integral parts is another solution. For example, one integral part can be added into the sign functions of (2.36a) and (2.39), i.e.,

$$\begin{aligned} f^{\xi}(\cdot) &= F\text{sgn}\left(e^{\xi}_{\text{com}} + K_{\text{I,com}} \int e^{\xi}_{\text{com}} d\theta\right), \\ g^{j}(\cdot) &= G\text{sgn}\left(e^{j}_{\text{dif}} + K_{\text{I,dif}} \int e^{j}_{\text{dif}} d\theta\right). \end{aligned} \tag{2.59}$$

Dynamics of the system under the control function in (2.59) can be summarized as

$$\frac{d}{d\theta}\mathbf{e} = -\frac{1}{\omega}\mathbf{B}\mathbf{i} - \frac{1}{2\omega}\mathbf{C}\mathrm{sgn}(\mathbf{e} + \mathbf{K}_{\mathrm{I1}}\int \mathbf{e}d\theta), \tag{2.60}$$

where

$$\mathbf{K}_{\mathrm{I1}} = \mathrm{diag}\left(K_{\mathrm{I,com1}}, K_{\mathrm{I,com1}}, K_{\mathrm{I,dif1}}, K_{\mathrm{I,dif1}}, K_{\mathrm{I,dif1}}\right). \tag{2.61}$$

Besides, the integral part can be added to the right side of (2.46) directly, i.e.,

$$\tfrac{d}{d\theta}\mathbf{e} = -\tfrac{1}{\omega}\mathbf{B}\mathbf{i} - \tfrac{1}{2\omega}\mathbf{C}\mathrm{sgn}(\mathbf{e}) - \mathbf{K}_{\mathrm{I2}}\textstyle\int \mathbf{e}d\theta, \tag{2.62}$$

where

$$\mathbf{K}_{\mathrm{I2}} = \mathrm{diag}\left(K_{\mathrm{I,com2}}, K_{\mathrm{I,com2}}, K_{\mathrm{I,dif2}}, K_{\mathrm{I,dif2}}, K_{\mathrm{I,dif2}}\right). \tag{2.63}$$

Control functions that correspond to (2.62) are:

$$\begin{aligned} f^{\xi}(\cdot) &= F\mathrm{sgn}\left(e^{\xi}_{\mathrm{com}}\right) + K_{\mathrm{I,com}}\textstyle\int e^{\xi}_{\mathrm{com}}d\theta, \\ g^{j}(\cdot) &= G\mathrm{sgn}\left(e^{j}_{\mathrm{dif}}\right) + K_{\mathrm{I,dif}}\textstyle\int e^{j}_{\mathrm{dif}}d\theta. \end{aligned} \tag{2.64}$$

2.3 Simulation Results

To demonstrate performance and effectiveness of the proposed control method, a three-phase MMC is simulated in the PSCAD/EMTDC software environment. Parameters of the study system are listed in Table 2.1 and the control system is designed based on (2.48), (2.55), and (2.57). The nearest-level modulation method and slow-rate balancing strategy in [97] are applied to generate gating signals. The average switching frequency is 420$\sim$440 Hz, which is sufficiently low for HVDC transmission systems. Steady-state waveforms under the proposed SMC-based method are provided in Fig. 2.4(a)-(c). The setpoints of real and reactive powers are 30 MW and -20 MVAr, respectively, where $i^{q,\mathrm{ref}}$ and $i^{d,\mathrm{ref}}$ are 0.816 kA and 0.544 kA. Based on Figs. 2.4(a)-(c), q- and d-components of line

Table 2.1: Parameters of the study system

Rating Value	Value
Nominal power of the MMC converter	50 MW
AC system nominal voltage $V_{\mathrm{in,ll,rms}}$	30 kV
Nominal frequency of ac system f	60 Hz
DC link voltage V_{DC}	60 kV
Reference of SM capacitor voltage V_C^{ref}	1.5 kV
MMC Parameter	**Value**
L	11 mH
R	0.03 Ω
Series-connected inductance l	8 mH
Resistance of series-connected inductor r	0.02 Ω
Number of SMs in each cluster N	40
Submodule capacitor C	14000 μF
Control Parameter	**Value**
F^{steady} in (2.51)	1.8 kV
G in (2.51)	1.5 kV
f_{cmp} in (2.51)	12 kHz
f_{bal}	600 Hz
f_{sw}	420˜440 Hz

currents and circulating currents are well regulated at their references under the proposed SMC-based method. Table 2.2 presents magnitudes of ripple components of i^{ξ} and i^{j}_{dif}, which are closely matched with their theoretical values in (2.51). In Fig. 2.4(d), responses of i^{q} to the step change of its reference under PI- and SMC-based methods are compared, where $i^{q,\mathrm{ref}}$ steps up from 0 to 0.816 kA at $t = 0.25$ s and $i^{d,\mathrm{ref}}$ remains to be 0.544 kA, and SCR is infinity. Fig. 2.4(d) illustrates that the SMC-based method can improve the dynamic response of i^{q}. Speed of the responses under different grid stiffnesses are compared in Table 2.3, which presents that the proposed SMC-based method can shorten the rising time (from 10% $\Delta I^{q,\mathrm{ref}}$ to 90% $\Delta I^{q,\mathrm{ref}}$) by about 50%, compared with the conventional PI-based method.

Fig. 2.5 illustrates the dynamic response of the variables in the MMC to a step change of $i^{q,\mathrm{ref}}$ from 0 to 0.816 kA at $t = 0.17$ s, while $i^{d,\mathrm{ref}}$ remains to be 0.544 kA and SCR is equal to 2.5. Fig. 2.5(a) shows that d-axis component of line currents is kept decoupled from its q-axis component of line currents. As illustrated in Fig. 2.5(b), the three-phase

line currents are well-regulated. Fig. 2.5(c) illustrates that the line-to-line voltages at AC terminal of the MMC recover to be a balanced sinusoidal set within 3 ms. In addition, Fig. 2.5(d) shows that the currents of the six arms are controlled as expected, where the second-order components are suppressed. As illustrated in Fig. 2.5(e), the average SM capacitor voltages of the six arms are also well-regulated. SM capacitor voltages of the upper arm of phase a are presented in Fig. 2.5(f), which illustrates that the SM capacitor voltages are kept balanced with the slow-rate balancing strategy.

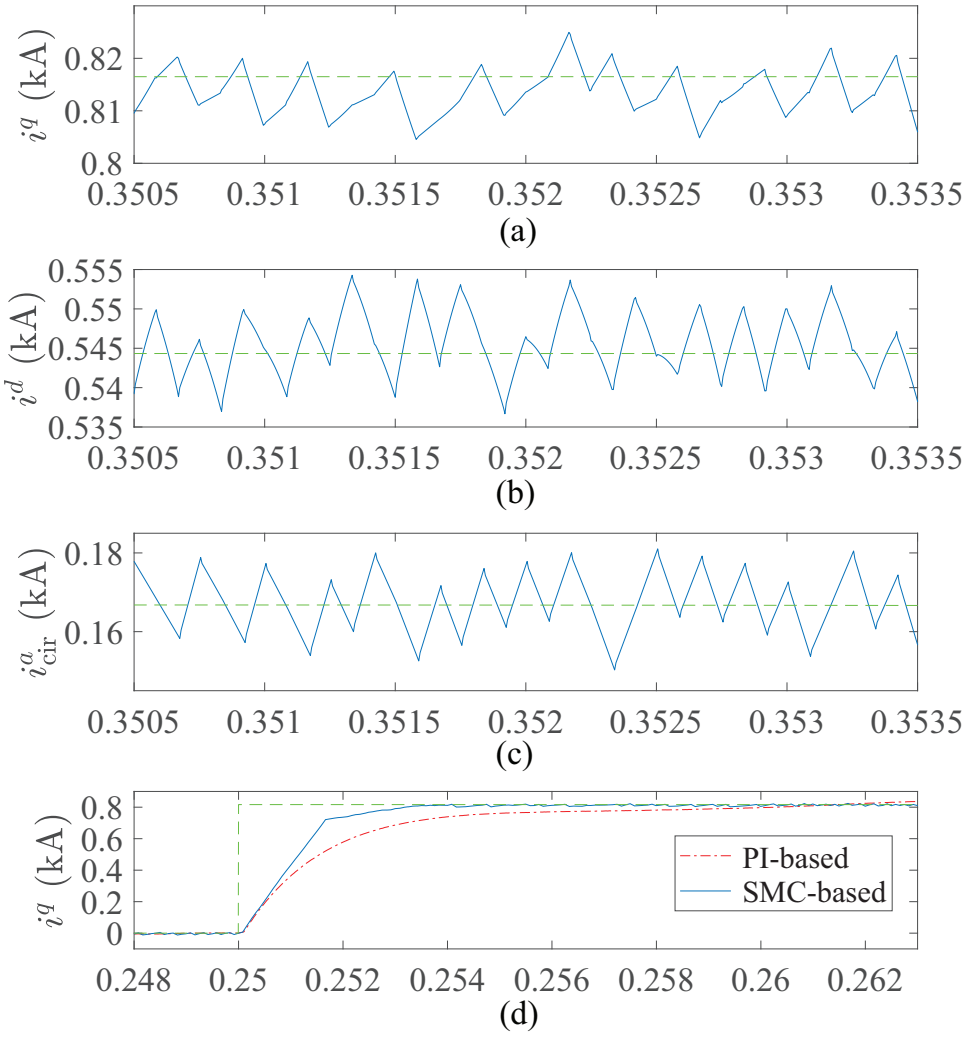

Figure 2.4: MMC waveforms under the proposed sliding mode control: (a) q-axis component of line currents in steady state and its reference, (b) d-axis component of line currents in steady state and its reference, (c) circulating current of phase a in steady state and its reference, (d) response of q-axis component of line currents to a step change of its reference.

Table 2.2: Magnitude of ripple components of i^{ξ} and i^{j}_{dif}

	i^{d} ($2i^{d}_{\mathrm{com}}$)	i^{q} ($2i^{q}_{\mathrm{com}}$)	i^{a}_{dif}
Simulation-based $\lvert\Delta i\rvert$ (kA)	0.012	0.011	0.015
Theoretical $\lvert\Delta i\rvert$ (kA)	0.010	0.010	0.016

Table 2.3: Rising time of i^{q} (from 10% $\Delta I^{q,\mathrm{ref}}$ to 90% $\Delta I^{q,\mathrm{ref}}$) under different SCRs

SCR	PI	SMC	Improvement
∞ (ideal)	3.65 ms	1.51 ms	58.6%
10 (stiff)	4.00 ms	1.66 ms	58.5%
4 (medium)	4.14 ms	2.11 ms	49.0%
2.5 (weak)	4.41 ms	2.20 ms	50.1%

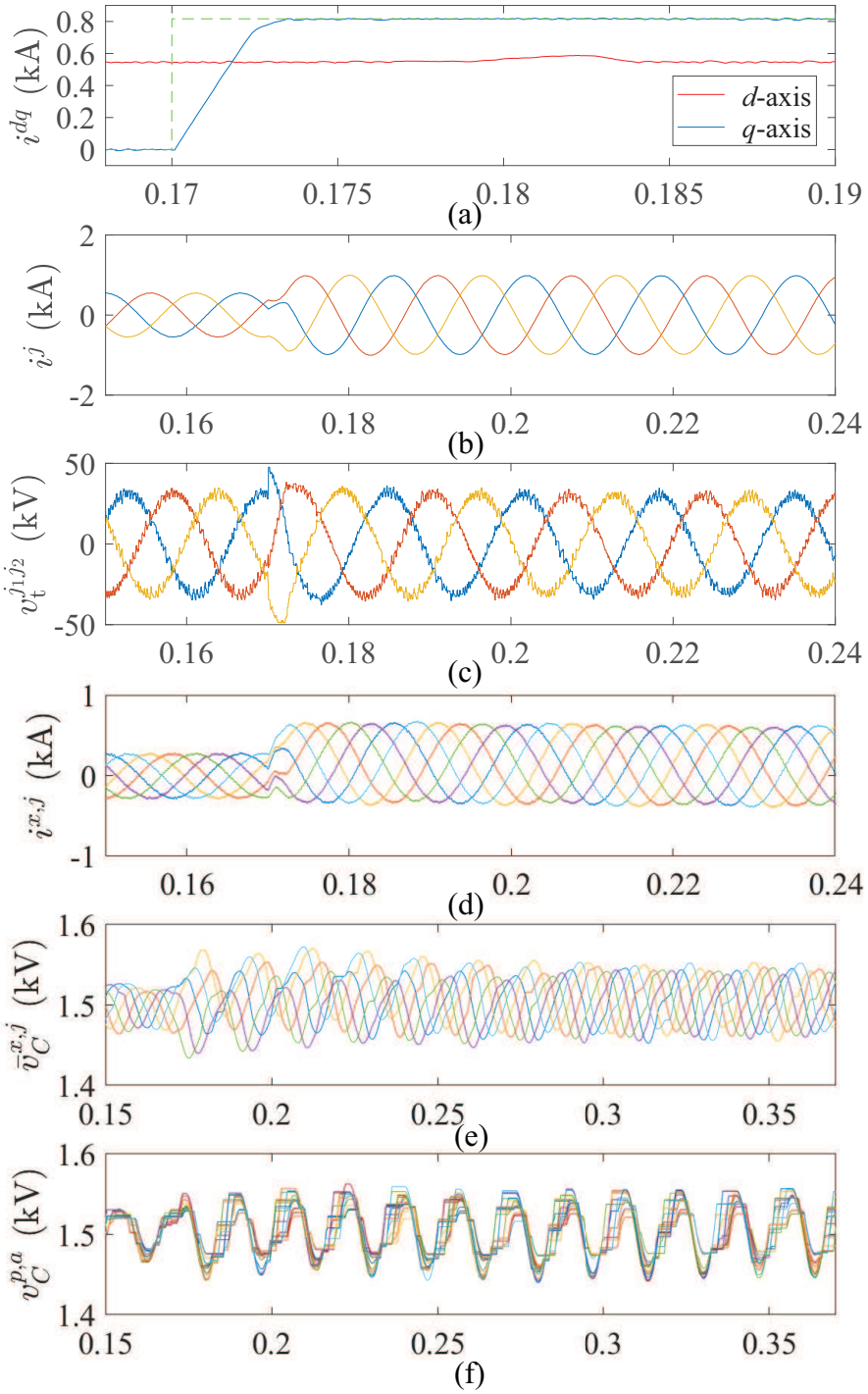

Figure 2.5: Response of the MMC to a step change of $i^{q,\mathrm{ref}}$ under the proposed sliding mode control (SCR = 2.5): (a) q- and d-axis components of the line currents, (b) three-phase line currents, (c) line-to-line voltages at AC terminal of the MMC, (d) arm currents of phase a, b, and c, (e) average SM capacitor voltages of phases a, b, and c, and (f) SM capacitor voltages in the arm p of phase a.

CHAPTER 3

THERMAL LOADING CONTROL OF THE DC-AC MMC

In this chapter, an active thermal loading control method is proposed for control of the MMC to simultaneously (i) minimize the total semiconductor power losses and (ii) balance the thermal loading of the semiconductor devices of each SM. In the proposed method, a multi-objective optimization problem is formulated and solved to establish a trade-off between the total power losses and the power losses of the semiconductor devices with the highest thermal loading. The Pareto optimal solutions determine the optimal value for the circulating currents, output common-mode voltage, and capacitor voltages. Performance and effectiveness of the proposed method are evaluated based on simulation studies in the PLECS software.

3.1 Control of the MMC

Figure 3.1 shows a schematic diagram of a three-phase grid-connected MMC. The AC-side currents of the MMC can be controlled using the conventional proportional-integral (PI)-based decoupled qd-current control [8]. The arm currents, voltages and power as well as the SM capacitor voltages of each phase-leg are decomposed into common- and differential-mode components:

$$\begin{bmatrix} z^{j}_{\mathrm{com}} \\ z^{j}_{\mathrm{dif}} \end{bmatrix} = \frac{1}{2} \begin{bmatrix} 1 & 1 \\ 1 & -1 \end{bmatrix} \begin{bmatrix} z^{p,j} \\ z^{n,j} \end{bmatrix}, \tag{3.1}$$

where $z^{x,j}$ can represent the arm power ($p^{x,j}$), arm voltage ($v^{x,j}$) and its reference ($v^{x,j,\mathrm{ref}}$), arm current ($i^{x,j}$) and its reference ($i^{x,j,\mathrm{ref}}$), and averaged SM capacitor voltage ($v_C^{x,j}$).

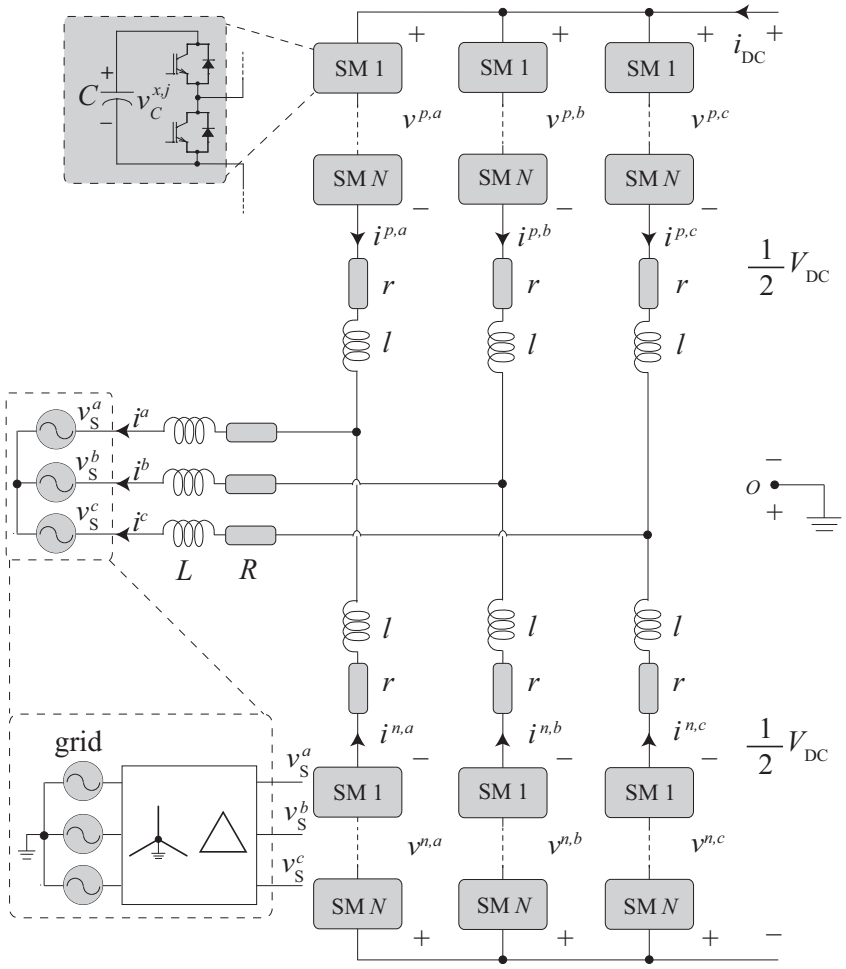

Figure 3.1: Circuit diagram of the DC-AC MMC.

Based on (3.1),

$$p^j_{\text{com}} = v^j_{\text{com}} i^j_{\text{com}} + v^j_{\text{dif}} i^j_{\text{dif}}, \tag{3.2a}$$

$$p^j_{\text{dif}} = v^j_{\text{com}} i^j_{\text{dif}} + v^j_{\text{dif}} i^j_{\text{com}}. \tag{3.2b}$$

By expressing $v_C^{x,j}$ as

$$v_C^{x,j} = \frac{1}{NCV_C^{\text{ref}}} \int p^{x,j} dt \tag{3.3}$$

and substituting for $p^j_{\rm com}$ and $p^j_{\rm dif}$ from (3.1) in (3.3),

$$v^j_{C,\rm com} = \tfrac{1}{NCV^{\rm ref}_C} \int p^j_{\rm com} dt, \tag{3.4a}$$

$$v^j_{C,\rm dif} = \tfrac{1}{NCV^{\rm ref}_C} \int p^j_{\rm dif} dt. \tag{3.4b}$$

Based on (3.2a) and (3.4a), since $v^j_{\rm dif}$ is close to $\frac{1}{2}V_{\rm DC}$, a DC component can be injected into $i^j_{\rm dif}$ to rectify $v^j_{C,\rm com}$. Similarly, based on (3.2b) and (3.4b), since $v^j_{\rm com}$ is close to a sinusoidal waveform, an in-phase AC component can be injected into $i^j_{\rm dif}$ to suppress $v^j_{C,\rm dif}$. Therefore,

$$\begin{aligned} i^{j,\rm ref}_{\rm dif} = {} & i^{j,\rm ref}_{\rm cir,inj} + \tfrac{P^{\rm ref}}{3V_{\rm DC}} + v^{j,\rm ref}_{\rm dif} \left(K_{\rm P1} + \tfrac{K_{\rm I1}}{s}\right) \left(LP_1\left(v^j_{C,\rm com}\right) - V^{\rm ref}_C\right) \\ & - v^{j,\rm ref}_{\rm com} \left(K_{\rm P2} + \tfrac{K_{\rm I2}}{s}\right) LP_2\left(v^j_{C,\rm dif}\right), \end{aligned} \tag{3.5}$$

where $i^{j,\rm ref}_{\rm cir,inj}$ is the desired circulating current component that needs to be injected to optimize the power loss and thermal loading distribution in each SM. In steady state, since the DC component of v^j_C is very close to $V^{\rm ref}_C$, $i^{j,\rm ref}_{\rm dif}$ is dominated by $i^{j,\rm ref}_{\rm cir,inj}$.

The overall control system of the MMC is summarized in Fig. 3.2, where circulating currents, output common-mode voltage, and SM capacitor voltages can be adjusted. The inner-arm balanced and modulation method is described in [100], which is based on PWM.

3.2 Semiconductor Power Loss Model of the MMC

Semiconductor conduction losses are calculated based on

$$\begin{aligned} P_{\rm cd,S} &= \left(v_{\rm ceo} + R_{\rm on,S} i_{\rm c}\right) i_{\rm c}, \\ P_{\rm cd,D} &= \left(v_{\rm fo} + R_{\rm on,D} i_{\rm f}\right) i_{\rm f}, \end{aligned} \tag{3.6}$$

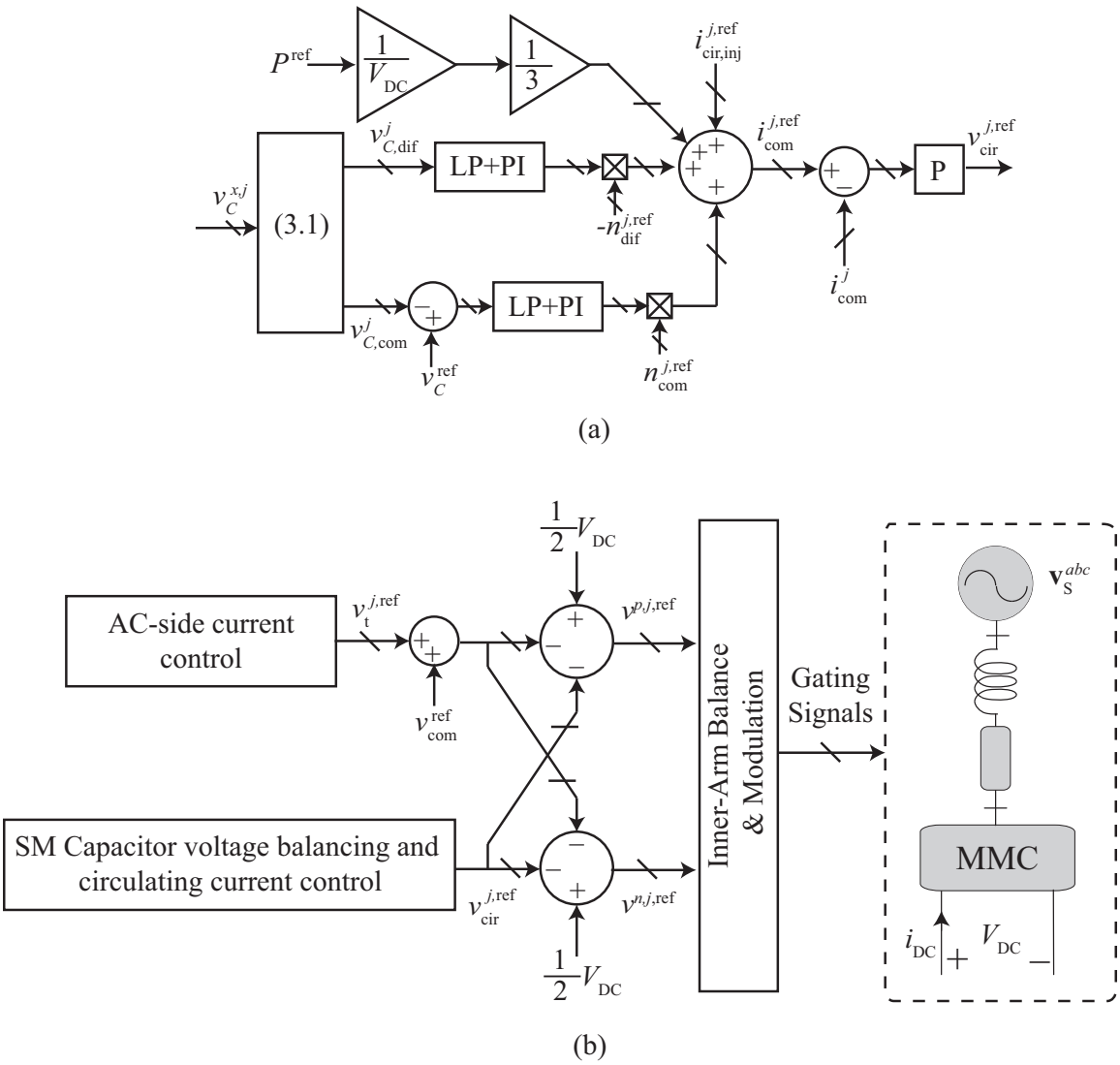

Figure 3.2: Block diagram of the: (a) SM capacitor voltage balancing and circulating current control, and (b) overall control strategy.

where $v_{\rm ceo}$ is the IGBT on-state zero-current collector-emitter voltage, $R_{\rm on,S}$ is the IGBT on-state resistance, $v_{\rm fo}$ is the diode on-state zero-current forward voltage, and $R_{\rm on,D}$ is the diode on-state resistance, $i_{\rm c}$ is the collector current of the IGBT and $i_{\rm f}$ is the forward current of the diode. The switching loss of the IGBT and the reverse-recovery power loss of the diode are calculated based on

$$\begin{aligned} E_{\rm sw,S} &= (E_{\rm on} + E_{\rm off})\,\tfrac{i_{\rm c} v_{\rm ce}}{I_{\rm nom,S} V_{\rm nom,S}}, \\ E_{\rm sw,D} &= E_{\rm rr}\,\tfrac{i_{\rm f} v_{\rm r}}{I_{\rm nom,D} V_{\rm nom,D}}, \end{aligned} \tag{3.7}$$

where $v_{\rm ce}$ is the IGBT off-state collector-emitter voltage and $v_{\rm r}$ is the diode reverse-blocking voltage. Values of $v_{\rm ceo}$, $R_{\rm on,S}$, $v_{\rm fo}$, $R_{\rm on,D}$, $E_{\rm on}$, $E_{\rm off}$, $E_{\rm rr}$, $I_{\rm nom,S}$, $V_{\rm nom,S}$, $I_{\rm nom,D}$, and $V_{\rm nom,D}$ can be obtained from data sheets of the corresponding devices.

Based on the averaged model of the MMC and the control system, the numbers of inserted SMs, arm currents, and capacitor voltages are expressed as

$$\begin{aligned} n^{p,j} &= \tfrac{1}{V_C^{\rm ref}}\left(\tfrac{1}{2}V_{\rm DC} - v_j^{\rm ref} - v_{\rm com}^{\rm out,ref}\right), \\ n^{n,j} &= \tfrac{1}{V_C^{\rm ref}}\left(\tfrac{1}{2}V_{\rm DC} + v_j^{\rm ref} + v_{\rm com}^{\rm out,ref}\right), \end{aligned} \tag{3.8}$$

$$\begin{aligned} i^{p,j} &= \tfrac{1}{2}i_j + i_{\rm cir,inj}^{j,\rm ref} + \tfrac{P^{\rm ref}}{3V_{\rm DC}}, \\ i^{n,j} &= -\tfrac{1}{2}i_j + i_{\rm cir,inj}^{j,\rm ref} + \tfrac{P^{\rm ref}}{3V_{\rm DC}}, \end{aligned} \tag{3.9}$$

$$v_C^{x,j} = V_C^{\rm ref} + \int_0^T \frac{n^{x,j}}{N} i^{x,j} dt, \tag{3.10}$$

where i_j is the line current of phase j, $v_j^{\rm ref}$ is the terminal voltage reference, $v_{\rm com}^{\rm out,ref}$ is the reference of the output common-mode voltage, and T is the period of line frequency, i.e., 50/60 Hz. In (3.8) and (3.9), i_j and $v_j^{\rm ref}$ can be obtained from real and reactive power references. The currents through the IGBTs and diodes, i.e., $i_{\rm c}$ and $i_{\rm f}$ in (3.6) are provided in Table 3.1.

Table 3.1: Current through IGBTs and diodes

Gating signal	Arm current	$i_{\rm c}$		$i_{\rm f}$	
		S_1	S_2	D_1	D_2
SM inserted	$i^{x,j} > 0$	0	0	$i^{x,j}$	0
	$i^{x,j} < 0$	0	$-i^{x,j}$	0	0
SM bypassed	$i^{x,j} > 0$	$i^{x,j}$	0	0	0
	$i^{x,j} < 0$	0	0	0	$-i^{x,j}$

For the switching loss, at each switching moment, $i_{\rm c}$ and $i_{\rm f}$ equal to $|i^{x,j}|$ and $v_{\rm ce}$ and $v_{\rm f}$ equal to the $v_C^{x,j}$. Based on a regular-sampling PWM strategy, the conduction time interval and switching moments can be determined and, subsequently, the conduction and switching

losses within each switching period can be calculated.

3.3 The Proposed Genetic Algorithm-based Optimization

The proposed optimization method has two objectives, i.e., minimizing the total power losses of the MMC to improve its efficiency and minimizing the power loss of the semiconductor devices with the highest temperature to improve the lifetime of the converter.

To optimize the power loss distribution, negative-sequence second-order circulating current, third-order output common-mode voltage, and SM capacitor voltages are adjusted. Therefore, the degrees of freedom can be summarized as five variables: magnitude and phase angle of the second-order circulating current, i.e., $\hat{I}_2$ and ϕ_{I2}, magnitude and phase angle of the third-order output common-mode voltage, i.e., $\hat{V}_{\mathrm{com}}^{\mathrm{out}}$ and $\phi_{V\mathrm{ocm}}$, and SM capacitor voltage reference, i.e., V_C^{ref}. Based on Section 3.2, the relations between the semiconductor power loss and the five variables can be summarized as:

$$\mathbf{P_{loss}} = \mathbf{F}\left(\hat{I}_2, \phi_{I2}, \hat{V}_{\mathrm{com}}^{\mathrm{out}}, \phi_{V\mathrm{ocm}}, V_C^{\mathrm{ref}}\right), \tag{3.11}$$

where $\mathbf{P_{loss}} = [P_{\mathrm{loss,S1}}\ P_{\mathrm{loss,D1}}\ P_{\mathrm{loss,S2}}\ P_{\mathrm{loss,D2}}]^T$ denotes the average power loss of each semiconductor device. The function $\mathbf{F}$ includes the averaged model of the MMC, control system, and the power loss calculation method. Combining the two objectives and the power loss calculation function along with the constraints, the optimization problem becomes

$$\begin{aligned}
&\underset{\mathbf{x}}{\text{minimize}} \quad (P_{\mathrm{total}}(\mathbf{x}), P_{\max}(\mathbf{x})) \\
&\text{subject to} \quad \mathbf{P_{loss}} = \mathbf{F}(\mathbf{x}) \\
&\qquad P_{\mathrm{total}} = P_{\mathrm{loss,S1}} + P_{\mathrm{loss,D1}} + P_{\mathrm{loss,S2}} + P_{\mathrm{loss,D2}} \\
&\qquad P_{\max} = \max\{P_{\mathrm{loss,D1}}, P_{\mathrm{loss,D2}}, P_{\mathrm{loss,S1}}, P_{\mathrm{loss,S2}}\} \\
&\qquad \mathbf{x_{min}} \leqslant \mathbf{x} \leqslant \mathbf{x_{max}} \\
&\qquad \xi_{\mathbf{min}} \leqslant \xi(t) \leqslant \xi_{\mathbf{max}}
\end{aligned} \tag{3.12}$$

where $\mathbf{x} = \left[\hat{I}_2, \phi_{I2}, \hat{V}_{\rm com}^{\rm out}, \phi_{V\rm ocm}, V_C^{\rm ref}\right]$ and $\xi(t)$ refer to a vector of time-variant variables such as $n^{x,j}$ and $i^{x,j}$.

The multi-objective optimization in (3.12) leads to a set of Pareto optimal solutions. An offline optimization can be run for various setpoints of real and reactive power to generate the Pareto optimal front of each operating condition. Based on the offline results, a look-up table or some empirical equations can be obtained to facilitate implementation of the proposed method.

3.4 Simulation Studies

In this section, the Pareto optimal front is derived and verified based on the PLECS software environment. Fig. 3.1 presents the study system with its parameters listed in Table 3.2. On the AC-side, decoupled qd-current-based control is utilized, where the setpoints of real and reactive powers are 22.5 MW and 15 MVAr, respectively. The MATLAB toolbox of GOSET 2.6 is utilized to solve the optimization problem [101]. The IGBT and diode models of the study system are ABB 5SNA 0650J450300 and 5SLD 0650J450300, respectively.

Table 3.2: Parameters of the study system

Quantity	Value
MMC nominal power $S_{\rm b}$	30 MVA
AC system nominal voltage $V_{\rm ll,rms}$	15 kV
Nominal frequency	60 Hz
R	0.015 Ω
L	2.4 mH
Buffer inductance l	7.4 mH
Series arm resistance r	0.116 Ω
DC source voltage $V_{\rm DC}$	30 kV
Number of SMs per arm N	12
Switching frequency $f_{\rm sw}$	1.2 kHz
Submodule capacitor C	3000 μF

Fig. 3.3 shows the Pareto front of the average power loss of S_2 versus the total power losses of the MMC. The result for a conventional operating point, where only the second-

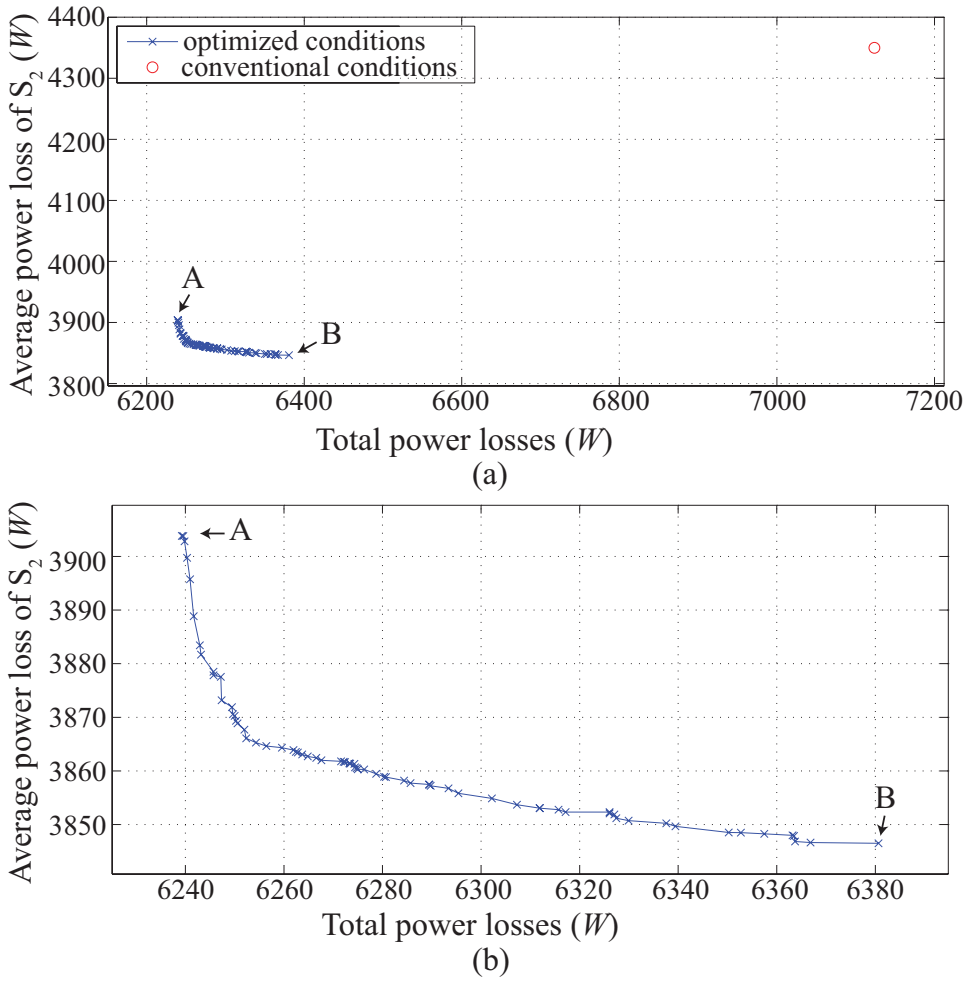

Figure 3.3: (a) Pareto front of the average power loss of S_2 versus the total power loss, (b) zoomed portion of Pareto front.

Table 3.3: Operating conditions of the simulation study system

Cond.	$\hat{I}_2$	ϕ_{I2}	$\hat{V}_{\text{com}}^{\text{out}}$	$\phi_{V\text{ocm}}$	V_C^{ref}
Conv.	0	0	0	0	2.5 kV
Opt. A	0.18 kA	-108.9°	1.69 kV	-0.2°	2.19 kV
Opt. B	0.07 kA	-60.4°	1.58 kV	-21.8°	2.15 kV

order circulating current is suppressed [102], is also projected in Fig. 3.3. The comparison confirms a significant improvement in both the total semiconductor power loss and the power loss of S_2, whose junction temperature is the highest among S_1, S_2, D_1, and D_2. As illustrated in Fig. 3.3, the operating conditions A and B, which are at the two ends of the Pareto front, are selected for the simulation study. The converter variables under the two

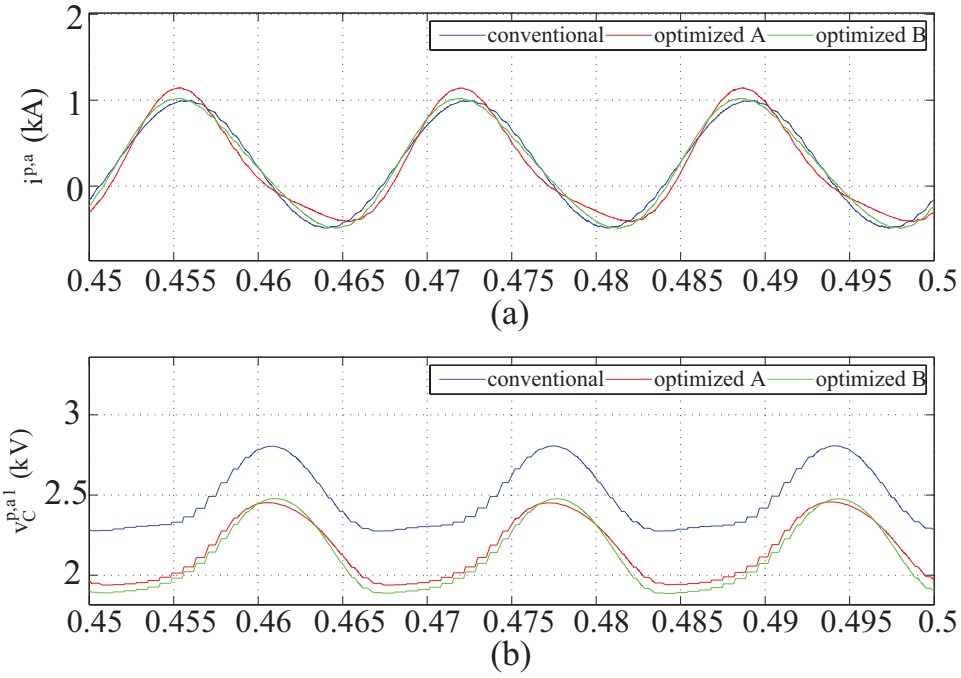

Figure 3.4: MMC waveforms under the conventional and optimized operating conditions A and B: (a) arm current of the upper arm of phase a, (b) SM capacitor voltage of the first SM of the upper arm of phase a.

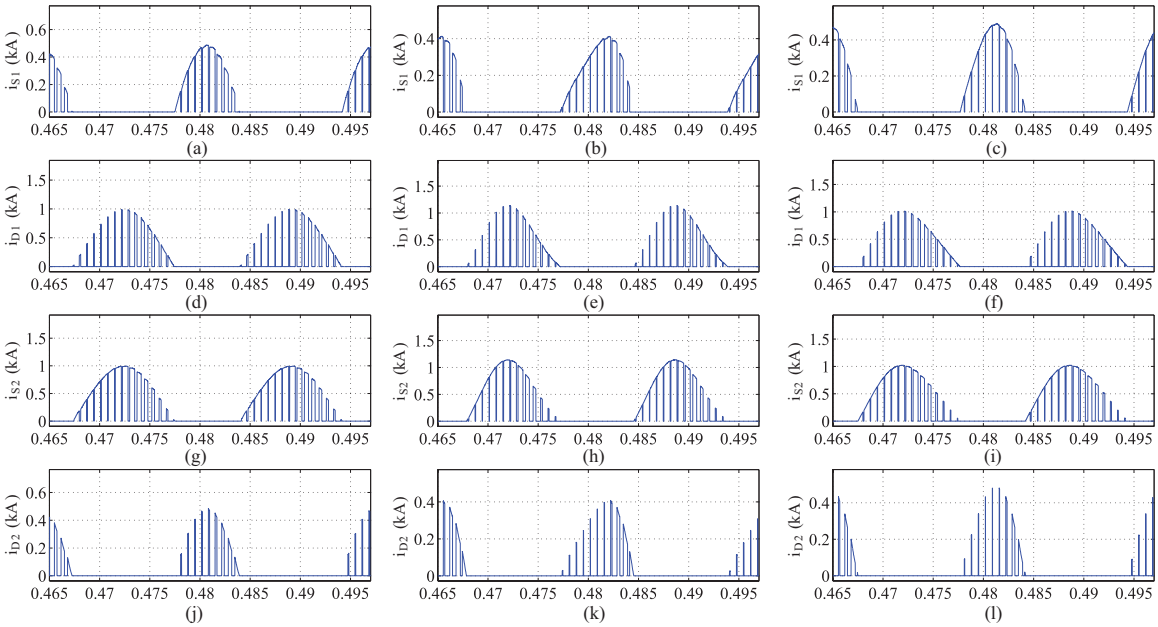

Figure 3.5: Current flowing through S_1, D_1, S_2, and D_2: (a), (d), (g), and (j) under the conventional operating condition, (b), (e), (h), and (k) under the optimized operating condition A, and (c), (f), (i), and (l) under the optimized operating condition B.

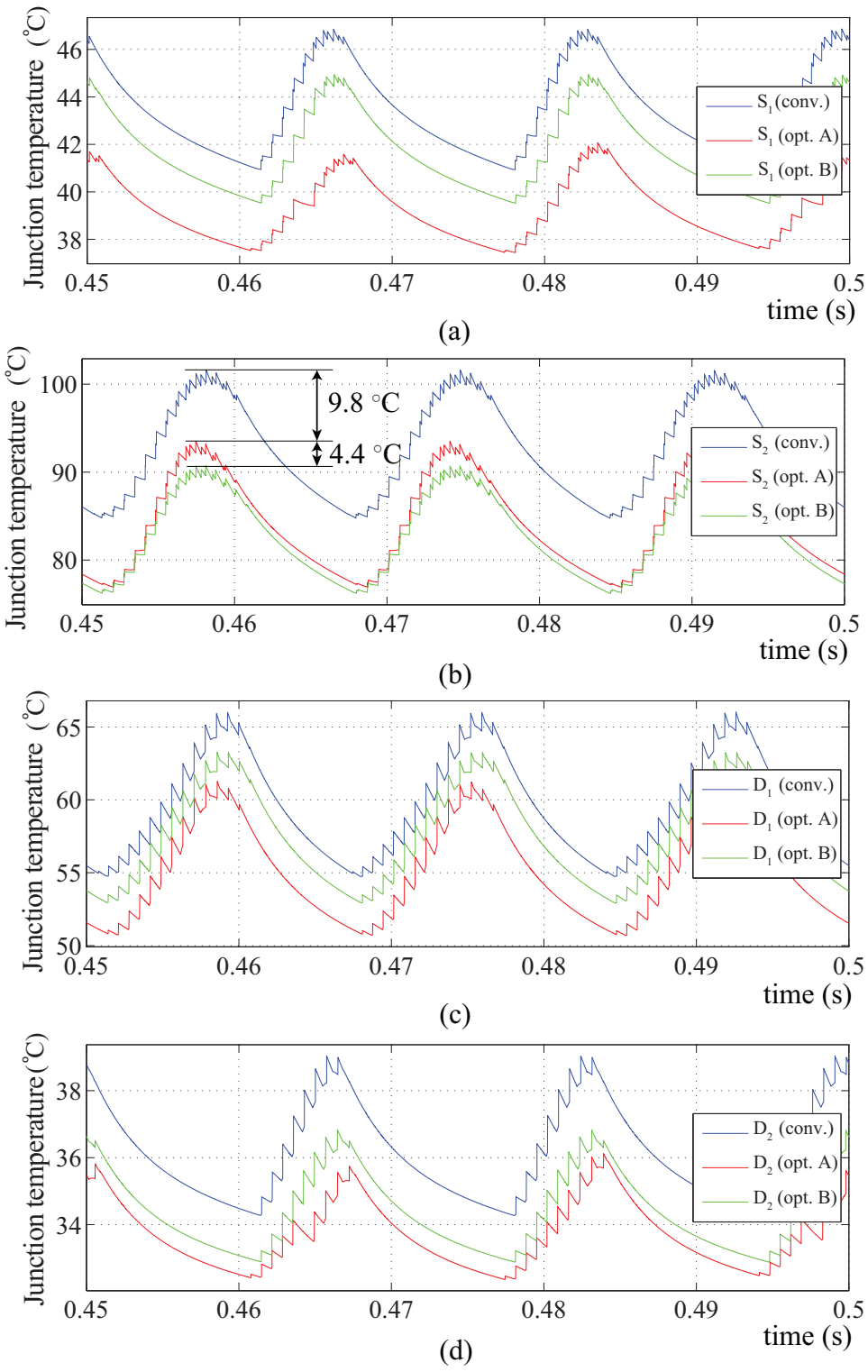

Figure 3.6: Junction temperature of: (a) S_1, (b) S_2, (c) D_1, and (d) D_2.

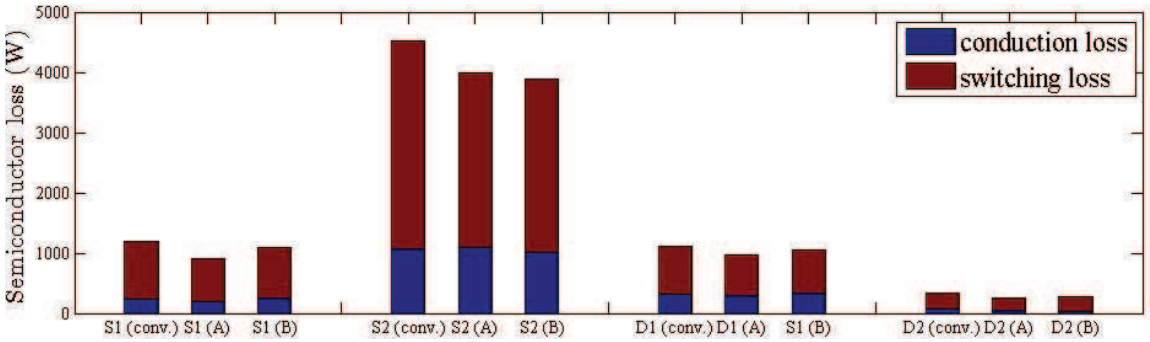

Figure 3.7: Power losses of semiconductor devices in each SM.

operating conditions (A and B) are compared with the conventional operating condition in Table 3.3. Therefore, the operating conditions A and B correspond to two optimized objectives, i.e.,

• Condition A: minimizing the total power losses of the MMC;

• Condition B: minimizing the power loss of the semiconductor devices with the highest thermal loading.

Fig. 3.4 compares the arm currents and capacitor voltages under the three operating conditions. Fig. 3.5 shows the currents flowing through the four semiconductor devices in one SM (first SM of the upper arm of phase a). Fig. 3.6 presents the junction temperatures of S_1, S_2, D_1, and D_2 under the three conditions, which verifies effectiveness of the proposed optimization method. As illustrated in Fig. 3.6, the highest junction temperature is reduced by 9.8 $^{\circ}C$ under the operating condition A. Under the operating condition B, junction temperature of S_2 is further reduced by 4.4 $^{\circ}C$ compared with the operating condition A. However, the junction temperatures of S_1, D_1, and D_2 under the operating condition B are higher than those under the operating condition A. The averaged power loss of the semiconductors is presented in Fig. 3.7. As illustrated in Fig. 3.7, semiconductor power losses under the two optimized conditions are significantly lower than the ones under the conventional operating condition. Furthermore, Fig. 3.7 shows that power loss of S_2 under the optimized condition B is lower than that under the operating condition A, while the power losses of S_1, D_1, and D_2 under the condition B are higher than those under the

condition A.

CHAPTER 4

AN OPEN-CIRCUIT FAULT DETECTION METHOD OF THE DC-AC MMC

In this chapter, an open-switch SM-failure detection and locating method based on a clustering algorithm (CA) is proposed. In the proposed method, a clustering algorithm is applied to analyze and identify the operating pattern of the fault-sensitive variables of the faulty and normal SMs. Without any additional sensor, the proposed method can accurately detect and locate the faulty SMs within a reasonable time. Performance and effectiveness of the proposed failure detection and locating methods are compared and evaluated based on time-domain simulation studies in the PSCAD/EMTDC software environment.

4.1 Impact of Open-Switch SM Failures on the Operation of an MMC

As shown in Fig. 4.1, open-switch failures of an SM can be:

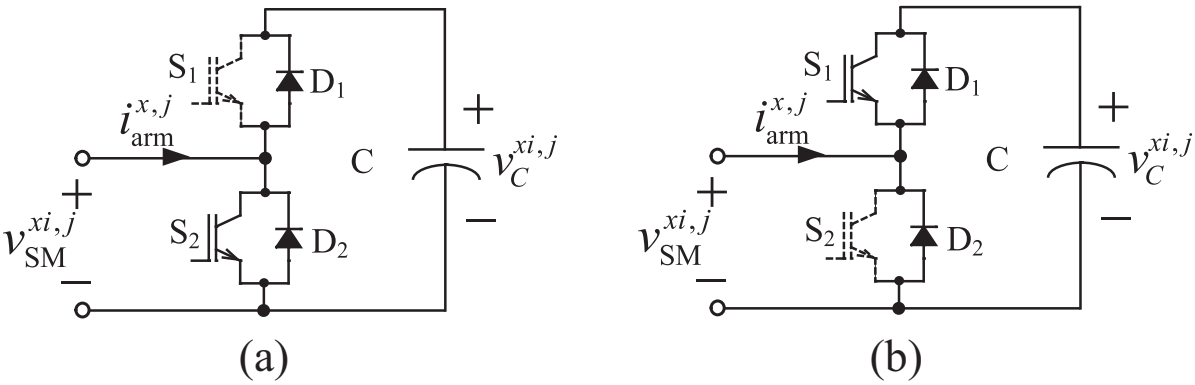

Figure 4.1: SM open-switch failure: (a) open-circuit failure at S_1 and (b) open-circuit failure at S_2.

- Open-circuit failure of switch S_1 as shown in Fig. 4.1(a) (hereafter referred as "ft1"): Since S_1 is located on the inserting path of the SM capacitor, under open-switch failure of S_1, $v_{C,\text{ft1}}^{xi,j}$ will never decrease. If the arm current is negative and S_1 is commanded to be ON, the arm current is forced to flow through the diode D_2 instead

of S_1, and the faulty SM is bypassed. When the arm current is positive and S_1 is commanded to be ON, the arm current flows through the diode D_1, charging the SM capacitor. If the SM is bypassed, the arm current will flow through its normal operating condition path, i.e., through S_2 if $i_{\mathrm{arm}}^{x,j} > 0$ and through D_2 if $i_{\mathrm{arm}}^{x,j} < 0$.

- Open-circuit failure of switch S_2 as shown in Fig. 4.1(b) (hereafter referred as "ft2"): If the arm current is positive and S_2 is commanded to be ON, the arm current is forced to flow through the diode D_1 instead of S_2, and the faulty SM is inserted, charging the SM capacitor. Otherwise, the arm current will flow through its normal operating condition path.

The impact of the current direction and the switching state on the capacitor voltages of healthy and faulty SMs is summarized in Table 4.1.

4.2 The Proposed Clustering Algorithm (CA)-based Method

In the proposed CA-based failure detection and locating method, a clustering algorithm is used to distinguish the dynamic characteristics of the faulty SMs from those of the healthy ones. As shown in Tables 4.1, the capacitor current of the normal SMs, i.e., $i_{C,\mathrm{hy}}^{x,j}$ and the commend-based estimated capacitor current of the faulty SMs, i.e., $i_{C,\mathrm{ft,cd}}^{x,j}$ are expressed by

$$\begin{aligned} i_{C,\mathrm{hy}}^{x,j} &= \frac{n_{\mathrm{hy}}^{x,j}}{N_{\mathrm{hy}}^{x,j}} i_{\mathrm{arm}}^{x,j}, \\ i_{C,\mathrm{ft,cd}}^{x,j} &= \frac{n_{\mathrm{ft,cd}}^{x,j}}{N_{\mathrm{ft}}^{x,j}} i_{\mathrm{arm}}^{x,j}, \end{aligned} \tag{4.1}$$

where the superscript x, j refers to the x arm of phase j, $n_{\mathrm{hy}}^{x,j}$ is the number of inserted normal SMs, $n_{\mathrm{ft,cd}}^{x,j}$ is the commanded number of the inserted faulty SMs, $N_{\mathrm{hy}}^{x,j}$ is the total number of the normal SMs, and $N_{\mathrm{ft}}^{x,j}$ is the total number of the faulty SMs. Since the actual capacitor currents are discontinuous, the commanded dynamic-average capacitor currents,

i.e., $\hat{i}_C^{xi,j}$ can be calculated by

$$\hat{i}_C^{xi,j} = \frac{1}{T_{\text{av}}^{\text{CA}}} \int_{t-T_{\text{av}}^{\text{CA}}}^{t} S_1^{xi,j}(\tau) i_{\text{arm}}^{x,j}(\tau)\, d\tau, \tag{4.2}$$

where T^{CA} is the time interval to calculate $\hat{i}_C^{xi,j}$.

Table 4.1: Relations among the arm current direction, SM state, and SM output

Normal SM				
$i_{\text{arm}}^{x,j}$	>0		<0	
$S_1^{xi,j}$	1	0	1	0
Current Path	D_1	S_2	S_1	D_2
Impact	charging	no impact	discharging	no impact
$v_{\text{SM}}^{xi,j}$	$v_{C,\text{hy}}^{xi,j}$	0	$v_{C,\text{hy}}^{xi,j}$	0
Faulty SM with open-circuit failure of switch S_1				
$i_{\text{arm}}^{x,j}$	>0		<0	
$S_1^{xi,j}$	1	0	1	0
Current Path	D_1	S_2	D_2	D_2
Impact	charging	no impact	no impact	no impact
$v_{\text{SM}}^{xi,j}$	$v_{C,\text{ft1}}^{xi,j}$	0	0	0
Faulty SM with open-circuit failure of switch S_2				
$i_{\text{arm}}^{x,j}$	>0		<0	
$S_1^{xi,j}$	1	0	1	0
Current Path	D_1	D_1	S_1	D_2
Impact	charging	charging	discharging	no impact
$v_{\text{SM}}^{xi,j}$	$v_{C,\text{ft2}}^{xi,j}$	$v_{C,\text{ft2}}^{xi,j}$	$v_{C,\text{ft2}}^{xi,j}$	0

To smooth the waveforms of $\hat{i}_C^{xi,j}$ and improve performance of the proposed method, $\hat{i}_C^{xi,j}$ is passed through a low-pass filter, outputting $\hat{i}_{C,\text{f}}^{xi,j}$. $v_C^{xi,j}$ and $\hat{i}_{C,\text{f}}^{xi,j}$ of each SM are used to form a vector to describe the dynamic characteristics of the corresponding SM, illustrated by a two-dimensional trajectory. The formed vector, i.e., $\mathbf{o}^{xi,j}$ is expressed by

$$\mathbf{o}^{xi,j} = \left[\eta v_C^{xi,j}(1), \cdots, \eta v_C^{xi,j}(M), \hat{i}_{C,\text{f}}^{xi,j}(1), \cdots, \hat{i}_{C,\text{f}}^{xi,j}(M)\right], \tag{4.3}$$

where M is the number of sampling points within T^{CA}, η is a coefficient to scale the

magnitude of the measured $v_C^{xi,j}$.

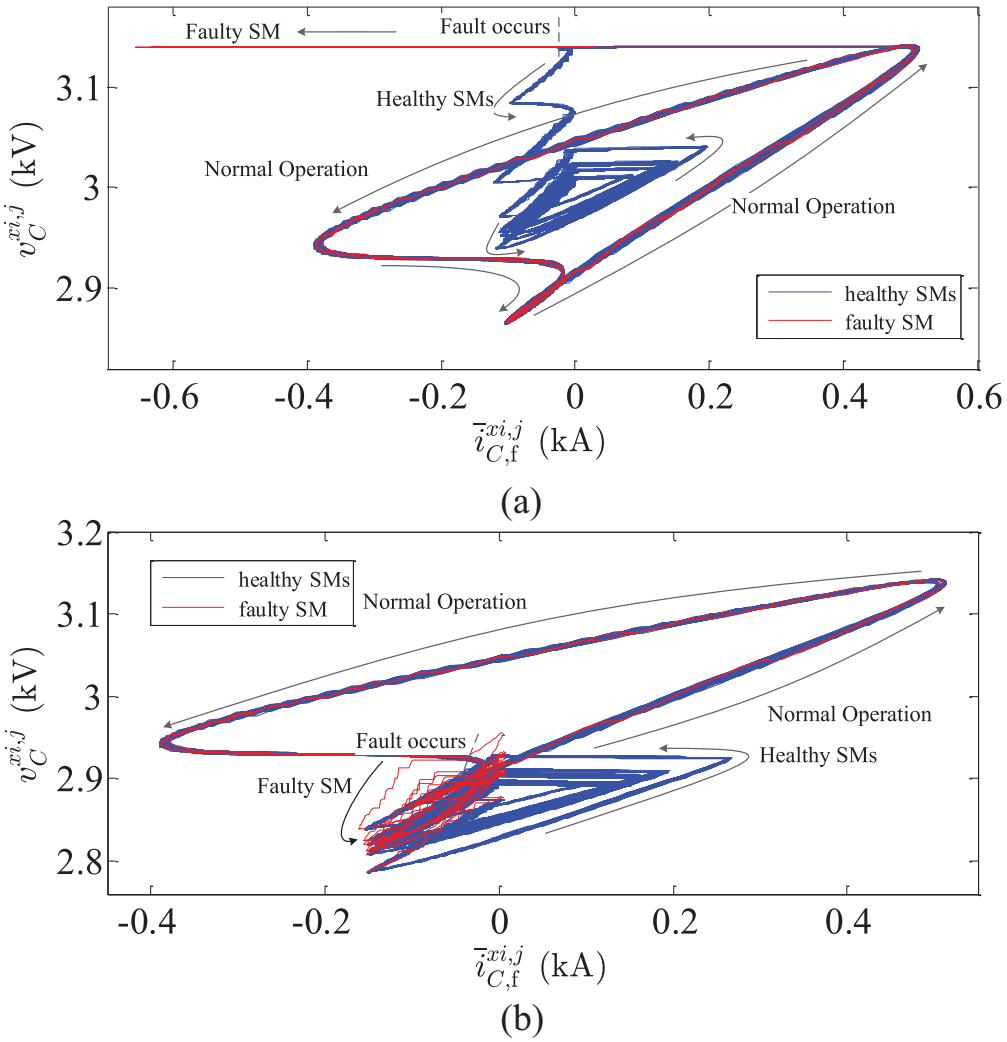

Figure 4.2: Trajectories of $v_C^{pi,a}$ v.s. $\hat{i}_{C,\mathrm{f}}^{pi,a}$: (a) Case I, (b) Case II.

Figures 4.2(a) and (b) show the two-dimensional trajectories of $v_C^{xi,j}$ v.s. $\hat{i}_{C,\mathrm{f}}^{xi,j}$ for two SM-failure cases, which will be discussed in Section 4.3. Prior to any SM failure occurrence, trajectories of SMs of each arm, which are individually defined by (4.3), coincide as shown in Figs. 4.2(a) and (b). Subsequent to any SM failure, as shown in Figs. 4.2(a) and (b), the trajectories of the faulty and normal SMs deviate from each other. In this section, K-means algorithm is used to classify the N vectors associated with the N SMs in one

arm, into $K^{x,j}$ clusters. Each cluster has a centroid, i.e., $\mathbf{c}_{\zeta}^{x,j}$ defined as:

$$\mathbf{c}_{\zeta}^{x,j} = \left[\eta v_{C,\zeta,\text{avg}}^{x,j}(1), \cdots, \eta v_{C,\zeta,\text{avg}}^{x,j}(M), \hat{i}_{C,\text{f},\zeta,\text{avg}}^{x,j}(1), \cdots, \hat{i}_{C,\text{f},\zeta,\text{avg}}^{x,j}(M)\right], \tag{4.4}$$

which can be calculated by

$$\mathbf{c}_{\zeta}^{x,j} = \frac{1}{N_{\zeta}^{x,j}} \sum_{i \in C_{\zeta}^{x,j}} \mathbf{o}^{xi,j}. \tag{4.5}$$

The distance between one vector in the ζth cluster and the centroid of the ζth cluster, i.e., $d\left(\mathbf{o}^{xi,j}, \mathbf{c}_{\zeta}^{x,j}\right)$ can be defined as

$$\begin{aligned} & d\left(\mathbf{o}^{xi,j}, \mathbf{c}_{\zeta}^{x,j}\right) = \left\|\mathbf{o}^{xi,j} - \mathbf{c}_{\zeta}^{x,j}\right\|^2 \\ & = \eta^2 \sum_{\xi=1}^{M} (v_C^{xi,j}(\xi) - v_{C,\zeta,\text{avg}}^{xi,j}(\xi))^2 + \sum_{\xi=1}^{M} (\hat{i}_{C,\text{f}}^{xi,j}(\xi) - \hat{i}_{C,\text{f},\zeta,\text{avg}}^{x,j}(\xi))^2. \end{aligned} \tag{4.6}$$

Furthermore, in the ζth cluster, the average value of the distances from the vectors to the centroid, i.e., $D_{\zeta(K)}^{x,j}$, is expressed as

$$D_{\zeta(K)}^{x,j} = \frac{1}{N_{\zeta}^{x,j}} \sum_{i \in C_{\zeta}^{x,j}} d\left(\mathbf{o}^{xi,j}, \mathbf{c}_{\zeta}^{x,j}\right), \tag{4.7}$$

where $C_{\zeta}^{x,j}$ is the set of all the $\mathbf{o}^{xi,j}$ in the ζ-th cluster.

By using the K-means algorithm, $\mathbf{c}_{\zeta}^{x,j}$ of all the clusters can be determined, so that $D_{\zeta(K)}^{x,j}$ is minimal [103]. The details of the algorithm is provided in the Appendix.

The implementation flowchart of the CA-based method is summarized in Fig. 4.3. Initially, N vectors associated with N SMs of one arm are assumed to belong to one cluster, corresponding to normal operation. If a fault occurs, $v_C^{xi,j}$ and $\hat{i}_{C,\text{f}}^{xi,j}$ of the faulty SM(s) will deviate from the healthy ones, and $D_{1(1)}^{x,j}$ will increase by several orders of magnitude within 2$\sim$4 fundamental periods. Hence, if $D_{1(1)}^{x,j}$ reaches a certain threshold, a failure is detected in the arm. Meanwhile, clustering algorithm is executed to classify the N vectors into two clusters: one for the normal SMs and the other for the faulty SMs. If only one type

of open-switch failure, either S_1 or S_2, exists in the arm, the new values of $D^{x,j}_{1(2)}$ and $D^{x,j}_{2(2)}$ will be both under the threshold. Through clustering, based on affiliation of the vectors with the clusters, the faulty SMs can be pinpointed.

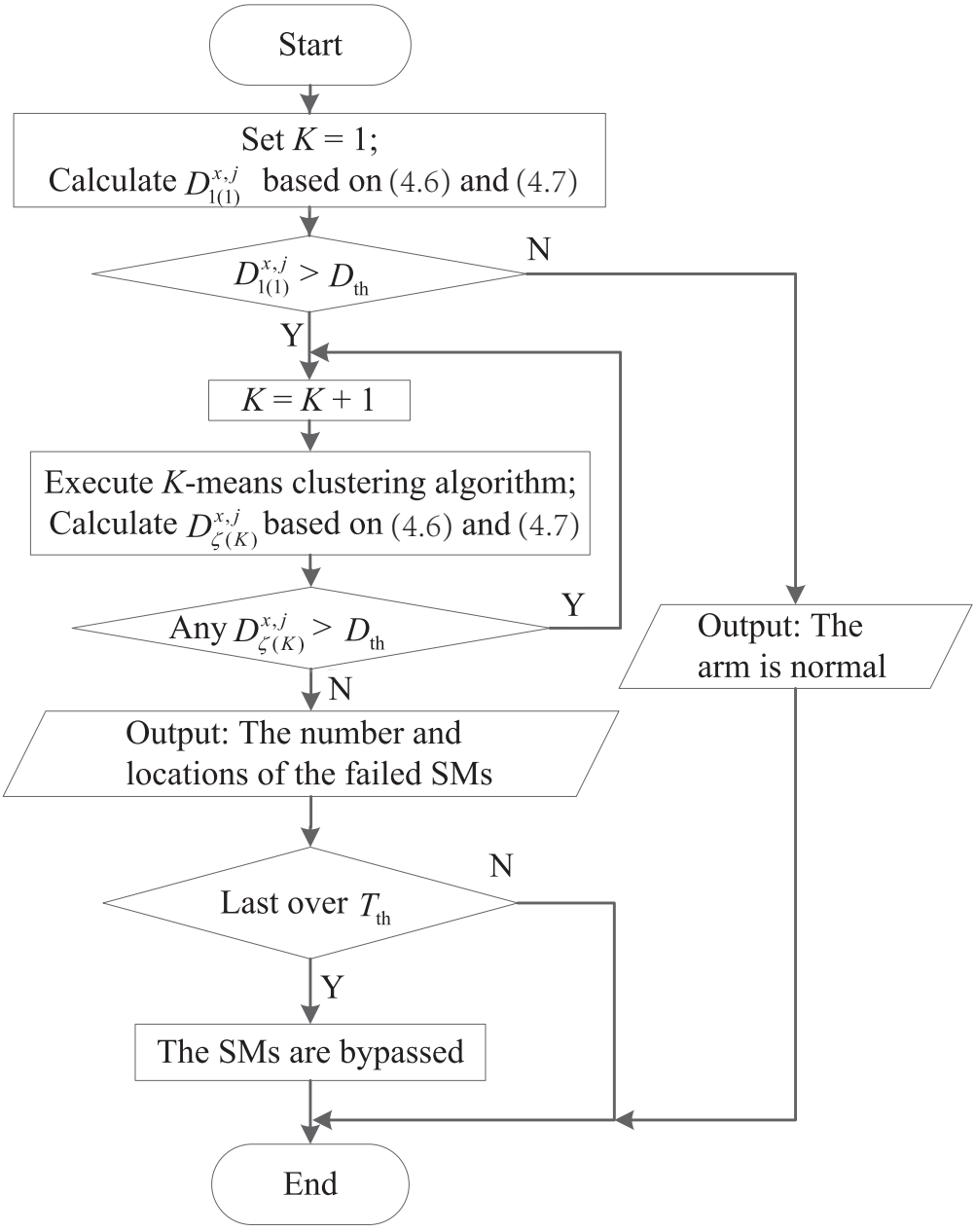

Figure 4.3: Flowchart of the CA-based method.

Table 4.2: Parameters of the study system of the MMC

Quantity	Value
MMC nominal power S_{b}	50 MVA
AC system nominal voltage $V_{\mathrm{ll,rms}}$	30 kV
Nominal frequencies	60 Hz
R	0.03 Ω
L	5 mH
Buffer inductance l	3 mH
Series arm resistance r	0.09 Ω
DC Source Voltage V_{dc}	60 kV
Number of SMs per arm N	20
Sorting period T_{sorting}	100 μs
Submodule capacitor C	14000 μF

4.3 Study Results

In this section, the study results are presented to evaluate the performance and effectiveness of the proposed failure detection methods. The studies are conducted in the PSCAD/EMTDC software environment. The parameters of the study system that is a grid-connected MMC with 20 SMs per arm, are listed in Table 4.2. The grid-connected MMC exchanges real and reactive power with the utility grid based on the closed-loop qd-current control technique. The setpoints for real and reactive power are chosen at -25 MW and 18 MVAr, respectively. Two case studies are conducted:

- Case I: open-circuit switch failure occurs in switch S_1 of the 20th SM in the upper arm of phase a at $t = 0.2$ s.
- Case II: open-circuit switch failure occurs in switch S_2 of the 20th SM in the upper arm of phase a at $t = 0.2$ s.

Figure 4.4 illustrates $v_C^{pi,a}$ and $\hat{i}_{C,\mathrm{f}}^{pi,a}$ of the SMs in the upper arm of phase a, prior and subsequent to the occurrence of the open-switch fault for Cases I and II. Subsequent to the fault, the trajectories of $v_C^{pi,a}$ v.s. $\hat{i}_{C,\mathrm{f}}^{pi,a}$ of the faulty SMs deviate from those of healthy ones, as shown in Fig. 4.2. Figures 4.5(a) and (c) show that, subsequent to an open-circuit fault

in either S_1 or S_2, the order of magnitude of $D^{p,a}_{1(1)}$ suddenly increases from -4 to -1. Setting the sampling frequency as 10 kHz, the threshold value as 5×10^{-3}, the time required to detect the open-switch failures are 38.8 ms and 97.1 ms for Cases I and II, respectively. Subsequent to fault detection, based on the CA, the vectors are classified into two clusters, i.e., $D^{p,a}_{1(2)}$ for the normal SMs and $D^{p,a}_{2(2)}$ for the faulty SM. As shown in Figs. 4.5(b) and (d), $D^{p,a}_{1(2)}$ and $D^{p,a}_{2(2)}$ are all below the threshold value. Meanwhile, the 20th SM, associated with $D^{p,a}_{2(2)}$, is pinpointed as the faulty one. Method

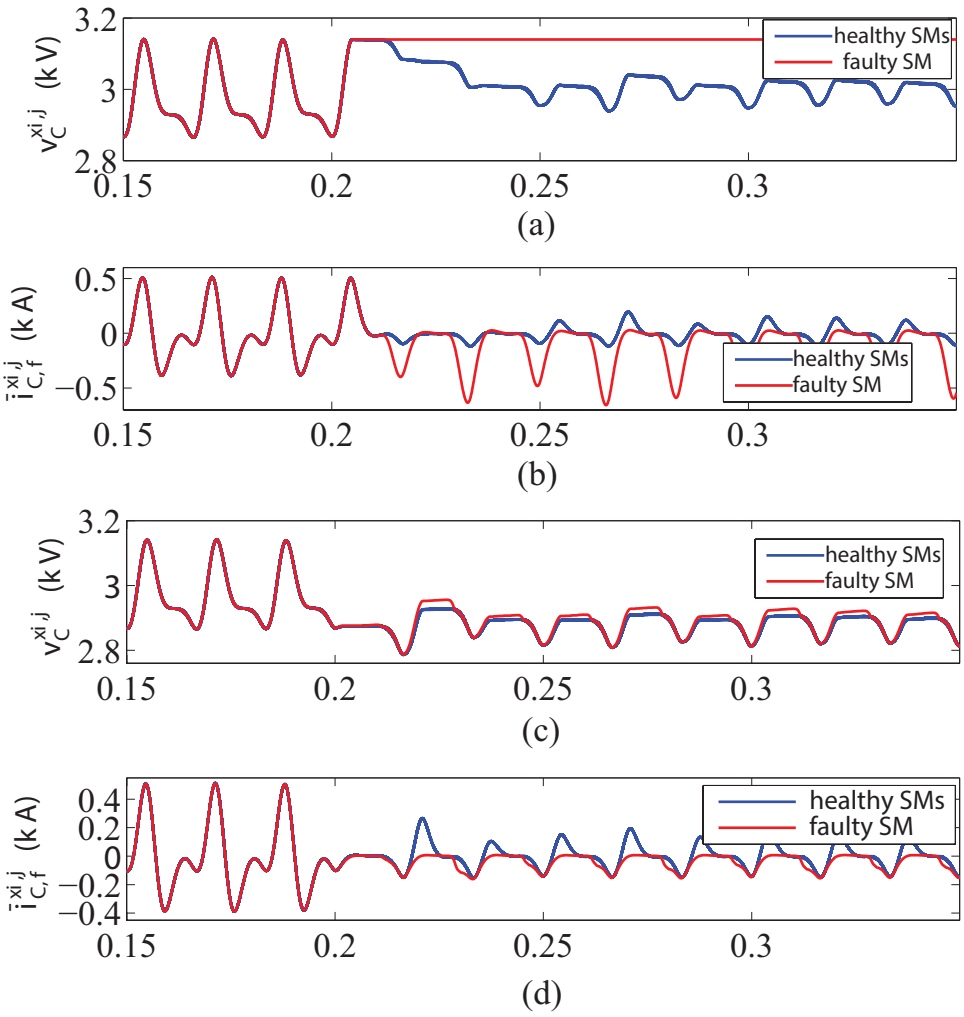

Figure 4.4: Waveforms of: (a) $v_C^{pi,a}$ in Case I, (b) $\hat{i}_{C,\mathrm{f}}^{pi,a}$ in Case I, (c) $v_C^{pi,a}$ in Case II, (d) $\hat{i}_{C,\mathrm{f}}^{pi,a}$ in Case II.

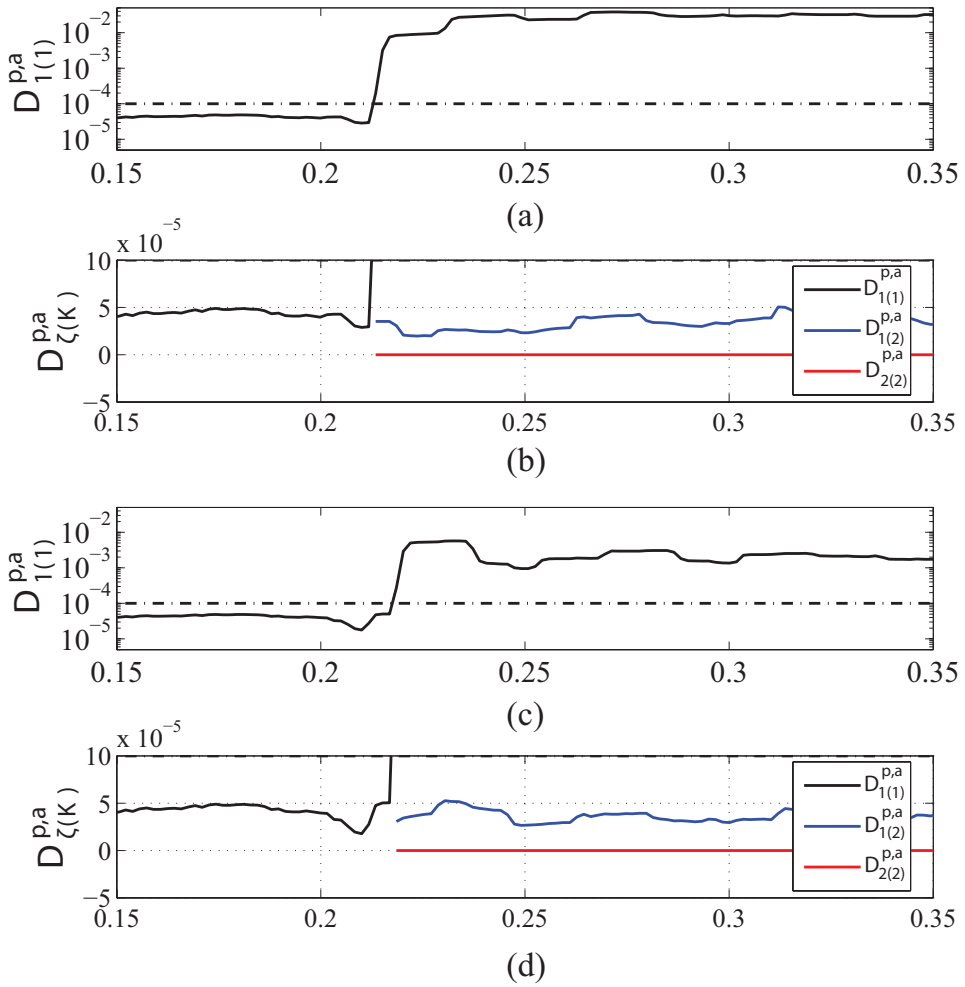

Figure 4.5: $D^{p,a}_{\zeta(K)}$: (a) $D^{p,a}_{1(1)}$ in Case I, (b) $D^{p,a}_{\zeta(K)}$ in Case I, (c) $D^{p,a}_{1(1)}$ in Case II, (d) $D^{p,a}_{\zeta(K)}$ in Case II.

4.4 Features of the Proposed Method

The proposed method is based upon comparison of the characteristics of a group of SMs. By comparison of the proposed CA-based method with the reported SM-failure detection methods, the followings are concluded:

- The required information for the implementation is $v_C^{xi,j}$, $S_1^{xi,j}$, and $i_{\text{arm}}^{x,j}$. Since all of those information can be provided based on the already measured signals for control purposes, there is no requirement for any additional measurement.

- The proposed method is effective for not only the open-switch failures, but also any type of fault that causes the deviation of the characteristic trajectories of the faulty SMs from those of the normal SMs. The sampling period for $i_{\text{arm}}^{x,j}$ and $v_C^{xi,j}$ is independent of the sorting algorithm period. As long as M is sufficiently large to distinguish $\mathbf{o}^{xi,j}$ of the faulty SMs from the healthy ones, the sampling period does not have any restriction.

CHAPTER 5

FAULT-TOLERANT CONTROL OF THE DC-AC AND AC-AC MMCS

This section presents:

- a fault-tolerant strategy based on adaption of the neutral-shift strategy to maximize the available output line-to-line voltages and the power transfer capability of the MMC subsequent to bypassing the faulty SMs. Since the conventional circulating current suppression methods are not meant to operate under unbalanced conditions, a new circulating current suppression method is also proposed. Performance of the proposed neutral-shift strategy and supporting circulating current suppression method are evaluated based on time-domain simulation studies in the PSCAD/EMTDC software environment.

- a fault-tolerant strategy to control the AC-AC MMC under input-side line-to-ground fault conditions is proposed. Since the unbalanced fault conditions cause significant negative-sequence input-side voltage components, input-side current regulation, capacitor voltage balancing, and capacitor voltage fluctuation mitigation methods are modified. The effectiveness of the proposed fault-tolerant strategy is verified by the simulation results in the PSCAD/EMTDC software environment.

- a fault-tolerant strategy to ensure stable operation and normal power transfer capability of the AC-AC MMC through modification of the SM capacitor voltages of the faulty cluster. This section also proposes strategies to attenuate the large SM capacitor voltage fluctuations when the output-side frequency is close to the input-side frequency. The effectiveness of the proposed methods are verified by the simulation results in the PSCAD/EMTDC software environment.

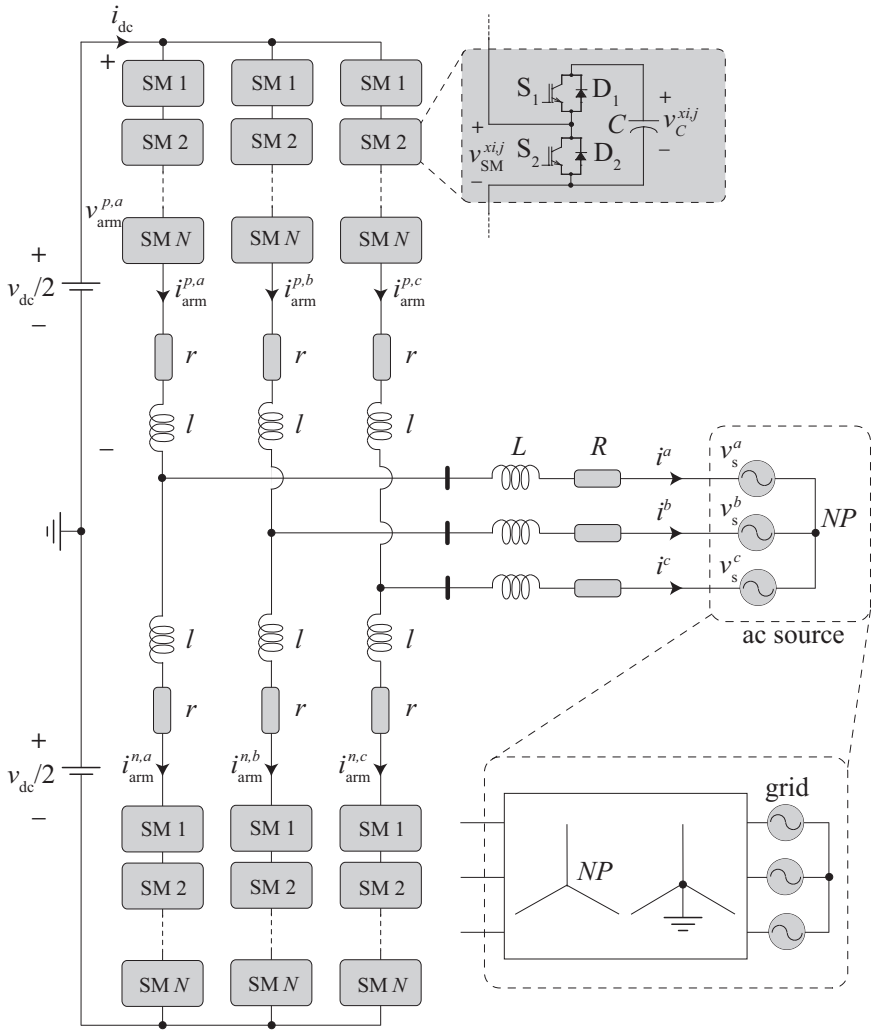

Figure 5.1: Circuit diagram of a grid-connected MMC.

5.1 Fault-Tolerant Control of the DC-AC MMC under an Internal Fault

5.1.1 A neutral-shift-based fault-tolerant strategy

In this section, a fault-tolerant strategy based on the neutral-shift method is presented, which, subsequent to bypassing the faulty SM(s), aims at improving the maximum attainable line-to-line voltages of the MMC. Figure 5.1 shows a schematic diagram of a three-phase MMC, which is connected to the grid through a three-phase transformer.

Under normal operation, voltage references for the three phase-legs are balanced. The modulation indices and angles m and φ_{m} are generated by the closed-loop control system

[8]. However, subsequent to bypassing faulty SM(s) in the faulty phase j, $\hat{V}^{j}_{\mathrm{t}O,\mathrm{mx}}$ of the faulty phase is reduced. In this case, $\hat{V}^{j}_{\mathrm{t}O,\mathrm{mx}}$ is expressed by:

$$\begin{aligned} \hat{V}^{j}_{\mathrm{t}O,\mathrm{mx}} &= \left(\tfrac{1}{2} - \tfrac{N^{j}_{\mathrm{ft}}}{N}\right) V_{\mathrm{dc}}, \\ N^{j}_{\mathrm{ft}} &= \max\left\{N^{p,j}_{\mathrm{ft}}, N^{n,j}_{\mathrm{ft}}\right\}. \end{aligned} \tag{5.1}$$

where $N^{p,j}_{\mathrm{ft}}$ and $N^{n,j}_{\mathrm{ft}}$ are the number of faulty SMs in upper and lower arms of phase j, N is the total number of SMs in one arm, V_{dc} is the DC-link voltage, and $\hat{V}^{j}_{\mathrm{t}O,\mathrm{mx}}$ is the maximum peak voltage between the AC-terminal of phase j and the mid-point O of the DC-link. If the references of the phase voltages remain as a balanced set, the attainable voltages will be determined by the minimum value of $\hat{V}^{j}_{\mathrm{t}O,\mathrm{mx}}$ ($j = a, b, c$). This, consequently, will significantly reduce the maximum three-phase terminal voltages as well as the maximum output voltage of the other phases.

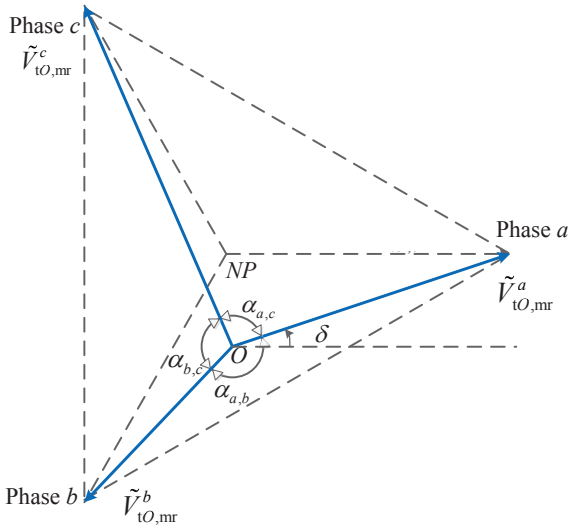

Figure 5.2: Phasor diagram of the proposed neutral-shift fault-tolerant strategy.

As shown in Fig. 5.2, by adjusting the magnitudes and phase angles of the converter phase voltages, the neutral point can be shifted and a balanced set of line-to-line voltages can be obtained, even though the MMC phase voltages are not balanced. In this case, to maximize the equilateral triangle constructed by the line-to-line voltages, i.e., the attainable

output voltage, the maximum attainable output voltage of each phase is fully utilized and the center of the equilateral triangle is shifted away from point O. Under normal operation, the magnitudes of the three-phase voltage references are identical and the points O and *NP* overlap at the center of the equilateral triangle. Based on Fig. 5.2, in the neutral-shift strategy, α_{j_1,j_2} can be obtained by

$$\alpha_{j_1,j_2} = \frac{\pi}{3} + \arccos \frac{\left(\hat{V}_{\mathrm{t}O,\mathrm{mx}}^{j_1}\right)^2 + \left(\hat{V}_{\mathrm{t}O,\mathrm{mx}}^{j_2}\right)^2 - \left(\hat{V}_{\mathrm{t}O,\mathrm{mx}}^{j_3}\right)^2}{2\hat{V}_{\mathrm{t}O,\mathrm{mx}}^{j_1}\hat{V}_{\mathrm{t}O,\mathrm{mx}}^{j_2}}. \tag{5.2}$$

The angle δ can be calculated by

$$\delta = \frac{\pi}{6} - \arcsin\left(\frac{\hat{V}_{\mathrm{t}O,\mathrm{mx}}^{b}}{\hat{V}_{\mathrm{t,ll,mx}}}\sin\left(\alpha_{a,b}\right)\right), \tag{5.3}$$

where

$$\hat{V}_{\mathrm{t,ll,mx}} = \sqrt{\left(\hat{V}_{\mathrm{t}O,\mathrm{mx}}^{j_1}\right)^2 + \left(\hat{V}_{\mathrm{t}O,\mathrm{mx}}^{j_2}\right)^2 - 2\hat{V}_{\mathrm{t}O,\mathrm{mx}}^{j_1}\hat{V}_{\mathrm{t}O,\mathrm{mx}}^{j_2}\cos\left(\alpha_{j_1,j_2}\right)}. \tag{5.4}$$

To implement the neutral-shift strategy, the original modulation indices and angles of the three phases, i.e., m^j and φ^j need to be modified by:

$$m^j = \frac{\sqrt{3}\hat{V}_{\mathrm{t}O,\mathrm{mx}}^{j}}{\hat{V}_{\mathrm{t,ll,mx}}}m, \tag{5.5}$$

and

$$\begin{aligned} \varphi^a &= \varphi_{\mathrm{m}} + \delta, \\ \varphi^b &= \varphi_{\mathrm{m}} + \delta - \alpha_{a,b}, \\ \varphi^c &= \varphi_{\mathrm{m}} + \delta + \alpha_{a,c}. \end{aligned} \tag{5.6}$$

By using the modified modulation indices and angles of the three phases, the modified voltage references of the three phases become:

$$v_{\mathrm{t}O,\mathrm{mr}}^{j} = \frac{1}{2}m^j V_{\mathrm{dc}}\cos\left(\omega t + \varphi^j\right). \tag{5.7}$$

In addition, for the neutral-shift strategy, the following requirements should be satisfied:

- Subsequent to bypassing the faulty SMs, the number of remaining healthy SMs within the faulty phase should be able to sustain the net DC-link voltage. In addition, to maintain the upper and lower arms of the faulty phase balanced, the same number of bypassed faulty SMs should be also bypassed in the complementary arm. Therefore, the following condition is required:

$$N_{\mathrm{ft}}^{j} \leq \frac{1}{2}N. \tag{5.8}$$

  If the constraint in (5.8) is violated, the faulty phase can neither provide a controllable AC voltage nor sustain the net DC-link voltage, and the MMC needs to be shut down. This means that in the phasor diagram of Fig. 5.2, the MMC cannot provide $\tilde{V}_{\mathrm{t}O,\mathrm{mr}}$ to construct the equilateral triangle.

- Based on the remaining healthy SMs, the three phases should be capable of establishing an equilateral triangle, which can be verified by

$$\hat{V}_{\mathrm{t}O,\mathrm{mx}}^{j_1} + \hat{V}_{\mathrm{t}O,\mathrm{mx}}^{j_2} \geq \hat{V}_{\mathrm{t}O,\mathrm{mx}}^{j_3}, \tag{5.9}$$

  where j_1, j_2, and j_3 need to cover all possible arrangements of the three phases. By satisfying the constraint (5.9), the MMC becomes capable of outputting balanced line-to-line voltages using the neutral-shift strategy, although the attainable voltage may not suffice to meet the demanded magnitude of voltage.

- The equilateral triangle maintained by $\hat{V}_{\mathrm{t}O,\mathrm{mx}}^{j}$ should satisfy the voltage magnitude requirement, by checking

$$\hat{V}_{\mathrm{t,ll,ref}} \leq \hat{V}_{\mathrm{t,ll,mx}}. \tag{5.10}$$

5.1.2 Circulating current suppression under the fault-tolerant strategy

In this section, the CCS method proposed in [15] is modified and used in conjunction with the neutral-shift strategy. The circulating current of phase j, i.e., i^j_{diff} is expressed by

$$i^j_{\text{diff}} = \frac{i^{p,j}_{\text{arm}} + i^{n,j}_{\text{arm}}}{2}. \tag{5.11}$$

The dynamic equation of i^j_{diff} is

$$v^j_{\text{diff}} = r i^j_{\text{diff}} + l\frac{di^j_{\text{diff}}}{dt}, \tag{5.12}$$

where

$$v^j_{\text{diff}} = \frac{V_{\text{dc}}}{2} - \frac{v^{p,j}_{\sum \text{SM}} + v^{n,j}_{\sum \text{SM}}}{2}. \tag{5.13}$$

Under normal operation, circulating currents can be decomposed into a DC component, i.e., $I^j_{\text{diff},0}$ and a negative-sequence double-frequency component as follows:

$$i^j_{\text{diff}} = I^j_{\text{diff},0} + I^-_{\text{diff},2}\sin\left(\theta_2 + \varphi^{j-}_{\text{diff},2}\right), \tag{5.14}$$

where $I^-_{\text{diff},2}$ is the magnitude of the second-order component, $\varphi^{j-}_{\text{diff},2}$ is the phase angle of the second-order component, $\theta_2 = 2\omega t$ and $I^j_{\text{diff},0}$ of the three phases all are equal to $\frac{i_{\text{dc}}}{3}$. In [15], a negative-sequence dq transformation is applied to obtain the dq components of the negative-sequence set, and, accordingly, proportional-integral (PI) controllers are used to suppress the dq components to zero.

Based on the analysis, under the neutral-shift strategy, the circulating currents in (5.11) can be decomposed into

$$\begin{aligned} i^j_{\text{diff}} &= I^j_{\text{diff},0} + I^-_{\text{diff},2}\sin\left(\theta_2 + \varphi^{j-}_{\text{diff},2}\right) + \\ & I^+_{\text{diff},2}\sin\left(\theta_2 + \varphi^{j+}_{\text{diff},2}\right) + I^z_{\text{diff},2}\sin\left(\theta_2 + \varphi^{jz}_{\text{diff},2}\right), \end{aligned} \tag{5.15}$$

where $I^{j}_{\mathrm{diff},0}$ of the three phases are different, the superscript $+$ and $-$ means the positive and negative components. Since uneven distribution of DC currents causes undesired double-frequency components in $i^{\mp}_{\mathrm{diff},dq}$, prior to dq transformation, $i^{j}_{\mathrm{diff,dc,est}}$ is removed from i^{j}_{diff}. $i^{j}_{\mathrm{diff,dc,est}}$ is the sum of two parts, i.e., prediction part and correction part. The prediction part is calculated based on the real power reference, while the correction part is obtained based on the difference between $\bar{v}^{j}_{C,\mathrm{dc}}$ and $v_{C,\mathrm{ref}}$, where $\bar{v}^{j}_{C,\mathrm{dc}}$ is the DC component of $\bar{v}^{j}_{C}$, which is illustrated in Fig. 5.3.

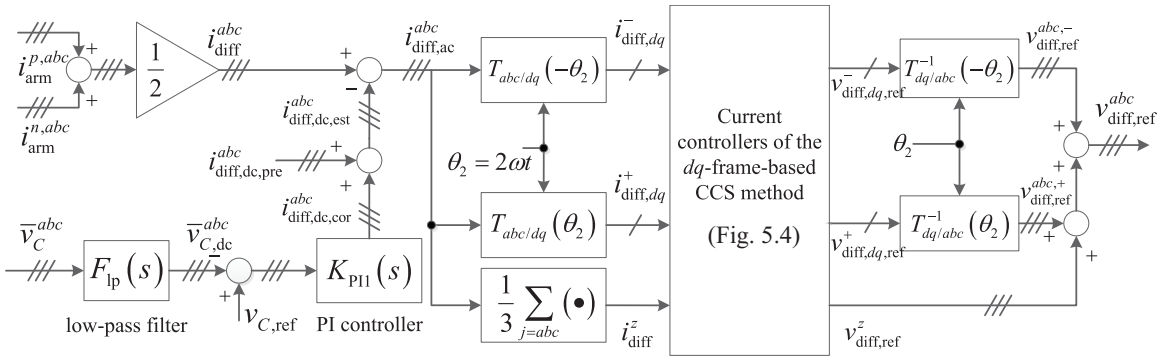

Figure 5.3: The dq-frame-based CCS method in conjunction with the neutral-shift strategy.

Since the AC component of the circulating current contains both negative- and positive-sequence components, two rotating frames are employed as follows [104]:

$$\begin{aligned} i^{-}_{\mathrm{diff},dq} &= F_{\mathrm{notch}}\left(T_{abc/dq}\left(-\theta_2\right) i^{abc}_{\mathrm{diff,ac}}\right), \\ i^{+}_{\mathrm{diff},dq} &= F_{\mathrm{notch}}\left(T_{abc/dq}\left(\theta_2\right) i^{abc}_{\mathrm{diff,ac}}\right), \end{aligned} \tag{5.16}$$

where F_{notch} are notch filter. The zero-sequence component is

$$i^{z}_{\mathrm{diff}} = \frac{1}{3}\sum_{j=a,b,c} i^{j}_{\mathrm{diff,ac}}. \tag{5.17}$$

On the basis of (5.12), (5.16), and (5.17), the dynamics of the circulating currents is ex-

pressed by:

$$\begin{aligned} v^{-}_{\mathrm{diff},dq} &= r i^{-}_{\mathrm{diff},dq} + l\frac{di^{-}_{\mathrm{diff},dq}}{dt} \pm 2\omega l i^{-}_{\mathrm{diff},qd}, \\ v^{+}_{\mathrm{diff},dq} &= r i^{+}_{\mathrm{diff},dq} + l\frac{di^{+}_{\mathrm{diff},dq}}{dt} \mp 2\omega l i^{+}_{\mathrm{diff},qd}, \\ v^{z}_{\mathrm{diff}} &= r i^{z}_{\mathrm{diff}} + l\frac{di^{z}_{\mathrm{diff}}}{dt}. \end{aligned} \tag{5.18}$$

Therefore, based on the CCS method in [15], the negative- and positive-sequence current controllers can be constructed. The zero-sequence component can be regulated with a proportional-resonant controller [105]. $v^{j,-}_{\mathrm{diff,ref}}$ and $v^{j,+}_{\mathrm{diff,ref}}$ are generated through negative- and positive-sequence inverse dq transformations. $v^{j}_{\mathrm{diff,ref}}$ is calculated by

$$v^{j}_{\mathrm{diff,ref}} = v^{j,-}_{\mathrm{diff,ref}} + v^{j,+}_{\mathrm{diff,ref}} + v^{z}_{\mathrm{diff,ref}}. \tag{5.19}$$

Furthermore, $v^{x,j}_{\sum \mathrm{SM,ref}}$ can be obtained, using [15]

$$\begin{aligned} v^{p,j}_{\sum \mathrm{SM,ref}} &= \tfrac{V_{dc}}{2} - v^{j}_{\mathrm{tO,mr}} - v^{j}_{\mathrm{diff,ref}}, \\ v^{n,j}_{\sum \mathrm{SM,ref}} &= \tfrac{V_{dc}}{2} + v^{j}_{\mathrm{tO,mr}} - v^{j}_{\mathrm{diff,ref}}. \end{aligned} \tag{5.20}$$

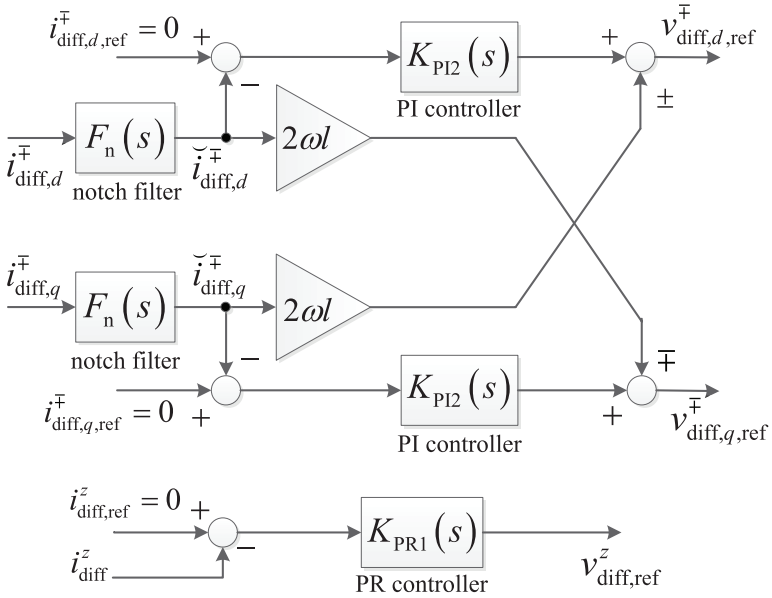

Figure 5.4: Current controllers of the dq-frame-based CCS method.

Table 5.1: Parameters of the study system of Fig. 5.1

Quantity	Value
MMC nominal power S_{b}	50 MVA
Ac system nominal voltage $V_{\mathrm{ll,rms}}$	138 kV
Ac System industance L_{AC}	150 mH
Nominal frequencies	60 Hz
R	0.03 Ω
L	5 mH
Buffer inductance l	3 mH
Series arm resistance r	0.01 Ω
Dc source voltage V_{dc}	60 kV
Number of SMs per arm N	20
Sorting period T_{sorting}	100 μs
Submodule capacitor C	14000 μF
Transformer voltage rating T	138 kV/30 kV (Y/Δ)
Transformer power rating	55 MVA
Transformer leakage reactance	5%
Transformer loss	1%

5.1.3 Simulation results

The study results are presented to evaluate the performance and effectiveness of the proposed fault-tolerant strategy. The studies are conducted in the PSCAD/EMTDC software environment. The study system is a grid-connected MMC with 20 SMs per arm, whose parameters are listed in Table 5.1. The MMC exchanges real and reactive power with the utility grid based on the closed-loop dq-current control technique, whose details are provided in [106]. Effectiveness of the neutral-shift strategy is presented in Fig. 5.5. Initially, the MMC is in its normal operating condition, where all SMs are healthy and the setpoints for real and reactive power are chosen at 54 MW and 4 MVAr, respectively. At t = 0.6 s, 4 SMs are bypassed in the upper and lower arms of phase b with no additional control action. Consequently, based on (5.1), $\hat{V}^{b}_{\mathrm{tO,mx}}$ is reduced to about $0.3V_{\mathrm{dc}}$. As illustrated in Fig. 5.5, this results in serious distortion of the AC currents, terminal voltages, transferred power, SM capacitor voltages, and arm currents. Based on Fig. 5.5, subsequent to bypassing the faulty SMs, the MMC is not able to transfer the demanded power. At t = 0.7 s, the

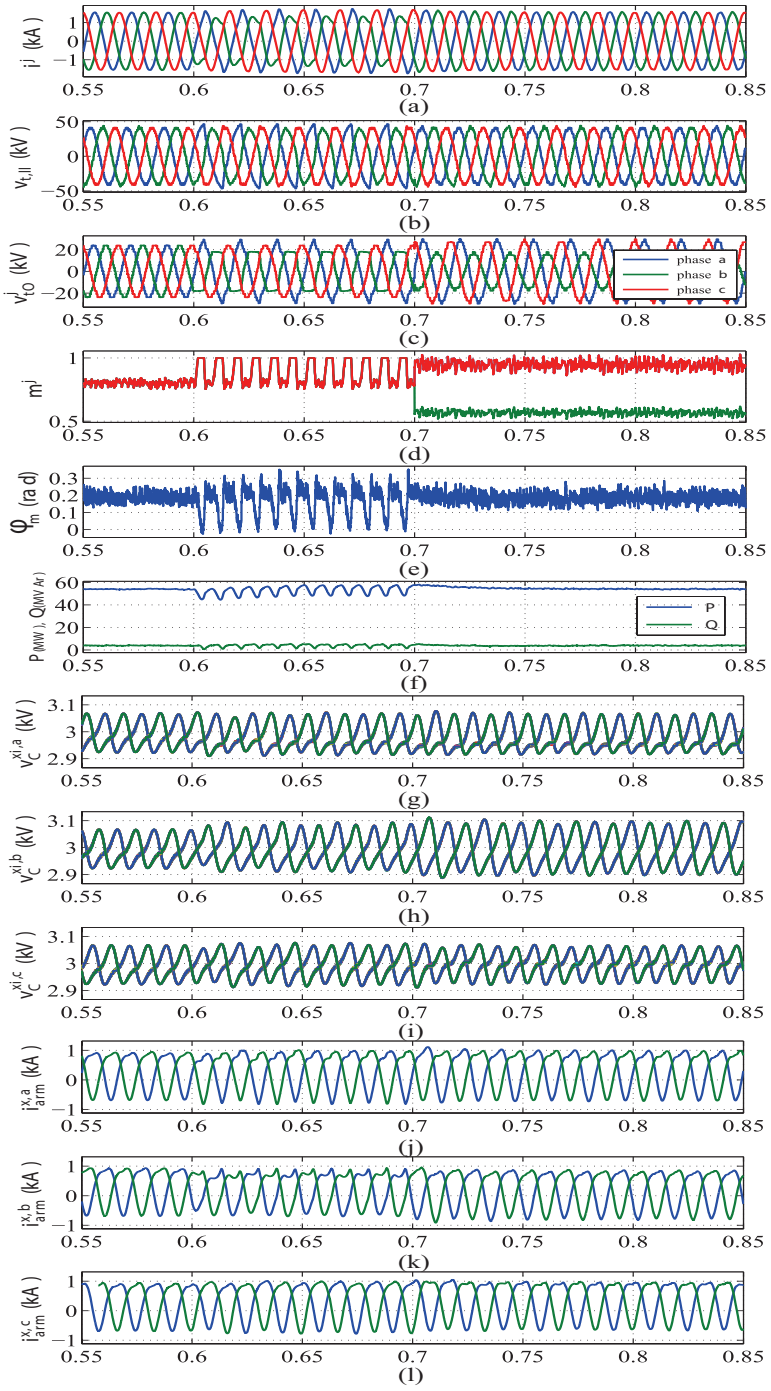

Figure 5.5: Effectiveness of the neutral-shift fault-tolerant strategy: (a) three-phase ac-side currents; (b) and (c) three-phase line-to-line and phase voltages of the MMC; (d) modulation index of the three phases; (e) modulation angle ϕ_m; (f) real and reactive power; (g), (h), and (i) SM capacitor voltages of the three phase-legs; (j), (k), and (l) arm currents of the three phase-legs.

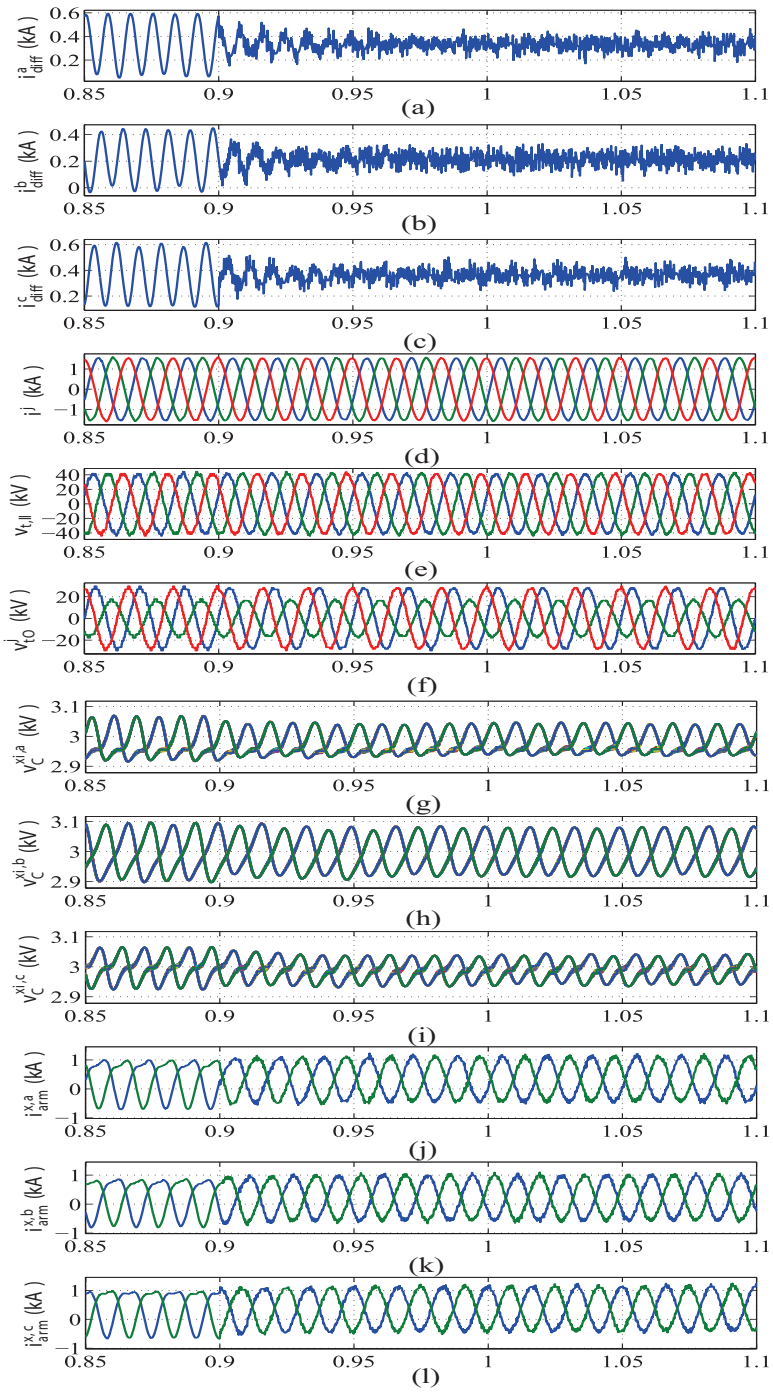

Figure 5.6: MMC waveform operating with the neutral-shift strategy when the CCS method is activated: (a), (b), and (c) circulating currents of the three phase-legs; (d) three-phase ac-side currents; (e) and (f) three-phase line-to-line and phase voltages of the MMC; (g), (h), and (i) SM capacitor voltages of the three phase-legs; (j), (k), and (l) arm currents of the three phase-legs.

neutral-shift fault-tolerant strategy is activated, in which the modified modulation indices and phase shifts are provided in the fifth row of Table II and equals 15.52°. Since for the demanded power, $\hat{V}_{\mathrm{t,ll,ref}}$ is 43.1 kV, i.e., smaller than $\hat{V}_{\mathrm{t,ll,mx}}$ = 44.2 kV based on (5.4), all the three constraints for the neutral-shift strategy are satisfied. As Fig. 5.5(d) shows, subsequent to activation of the neutral-shift strategy, the three-phase modulation indices are modified based on (5.5). In Fig. 5.5(d), m^a and m^c are overlapped since N^a_{ft} equals N^c_{ft}. Since the voltage references of the three phases are modified, the magnitude of $v^b_{\mathrm{t}O}$ is different from $v^a_{\mathrm{t}O}$ and $v^c_{\mathrm{t}O}$, as illustrated in Fig. 5.5(c). Meanwhile, the phase shifts among the three-phase voltages are displaced from 120°. Subsequently, the ac currents, line-to-line voltages, and real and reactive power are recovered to their expected waveforms, as shown in Figs. 5.5(a), (b) and (c). As shown in Figs. 5.5(g)-(i), the capacitor voltages of the healthy SMs are well regulated and balanced at their nominal value. Based on Fig. 5.5(j)-(l), under the neutral-shift fault-tolerant operation, $i^{x,j}_{\mathrm{arm}}$ remains similar to its value under normal operating conditions.

To control the circulating currents under the fault-tolerant operation with the neutral-shift strategy, the CCS method described in Fig. 5.3 is adopted. The MMC waveforms are provided in Fig. 5.6. Under operation with the neutral-shift strategy, subsequent to the activation of the CCS method at t = 0.9 s, the three-phase circulating currents, as shown in Fig. 5.6(a)-(c), are significantly reduced. Three-phase AC-side currents, line-to-line voltages, and the phase voltages keep exceptional, as shown in Fig. 5.6(d)-(f). Fig. 5.6(g)-(i) illustrate the SM capacitor voltages, which are well regulated at their reference value. Based on Fig. 5.6(j)-(l), the second-order harmonics of the arm currents are significantly reduced.

5.2 Fault-Tolerant Control of the AC-AC MMC under an External Fault

Figure 5.7 shows a schematic diagram of an AC-AC MMC. The AC-AC MMC consists of nine clusters, where each cluster is comprised of N series-connected, normally identical,

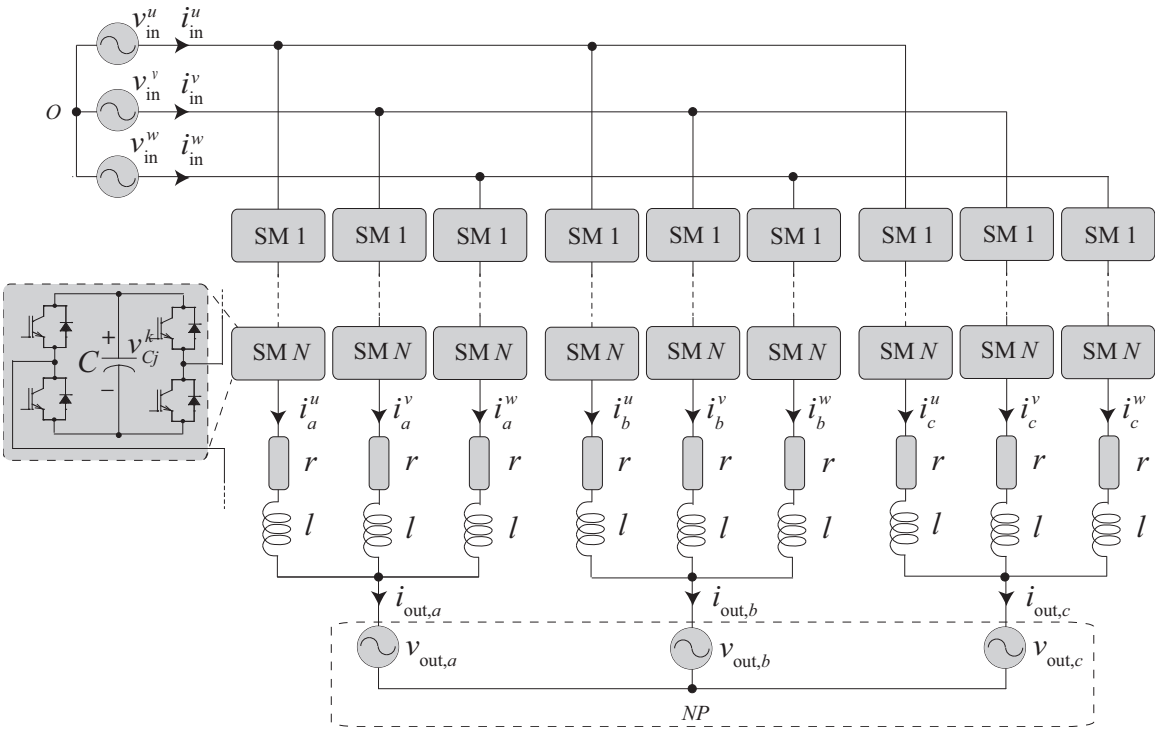

Figure 5.7: Circuit diagram of the AC-AC MMC.

full-bridge SMs, and a series-connected inductor. Input-side of the MMC is fed by a three-phase voltage source while output-side drives a three-phase machine. Basics of operation of the AC-AC MMC in Fig. 5.7 under normal operation is presented in [75]. In summary, double $\alpha\beta$ transformation is used to transform (5.21) into (5.22).

$$\begin{bmatrix} v_{\text{in}}^u & v_{\text{in}}^v & v_{\text{in}}^w \\ v_{\text{in}}^u & v_{\text{in}}^v & v_{\text{in}}^w \\ v_{\text{in}}^u & v_{\text{in}}^v & v_{\text{in}}^w \end{bmatrix} = (r + l\tfrac{d}{dt}) \begin{bmatrix} i_a^u & i_a^v & i_a^w \\ i_b^u & i_b^v & i_b^w \\ i_c^u & i_c^v & i_c^w \end{bmatrix} + \begin{bmatrix} v_{\text{cls},a}^u & v_{\text{cls},a}^v & v_{\text{cls},a}^w \\ v_{\text{cls},b}^u & v_{\text{cls},b}^v & v_{\text{cls},b}^w \\ v_{\text{cls},c}^u & v_{\text{cls},c}^v & v_{\text{cls},c}^w \end{bmatrix} + \begin{bmatrix} v_{\text{out},a} & v_{\text{out},a} & v_{\text{out},a} \\ v_{\text{out},b} & v_{\text{out},b} & v_{\text{out},b} \\ v_{\text{out},c} & v_{\text{out},c} & v_{\text{out},c} \end{bmatrix} + v_{\text{com}} \begin{bmatrix} 1 & 1 & 1 \\ 1 & 1 & 1 \\ 1 & 1 & 1 \end{bmatrix} \tag{5.21}$$

$$\begin{bmatrix} 0 & 0 & 0 \\ 0 & 0 & 0 \\ v_{\text{in}}^{\alpha} & v_{\text{in}}^{\beta} & 0 \end{bmatrix} = (r + l\frac{d}{dt}) \begin{bmatrix} i_{\alpha}^{\alpha} & i_{\alpha}^{\beta} & i_{\alpha}^{0} \\ i_{\beta}^{\alpha} & i_{\beta}^{\beta} & i_{\beta}^{0} \\ i_{0}^{\alpha} & i_{0}^{\beta} & i_{0}^{0} \end{bmatrix} + \begin{bmatrix} v_{\alpha}^{\alpha} & v_{\alpha}^{\beta} & v_{\alpha}^{0} \\ v_{\beta}^{\alpha} & v_{\beta}^{\beta} & v_{\beta}^{0} \\ v_{0}^{\alpha} & v_{0}^{\beta} & v_{0}^{0} \end{bmatrix} + \begin{bmatrix} 0 & 0 & v_{\text{out},\alpha} \\ 0 & 0 & v_{\text{out},\beta} \\ 0 & 0 & 0 \end{bmatrix} + v_{\text{com}} \begin{bmatrix} 0 & 0 & 0 \\ 0 & 0 & 0 \\ 0 & 0 & 2 \end{bmatrix} \tag{5.22}$$

The transformation matrix is

$$\mathbf{T}_{\alpha\beta} = \frac{2}{3} \begin{bmatrix} 1 & -\frac{1}{2} & -\frac{1}{2} \\ 0 & \frac{\sqrt{3}}{2} & -\frac{\sqrt{3}}{2} \\ \frac{1}{\sqrt{2}} & \frac{1}{\sqrt{2}} & \frac{1}{\sqrt{2}} \end{bmatrix}, \tag{5.23}$$

and variables in (5.21) are illustrated in Fig. 5.7, v_{com} in (5.21) represents the common-mode voltage of the output-side. Under input-side line-to-ground fault, v_{com} is different from voltage between *NP* and *O*, since zero-sequence components appear in the input-side voltages.

Applying dq transformation to $v_0^{\alpha\beta}$ and $v_{\alpha\beta}^0$ in (5.22), v_0^{dq} and v_{dq}^0 are obtained, which are controlled to regulate input- and output-side line currents respectively. Output-side common-mode voltage is inserted by controlling v_0^0, and circulating currents are injected by manipulating v_α^α, v_α^β, v_β^α and v_β^β.

5.2.1 Input- and output-side current regulation method

The input-side line currents are regulated by

$$\begin{aligned}
v_0^{q,pos*} &= v_{\text{in}}^{q,pos} - \tfrac{1}{3}\omega_{\text{in}} l i_{\text{in}}^{d,pos} + PI_1(s)\,(I_{\text{in}}^{q,pos*} - i_{\text{in}}^{q,pos}),\\
v_0^{d,pos*} &= v_{\text{in}}^{d,pos} + \tfrac{1}{3}\omega_{\text{in}} l i_{\text{in}}^{q,pos} + PI_1(s)\,(I_{\text{in}}^{d,pos*} - i_{\text{in}}^{d,pos}),\\
v_0^{q,neg*} &= v_{\text{in}}^{q,neg} - \tfrac{1}{3}\omega_{\text{in}} l i_{\text{in}}^{d,neg} + PI_1(s)\,(I_{\text{in}}^{q,neg*} - i_{\text{in}}^{q,neg}),\\
v_0^{d,neg*} &= v_{\text{in}}^{d,neg} + \tfrac{1}{3}\omega_{\text{in}} l i_{\text{in}}^{q,neg} + PI_1(s)\,(I_{\text{in}}^{d,neg*} - i_{\text{in}}^{d,neg}),
\end{aligned} \tag{5.24}$$

where v_{in}^{dq} and i_{in}^{dq} are dq-axis components of the input-side voltages and currents respectively, the asterisk superscripts denote references of the corresponding variables, the superscripts of pos and neg denote positive- and negative-sequence components, respectively, ω_{in} is the input-side angular frequency, and PI denotes proportional-integral (PI) controller. Since the input-side line-to-ground fault causes negative- and zero-sequence voltage components, current references are derived as follows to maintain power transfer capability and keep capacitor voltages of all clusters balanced.

Power of a cluster is expressed by:

$$p_j^k = (v_{\text{in}}^k - v_{\text{out},j} - v_{\text{com}})(\tfrac{1}{3} i_{\text{in}}^k + \tfrac{1}{3} i_{\text{out},j} + i_{\text{cir},j}^k), \tag{5.25}$$

where $i_{\text{cir},j}^k$ is circulating current of the cluster. Under input-side line-to-ground fault condition, input-side voltage and current of phase u are expressed as

$$\begin{aligned}
v_{\text{in}}^u &= \hat{V}_{\text{in}}^{pos} \sin(\omega_{\text{in}} t) + \hat{V}_{\text{in}}^{neg} \sin(\omega_{\text{in}} t + \delta^{neg}) + \hat{V}_{\text{in}}^{zero} \sin(\omega_{\text{in}} t + \delta^{zero}),\\
i_{\text{in}}^u &= \hat{I}_{\text{in}}^{pos} \sin(\omega_{\text{in}} t + \phi_{\text{in}}^{pos}) + \hat{I}_{\text{in}}^{neg} \sin(\omega_{\text{in}} t + \delta^{neg} + \phi_{\text{in}}^{neg}),
\end{aligned} \tag{5.26}$$

where i_{in}^u does not contain any zero-sequence component, as there is no zero-sequence

current path. The output-side voltage and current of phase a are expressed as

$$\begin{aligned} v_{\mathrm{out},a} &= \hat{V}_{\mathrm{out}} \sin(\omega_{\mathrm{out}} t + \delta_{\mathrm{out}}), \\ i_{\mathrm{out},a} &= \hat{I}_{\mathrm{out}} \sin(\omega_{\mathrm{out}} t + \delta_{\mathrm{out}} + \phi_{\mathrm{out}}). \end{aligned} \tag{5.27}$$

Substituting (5.26) and (5.27) for v_{in}^{u}, i_{in}^{u}, $v_{\mathrm{out},a}$ and $i_{\mathrm{out},a}$ in (5.25), DC components in p_a^u could be found:

$$\begin{aligned} p_{a,\mathrm{dc}}^{u} = {} & \hat{V}_{\mathrm{in}}^{pos} \hat{I}_{\mathrm{in}}^{pos} \cos(\phi_{\mathrm{in}}^{pos}) + \hat{V}_{\mathrm{in}}^{neg} \hat{I}_{\mathrm{in}}^{neg} \cos(\phi_{\mathrm{in}}^{neg}) - \hat{V}_{\mathrm{out}} \hat{I}_{\mathrm{out}} \cos(\phi_{\mathrm{out}}) \\ & + \hat{V}_{\mathrm{in}}^{pos} \hat{I}_{\mathrm{in}}^{neg} \cos(\delta^{neg} + \phi_{\mathrm{in}}^{neg}) + \hat{V}_{\mathrm{in}}^{neg} \hat{I}_{\mathrm{in}}^{pos} \cos(\delta^{neg} - \phi_{\mathrm{in}}^{pos}). \end{aligned} \tag{5.28}$$

Since $p_{a,\mathrm{dc}}^{u}$, $p_{a,\mathrm{dc}}^{v}$, and $p_{a,\mathrm{dc}}^{w}$ should equal zero in steady state, the following control objects are obtained:

$$\hat{V}_{\mathrm{in}}^{pos} \hat{I}_{\mathrm{in}}^{pos} \cos(\phi_{\mathrm{in}}^{pos}) + \hat{V}_{\mathrm{in}}^{neg} \hat{I}_{\mathrm{in}}^{neg} \cos(\phi_{\mathrm{in}}^{neg}) = \hat{V}_{\mathrm{out}} \hat{I}_{\mathrm{out}} \cos(\phi_{\mathrm{out}}), \tag{5.29}$$

$$\hat{V}_{\mathrm{in}}^{pos} \hat{I}_{\mathrm{in}}^{neg} \cos(\delta^{neg} + \phi_{\mathrm{in}}^{neg}) + \hat{V}_{\mathrm{in}}^{neg} \hat{I}_{\mathrm{in}}^{pos} \cos(\delta^{neg} - \phi_{\mathrm{in}}^{pos}) = 0, \tag{5.30}$$

$$\hat{V}_{\mathrm{in}}^{pos} \hat{I}_{\mathrm{in}}^{neg} \cos(\delta^{neg} + \phi_{\mathrm{in}}^{neg} - \tfrac{2\pi}{3}) + \hat{V}_{\mathrm{in}}^{neg} \hat{I}_{\mathrm{in}}^{pos} \cos(\delta^{neg} - \phi_{\mathrm{in}}^{pos} - \tfrac{2\pi}{3}) = 0, \tag{5.31}$$

$$\hat{V}_{\mathrm{in}}^{pos} \hat{I}_{\mathrm{in}}^{neg} \cos(\delta^{neg} + \phi_{\mathrm{in}}^{neg} + \tfrac{2\pi}{3}) + \hat{V}_{\mathrm{in}}^{neg} \hat{I}_{\mathrm{in}}^{pos} \cos(\delta^{neg} - \phi_{\mathrm{in}}^{pos} + \tfrac{2\pi}{3}) = 0. \tag{5.32}$$

Since only two out of (5.30), (5.31) and (5.32) are independent, three control objects with respect to $\hat{I}_{\mathrm{in}}^{pos}$, $\hat{I}_{\mathrm{in}}^{neg}$, ϕ_{in}^{pos}, and ϕ_{in}^{neg} are found. If a proper definition of reactive power under unbalanced condition is provided as the fourth control object, unique $\hat{I}_{\mathrm{in}}^{pos}$, $\hat{I}_{\mathrm{in}}^{neg}$, ϕ_{in}^{pos}, and ϕ_{in}^{neg} can be derived. In this paper, for simplicity, the fourth control object is

$$\hat{V}_{\mathrm{in}}^{pos} \hat{I}_{\mathrm{in}}^{neg} = \hat{V}_{\mathrm{in}}^{neg} \hat{I}_{\mathrm{in}}^{pos}, \tag{5.33}$$

which is equivalent to $Q = 0$ under normal operating condition. Besides, to compensate power loss in the converter, (5.29) is modified into

$$\hat{V}_{\text{in}}^{pos}\hat{I}_{\text{in}}^{pos}\cos(\phi_{\text{in}}^{pos}) + \hat{V}_{\text{in}}^{neg}\hat{I}_{\text{in}}^{neg}\cos(\phi_{\text{in}}^{neg}) = P^*, \tag{5.34}$$

where

$$P^* \triangleq \hat{V}_{\text{out}}\hat{I}_{\text{out}}\cos(\phi_{\text{out}}) - PI_2\left(\frac{1}{9}\sum_{k,j} v_{Cj}^k - V_C^*\right). \tag{5.35}$$

Solving (5.30), (5.31), (5.33), and (5.34), references of $\hat{I}_{\text{in}}^{pos}$, $\hat{I}_{\text{in}}^{neg}$, ϕ_{in}^{pos}, and ϕ_{in}^{neg} are:

$$\begin{aligned}
\hat{I}_{\text{in}}^{pos*} &= \tfrac{2}{3}P^*/(\hat{V}_{\text{in}}^{pos} - \tfrac{(\hat{V}_{\text{in}}^{neg})^2}{\hat{V}_{\text{in}}^{pos}}),\\
\phi_{\text{in}}^{pos*} &= 0,\\
\hat{I}_{\text{in}}^{neg*} &= \tfrac{\hat{V}_{\text{in}}^{neg}}{\hat{V}_{\text{in}}^{pos}}\hat{I}_{\text{in}}^{pos*},\\
\phi_{\text{in}}^{neg*} &= \pi.
\end{aligned} \tag{5.36}$$

Therefore, the current references in (5.24) are

$$\begin{aligned}
I_{\text{in}}^{q,pos*} &= \hat{I}_{\text{in}}^{pos*}\cos(\phi_{\text{in}}^{pos}) = \tfrac{2}{3}P^*/(\hat{V}_{\text{in}}^{pos} - \tfrac{(\hat{V}_{\text{in}}^{neg})^2}{\hat{V}_{\text{in}}^{pos}}),\\
I_{\text{in}}^{d,pos*} &= \hat{I}_{\text{in}}^{pos*}\sin(\phi_{\text{in}}^{pos}) = 0,\\
I_{\text{in}}^{q,neg*} &= -\hat{I}_{\text{in}}^{neg*}\cos(\phi_{\text{in}}^{neg}) = \tfrac{\hat{V}_{\text{in}}^{neg}}{\hat{V}_{\text{in}}^{pos}}\hat{I}_{\text{in}}^{pos*},\\
I_{\text{in}}^{d,neg*} &= \hat{I}_{\text{in}}^{neg*}\sin(\phi_{\text{in}}^{neg}) = 0.
\end{aligned} \tag{5.37}$$

In addition, since the phase angle of the negative-sequence component is needed to maintain capacitor voltages balanced and mitigate large capacitor voltage fluctuations, the phase-locked loop (PLL) is modified as shown in Fig. 5.8, where $F_n(s)$ represents a notch filter to remove the second-order frequency component.

The output-side current regulation method depends on specific electric machine drive method, e.g., flux-oriented method or direct-torque method, which provides v_{dq}^{0*} to the control system of the AC-AC MMC.

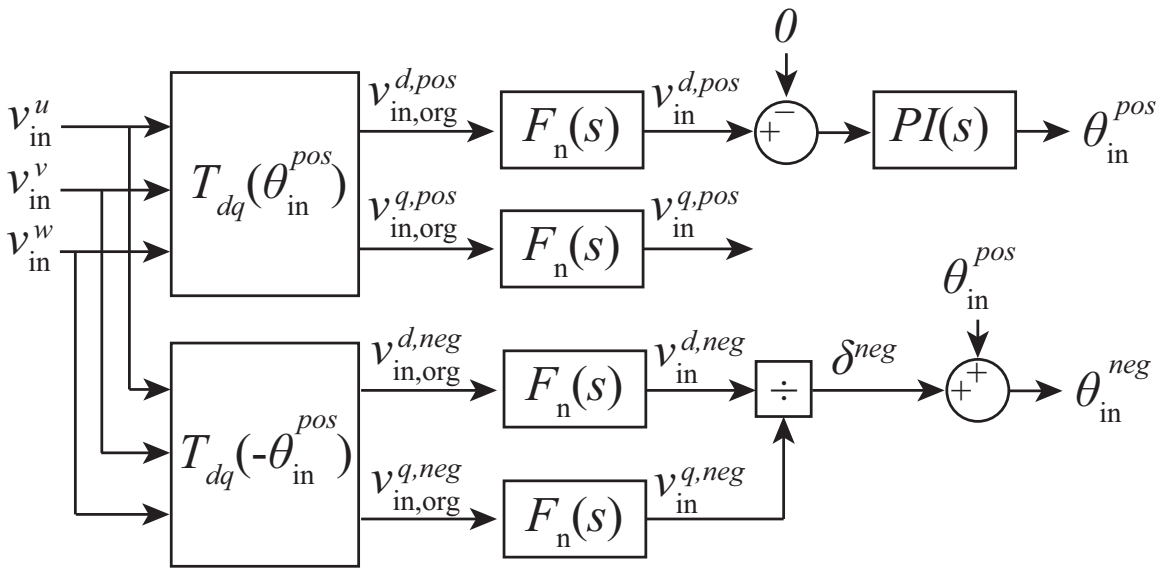

Figure 5.8: Block diagram of the PLL.

Capacitor Voltage Balancing Method

In the existing capacitor voltage balancing methods, circulating currents and/or output-side common-mode voltage are injected to adjust power of each cluster [107, 108]. The capacitor voltage balancing method is based on

$$v_{Cj}^{k} = V_C^* + \frac{1}{NCV_C^*}\int p_j^k dt \tag{5.38}$$

and double $\alpha\beta$-transformation, i.e.,

$$\left[v_{C\alpha\beta0}^{\alpha\beta0}\right] = \begin{bmatrix} v_{C\alpha}^{\alpha} & v_{C\alpha}^{\beta} & v_{C\alpha}^{0} \\ v_{C\beta}^{\alpha} & v_{C\beta}^{\beta} & v_{C\beta}^{0} \\ v_{C0}^{\alpha} & v_{C0}^{\beta} & v_{C0}^{0} \end{bmatrix} = \mathbf{T}_{\alpha\beta} \begin{bmatrix} v_{Ca}^{u} & v_{Ca}^{v} & v_{Ca}^{w} \\ v_{Cb}^{u} & v_{Cb}^{v} & v_{Cb}^{w} \\ v_{Cc}^{u} & v_{Cc}^{v} & v_{Cc}^{w} \end{bmatrix} \mathbf{T}_{\alpha\beta}^{T}, \tag{5.39}$$

where v_{Cj}^{k} is average capacitor voltage of a cluster. Based on (5.38) and (5.39), each element in $\left[v_{C\alpha\beta0}^{\alpha\beta0}\right]$ is positively correlated to the element that in the same position in $\left[p_{\alpha\beta0}^{\alpha\beta0}\right]$.

Under input-side line-to-ground fault condition, input-side voltages contain both positive-

and negative-sequence components:

$$\begin{aligned} v_{\text{in}}^{\alpha} &= v_{\text{in}}^{\alpha,pos} + v_{\text{in}}^{\alpha,neg} = \hat{V}_{\text{in}}^{pos}\sin(\theta_{\text{in}}^{pos}) + \hat{V}_{\text{in}}^{neg}\sin(\theta_{\text{in}}^{neg}) = \hat{V}_{\text{in}}^{\alpha}\sin(\omega_{\text{in}}t + \delta^{\alpha}), \\ v_{\text{in}}^{\beta} &= v_{\text{in}}^{\beta,pos} + v_{\text{in}}^{\beta,neg} = -\hat{V}_{\text{in}}^{pos}\cos(\theta_{\text{in}}^{pos}) + \hat{V}_{\text{in}}^{neg}\cos(\theta_{\text{in}}^{neg}) = \hat{V}_{\text{in}}^{\beta}\cos(\omega_{\text{in}}t + \delta^{\beta}), \end{aligned} \tag{5.40}$$

where

$$\begin{aligned} \hat{V}_{\text{in}}^{\alpha} &= \sqrt{(\hat{V}_{\text{in}}^{pos})^2 + (\hat{V}_{\text{in}}^{neg})^2 + 2\hat{V}_{\text{in}}^{pos}\hat{V}_{\text{in}}^{neg}\cos(\delta^{neg})}, \\ \delta^{\alpha} &= \arcsin(\tfrac{\hat{V}_{\text{in}}^{neg}}{\hat{V}_{\text{in}}^{\alpha}}\sin(\delta^{neg})), \\ \hat{V}_{\text{in}}^{\beta} &= \sqrt{(\hat{V}_{\text{in}}^{pos})^2 + (\hat{V}_{\text{in}}^{neg})^2 - 2\hat{V}_{\text{in}}^{pos}\hat{V}_{\text{in}}^{neg}\cos(\delta^{neg})}, \\ \delta^{\beta} &= -\arcsin(\tfrac{\hat{V}_{\text{in}}^{neg}}{\hat{V}_{\text{in}}^{\beta}}\sin(\delta^{neg})) + \pi. \end{aligned} \tag{5.41}$$

Based on (5.40), the following circulating currents could be injected to compensate $v_{C\alpha}^{0}$ and $v_{C\beta}^{0}$.

$$\begin{bmatrix} i_{\alpha 1}^{\alpha *} & i_{\alpha 1}^{\beta *} \\ i_{\beta 1}^{\alpha *} & i_{\beta 1}^{\beta *} \end{bmatrix} = -K_1 \begin{bmatrix} v_{C\alpha}^{0}\sin(\theta_{\text{in}}^{pos} + \delta^{\alpha}) & v_{C\alpha}^{0}\cos(\theta_{\text{in}}^{pos} + \delta^{\beta}) \\ v_{C\beta}^{0}\sin(\theta_{\text{in}}^{pos} + \delta^{\alpha}) & v_{C\beta}^{0}\cos(\theta_{\text{in}}^{pos} + \delta^{\beta}) \end{bmatrix}. \tag{5.42}$$

The output-side voltages remain to be balanced, so the following circulating currents can be injected to compensate v_{C0}^{α} and v_{C0}^{β}:

$$\begin{bmatrix} i_{\alpha 2}^{\alpha *} & i_{\alpha 2}^{\beta *} \\ i_{\beta 2}^{\alpha *} & i_{\beta 2}^{\beta *} \end{bmatrix} = K_2 \begin{bmatrix} -v_{C0}^{\alpha}\sin\theta_{\text{out}} & -v_{C0}^{\beta}\sin\theta_{\text{out}} \\ v_{C0}^{\alpha}\cos\theta_{\text{out}} & v_{C0}^{\beta}\cos\theta_{\text{out}} \end{bmatrix}, \tag{5.43}$$

where

$$\theta_{\text{out}} = \omega_{\text{out}}t + \delta_{\text{out}}. \tag{5.44}$$

Besides, circulating currents that are used to compensate $v_{C\alpha}^{\alpha}$, $v_{C\alpha}^{\beta}$, $v_{C\beta}^{\alpha}$, and $v_{C\beta}^{\beta}$ could be

$$\begin{aligned}
i_{\alpha 3}^{\alpha *} &= K_3(v_{C\alpha}^{\alpha}\sin(\theta_{\text{out}}) + v_{C\beta}^{\alpha}\cos(\theta_{\text{out}})),\\
i_{\alpha 3}^{\beta *} &= K_3(-v_{C\beta}^{\alpha}\sin(\theta_{\text{out}}) + v_{C\alpha}^{\alpha}\cos(\theta_{\text{out}})),\\
i_{\beta 3}^{\alpha *} &= K_3(v_{C\beta}^{\beta}\cos(\theta_{\text{out}}) + v_{C\alpha}^{\beta}\sin(\theta_{\text{out}})),\\
i_{\beta 3}^{\beta *} &= K_3(v_{C\alpha}^{\beta}\cos(\theta_{\text{out}}) - v_{C\beta}^{\beta}\sin(\theta_{\text{out}})).
\end{aligned} \tag{5.45}$$

In addition, the average capacitor voltage of all clusters is regulated by (5.34).

5.2.2 Capacitor voltage fluctuation mitigation method

If the output-side frequency, i.e., f_{out} is close to the input-side frequency, i.e., f_{in}, low-frequency components will appear in the power of clusters, i.e., p_j^k, causing large fluctuation of SM capacitor voltages [79]. Based on (5.25), (5.26), and (5.27), under input-side line-to-ground fault, the low-frequency components in p_a^u are

$$\begin{aligned}
p_{a,\text{lf}}^u = \tfrac{1}{6}[&-\hat{V}_{\text{out}}\hat{I}_{\text{in}}^{pos}\cos((\omega_{\text{in}}-\omega_{\text{out}})t - \delta_{\text{out}} + \phi_{\text{in}}^{pos})\\
&- \hat{V}_{\text{out}}\hat{I}_{\text{in}}^{neg}\cos((\omega_{\text{in}}-\omega_{\text{out}})t - \delta_{\text{out}} + \delta^{neg} + \phi_{\text{in}}^{neg})\\
&+ \hat{V}_{\text{in}}^{pos}\hat{I}_{\text{out}}\cos((\omega_{\text{in}}-\omega_{\text{out}})t - \delta_{\text{out}} - \phi_{\text{out}})\\
&+ \hat{V}_{\text{in}}^{neg}\hat{I}_{\text{out}}\cos((\omega_{\text{in}}-\omega_{\text{out}})t + \delta^{neg} - \delta_{\text{out}} - \phi_{\text{out}})].
\end{aligned} \tag{5.46}$$

To remove the low-frequency components, i.e., $p_{j,\text{lf}}^k$, sinusoidal common-mode voltage and corresponding circulating currents are injected:

$$\begin{aligned}
v_{\text{com}}^{*} &= \hat{V}_{\text{com}}\sin(\omega_{\text{com}}t) - v_{\text{in}}^{zero},\\
i_{\text{cir,lf},j}^{k*} &= 2\tfrac{p_{j,\text{lf}}^k}{\hat{V}_{\text{com}}}\sin(\omega_{\text{com}}t),
\end{aligned} \tag{5.47}$$

where $\hat{V}_{\text{com}}$ and ω_{com} are magnitude and angular frequency of the common-mode voltage and v_{in}^{zero} is the zero-sequence component of input-side voltages.

5.2.3 Simulation results

In this section, study results conducted in the PSCAD/EMTDC software environment are presented to verify the effectiveness of the proposed methods. The parameters of the study system are listed in Table 5.2. The permanent magnetic synchronous machine (PMSM) is loaded at the rated torque. Flux-oriented control is applied to the PMSM. The overall control system is provided in Fig. 5.9. Input-side currents are controlled by the method developed in Section 5.2.1, where setpoint of reactive power is zero.

Fig. 5.10 shows converter waveforms under the proposed post-fault strategy when $f_{\rm in}$ is the same as $f_{\rm out}$, i.e., 50 Hz, when the proposed methods in Section 5.2 are employed. At $t = 1.2$ s, a line-to-ground fault occurs at the input-side phase-u, as illustrated in Fig. 5.10(a). Fig. 5.10(b) illustrates that input-side currents, which are well regulated to contain proper positive- and negative-components subsequent to the fault. The output-side voltages and currents are maintained to be normal as shown in Figs. 5.10(c) and (d), which presents fault ride through capability of the proposed post-fault strategy. The proposed methods regulate the capacitor voltages within $\pm\ 3\ \%$ of the V_C^* prior and subsequent to the fault, as illustrated in Figs. 5.10(e), (f), and (g). Fig. 5.10 (h) illustrates the instantaneous input-side power based on

$$p_{\rm in} = v_{\rm in}^u i_{\rm in}^u + v_{\rm in}^v i_{\rm in}^v + v_{\rm in}^w i_{\rm in}^w. \tag{5.48}$$

As illustrated in Fig. 5.10 (h), subsequent to the line-to-ground fault, power that flows into the converter is slightly higher than that prior to the fault. The difference is caused by larger power losses in the converter, since larger currents are needed to reach the power transfer requirement. Fig. 5.11 presents the waveforms when $f_{\rm out}$ is at 75 Hz. Under such $f_{\rm out}$, the inherent capacitor voltage fluctuation problem does not appear. Therefore, only the input-side current regulation method and capacitor voltage balancing method are applied. Fig. 5.11(b) shows that input-side currents, which are well regulated to contain proper

positive- and negative-components subsequent to the fault. The output-side voltages and currents are not impacted by the fault, as illustrated in Figs. 5.11(c), and (d). Capacitor voltages are still balanced, as illustrated in Figs. 5.11(e)-(g). The instantaneous power that flows into the converter from the input-side is provided in Fig. 5.11(h), which illustrates that the converter is still capable of transferring required power while the power losses are higher subsequent to the fault.

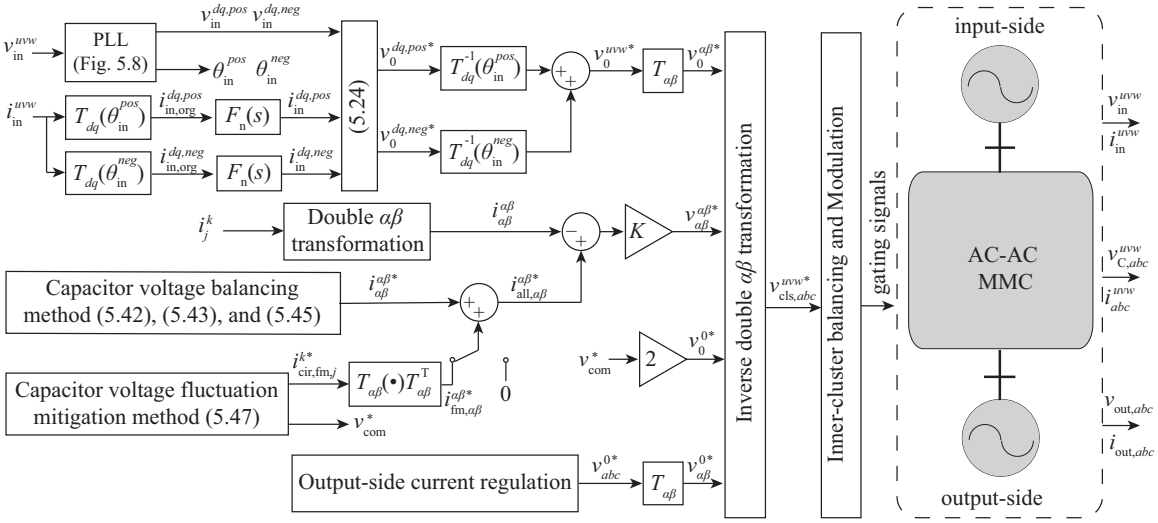

Figure 5.9: Overall control block diagram of the AC-AC MMC.

5.3 Fault-Tolerant Control for the AC-AC MMC under Internal SM Faults

To maintain voltage output capability of the faulty cluster, subsequent to bypassing the faulty SMs, the reference of the capacitor voltages in the faulty cluster can be modified to:

$$V_{Cj,\mathrm{ft}}^{k*} = \frac{N}{N_j^k} V_{Cj}^{k*}. \tag{5.49}$$

On the other hand, the capacitor voltage balancing method along with the SM capacitor voltage fluctuation mitigation method, which are abbreviated as v_C-balancing method and $\tilde{v}_C$-mitigation method in the following paragraphs, need to be modified. Instead of depending on the average capacitor voltages of each cluster, i.e., $\bar{v}_{Cj}^k$, the modified control strategy

Table 5.2: Parameters of the study system

Quantity	Value
Nominal power of AC-AC MMC S_{b}	5 kVA
Input-side AC system nominal voltage $V_{\mathrm{in,ll,rms}}$	400 V
Nominal frequency of input-side AC system f_{in}	50 Hz
Series-connected inductance l	10 mH
Resistance of series-connected inductor r	1 mΩ
Submodule capacitor C	1700 μF
Number of SMs in each cluster N	4
Capacitor voltage reference V_C^*	300 V
Rated power of PMSM P_{outr}	5 kW
Rated voltage of PMSM $V_{\mathrm{out,ll,rms}}$	400 V
Rated frequency of PMSM f_{out}	75 Hz
Stator winding resistance	0.46 Ω
Stator leakage reactance	4 mH
Unsaturated reactance in d-axis	20 mH
Unsaturated reactance in q-axis	20 mH

relies on the differences between $\bar{v}_{Cj}^k$ and V_{Cj}^{k*}, which can be defined as:

$$\Delta v_{Cj}^k = \frac{V_{Cj}^{k*}}{V_C^*}(\bar{v}_{Cj}^k - v_{Cj}^{k*}). \tag{5.50}$$

The overall v_C-balancing method is modified to be:

$$\begin{aligned} i_{\mathrm{in}}^{d*} &= \tfrac{p_{\mathrm{out}}^*}{v_{\mathrm{in}}^d} - \left(K_{\mathrm{P1}} + \tfrac{K_{\mathrm{I1}}}{s}\right) \sum_{k,j} \Delta v_{Cj}^k \\ i_{\mathrm{in}}^{q*} &= \tfrac{q_{\mathrm{in}}^*}{v_{\mathrm{in}}^d}, \end{aligned} \tag{5.51}$$

where p_{out}^* is the real power fed into the motor, q_{in}^* is the commanded reactive power absorbed by the AC-AC MMC. In addition to the overall average capacitor voltage regulation, energy differences among the clusters need to be suppressed to maintain Δv_{Cj}^k close to zero. Therefore, circulating currents need to be injected based on the capacitor voltage difference

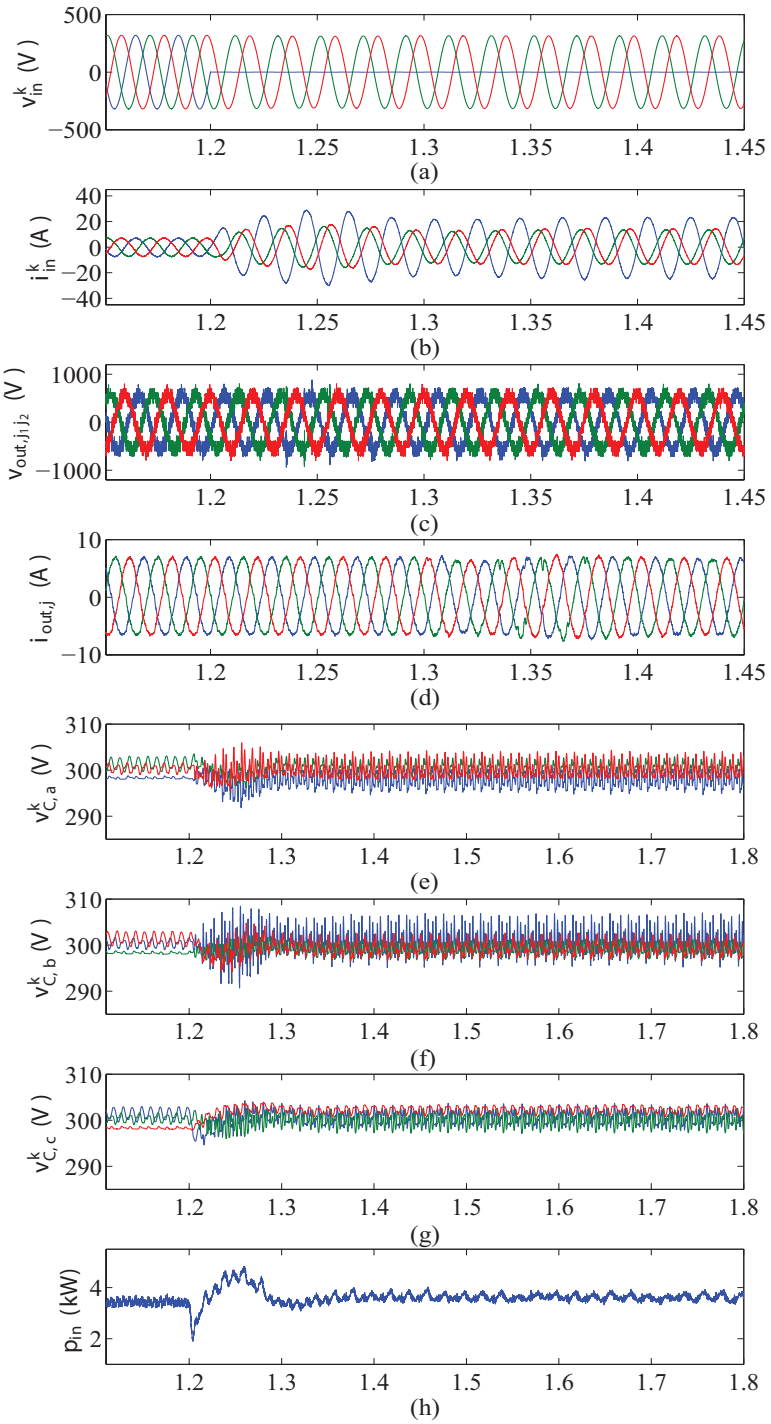

Figure 5.10: Converter waveforms under the input-side line-to-ground fault conditions (f_{out} is the same with f_{in}, i.e., 50Hz): (a,b) input-side voltages and currents v_{in}^k and i_{in}^k ($k = u, v, w$), (c,d) output-side voltages and currents $v_{\text{out},j}$ and $i_{\text{out},j}$ ($j = a, b, c$), (e-g) capacitor voltages $v_{C,j}^k$, and (h) input-side instantaneous power p_{in}.

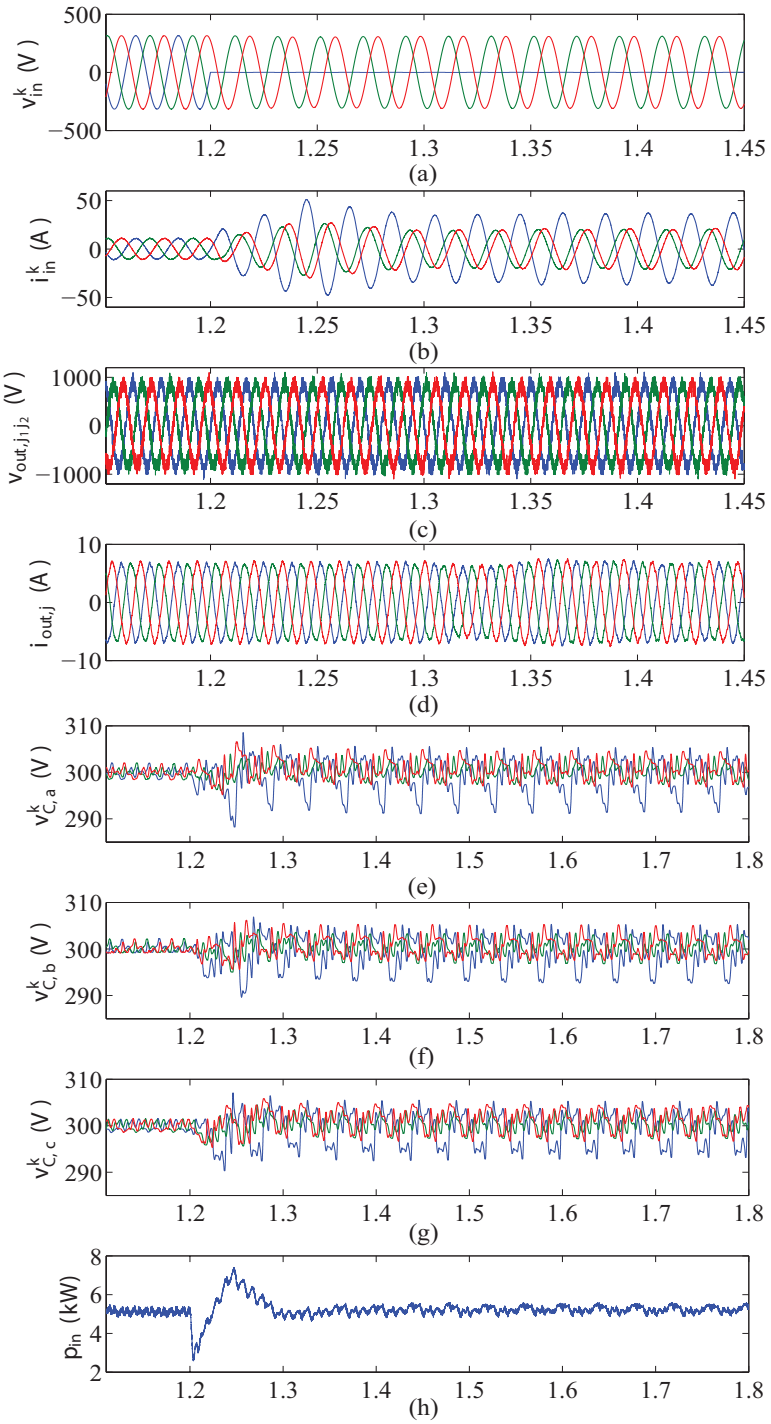

Figure 5.11: Converter waveforms under the input-side line-to-ground fault conditions (f_{out} is the rated frequency of the electric machine, i.e., 75Hz): (a,b) input-side voltages and currents v_{in}^k and i_{in}^k ($k = u, v, w$), (c,d) output-side voltages and currents $v_{\text{out},j}$ and $i_{\text{out},j}$ ($j = a, b, c$), (e-g) capacitor voltages $v_{C,j}^k$, and (h) input-side instantaneous power p_{in}.

matrix in the $\alpha\beta$ frame, i.e., $\left[\Delta v_{C\alpha\beta 0}^{\alpha\beta 0}\right]$:

$$\left[\Delta v_{C\alpha\beta 0}^{\alpha\beta 0}\right] = \begin{bmatrix} \Delta v_{C\alpha}^{\alpha} & \Delta v_{C\alpha}^{\beta} & \Delta v_{C\alpha}^{0} \\ \Delta v_{C\beta}^{\alpha} & \Delta v_{C\beta}^{\beta} & \Delta v_{C\beta}^{0} \\ \Delta v_{C0}^{\alpha} & \Delta v_{C0}^{\beta} & \Delta v_{C0}^{0} \end{bmatrix} = \mathbf{T}_{\alpha\beta} \begin{bmatrix} \Delta v_{Ca}^{u} & \Delta v_{Ca}^{v} & \Delta v_{Ca}^{w} \\ \Delta v_{Cb}^{u} & \Delta v_{Cb}^{v} & \Delta v_{Cb}^{w} \\ \Delta v_{Cc}^{u} & \Delta v_{Cc}^{v} & \Delta v_{Cc}^{w} \end{bmatrix} \mathbf{T}_{\alpha\beta}^{T}, \tag{5.52}$$

where

$$\mathbf{T}_{\alpha\beta} = \begin{bmatrix} \frac{2}{3} & -\frac{1}{3} & -\frac{1}{3} \\ 0 & \frac{\sqrt{3}}{3} & -\frac{\sqrt{3}}{3} \\ \frac{1}{3} & \frac{1}{3} & \frac{1}{3} \end{bmatrix}. \tag{5.53}$$

To suppress $\Delta v_{C\alpha}^{0}$, $\Delta v_{C\beta}^{0}$, Δv_{C0}^{α}, and Δv_{C0}^{β}, circulating currents need to be injected as follows:

$$\begin{aligned} i_{\alpha 1}^{\alpha *} &= -K_1 \Delta v_{C\alpha}^{0} \sin\theta_{\text{in}} - K_2 \Delta v_{C0}^{\alpha} \sin\theta_{\text{out}}, \\ i_{\alpha 1}^{\beta *} &= K_1 \Delta v_{C\alpha}^{0} \cos\theta_{\text{in}} - K_2 \Delta v_{C0}^{\beta} \sin\theta_{\text{out}}, \\ i_{\beta 1}^{\alpha *} &= -K_1 \Delta v_{C\beta}^{0} \sin\theta_{\text{in}} + K_2 \Delta v_{C0}^{\alpha} \cos\theta_{\text{out}}, \\ i_{\beta 1}^{\beta *} &= K_1 \Delta v_{C\beta}^{0} \cos\theta_{\text{in}} + K_2 \Delta v_{C0}^{\beta} \cos\theta_{\text{out}}, \end{aligned} \tag{5.54}$$

where θ_{in} is the phase of v_{in}^{u} and θ_{out} is the phase of $v_{\text{in},a}$. Besides, $\Delta v_{C\alpha}^{\alpha}$, $\Delta v_{C\beta}^{\alpha}$, $\Delta v_{C\alpha}^{\beta}$, and $\Delta v_{C\beta}^{\beta}$ can be regulated around 0 by injecting

$$\begin{aligned} i_{\alpha 2}^{\alpha *} &= -K_3(\Delta v_{C\alpha}^{\alpha} \sin\theta_{\text{in}} + \Delta v_{C\alpha}^{\alpha} \cos\theta_{\text{in}}), \\ i_{\alpha 2}^{\beta *} &= -K_3(\Delta v_{C\alpha}^{\beta} \cos\theta_{\text{in}} - \Delta v_{C\alpha}^{\beta} \sin\theta_{\text{in}}), \\ i_{\beta 2}^{\alpha *} &= -K_3(\Delta v_{C\beta}^{\alpha} \sin\theta_{\text{in}} + \Delta v_{C\beta}^{\alpha} \cos\theta_{\text{in}}), \\ i_{\beta 2}^{\beta *} &= -K_3(\Delta v_{C\beta}^{\beta} \cos\theta_{\text{in}} - \Delta v_{C\beta}^{\beta} \sin\theta_{\text{in}}). \end{aligned} \tag{5.55}$$

In addition, the sorting-based voltage balancing method should sort Δv_{Cj}^{k} instead of $\bar{v}_{Cj}^{k}$.

5.3.1 The proposed capacitor voltage fluctuation mitigation methods

If the output-side frequency, i.e., $f_{\rm out}$ is close to the input-side frequency, i.e., $f_{\rm in}$, low-frequency components will appear in the power of the clusters, i.e., p_j^k, causing large fluctuation of the SM capacitor voltages [79]. If $f_{\rm out}$ equals to $f_{\rm in}$, the dc components in p_j^k will cause $\bar{v}_{Cj}^k$ to deviate from V_{Cj}^{k*} significantly. To suppress the significant fluctuation/deviation, one common method is to simultaneously inject circulating currents and a common-mode voltage to cancel out the low-frequency components in p_j^k. Compared to the methods based on only injecting circulating currents, the method will neither cause large fluctuations under $f_{\rm out} = f_{\rm in}/3$ condition nor require reactive power adjustment of the input or output side.

In a well-controlled system, the input side line-to-neutral voltages and common-mode voltage can be assumed to be equal to their references, i.e., $v_{{\rm out},j}^*$ and $v_{\rm com}^*$. Thus, the cluster power can be expressed as:

$$p_j^k = \left(\frac{1}{3}i_{\rm in}^k + \frac{1}{3}i_{{\rm out},j} + i_{{\rm cir},j}^k\right)\left(v_{\rm in}^k - v_{{\rm out},j}^* - v_{\rm com}^*\right), \tag{5.56}$$

where $i_{{\rm cir},j}^k$ denotes the circulating current. Since the low-frequency components in the cluster power are produced by the terms $\frac{1}{3}v_{\rm in}^k i_{{\rm out},j} - \frac{1}{3}v_{{\rm out},j}^* i_{\rm in}^k$, the cluster power component that needs to be removed can be set as

$$\begin{aligned} &p_{{\rm rmv},j}^k = \tfrac{1}{3}v_{\rm in}^k i_{{\rm out},j} - \tfrac{1}{3}v_{{\rm out},j}^* i_{\rm in}^k \\ &= \tfrac{1}{6}\hat{V}_{\rm in}\hat{I}_{\rm out}\cos\left(\left(\omega_{\rm in} - \omega_{\rm out}\right)t + \varphi_{\rm d1}\right) - \tfrac{1}{6}\hat{V}_{\rm in}\hat{I}_{\rm out}\cos\left(\left(\omega_{\rm in} + \omega_{\rm out}\right)t + \varphi_{\rm c}\right) \\ &+\tfrac{1}{6}\hat{V}_{\rm out}\hat{I}_{\rm in}\cos\left(\left(\omega_{\rm in} - \omega_{\rm out}\right)t + \varphi_{\rm d2}\right) - \tfrac{1}{6}\hat{V}_{\rm out}\hat{I}_{\rm in}\cos\left(\left(\omega_{\rm in} + \omega_{\rm out}\right)t + \varphi_{\rm c}\right), \end{aligned} \tag{5.57}$$

where $\hat{V}_{\rm in}$, $\hat{I}_{\rm in}$, $\hat{V}_{\rm out}$, and $\hat{I}_{\rm out}$ are the peak values of $v_{\rm in}$, $i_{\rm in}$, $v_{{\rm out},j}$, and $i_{{\rm out},j}$ respectively, $\omega_{\rm in}$ and $\omega_{\rm out}$ are fundamental frequencies of input and output sides, $\varphi_{\rm d1}$, $\varphi_{\rm d2}$, and $\varphi_{\rm c}$ are phase angles of the components. Calculation of $p_{{\rm rmv},j}^k$ in (5.57) is independent of the phase angles of both input- and output-side voltages and currents, which are obtained from phase

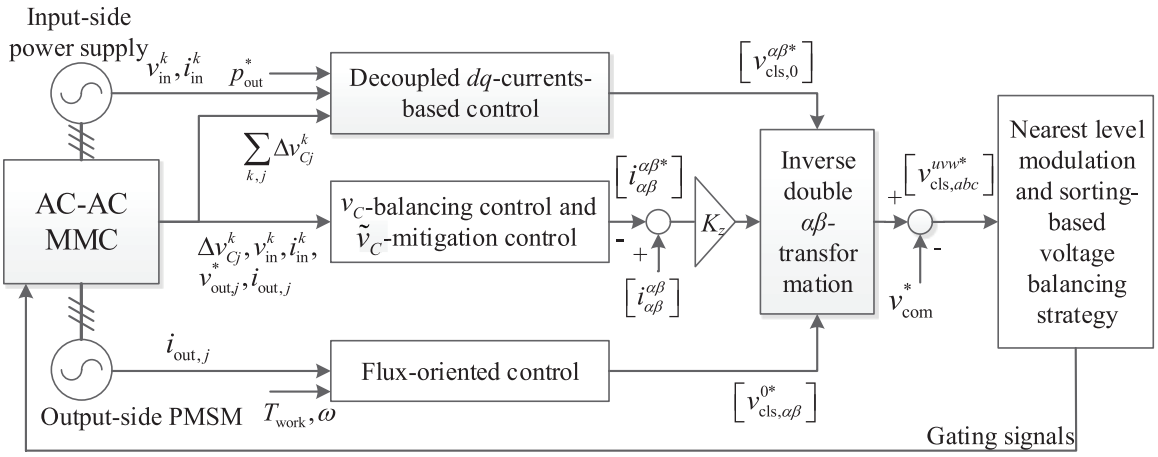

Figure 5.12: Block diagram of the overall control of the AC-AC MMC.

lock loop or rotor position sensor. In [81], the component that needs to be removed is

$$p^k_{\mathrm{rmv},j} = \frac{1}{6}\hat{V}_{\mathrm{in}}\hat{I}_{\mathrm{out}}\cos\left(\left(\omega_{\mathrm{in}}-\omega_{\mathrm{out}}\right)t+\varphi_{\mathrm{d1}}\right)+\frac{1}{6}\hat{V}_{\mathrm{out}}\hat{I}_{\mathrm{in}}\cos\left(\left(\omega_{\mathrm{in}}-\omega_{\mathrm{out}}\right)t+\varphi_{\mathrm{d2}}\right), \quad (5.58)$$

which depends on the frequencies and phase angles of both input- and output-side voltages and currents. Therefore, compared to the method that bases on (5.58) in [81], removing components that (5.57) contains is simpler. However, (5.57) contains $(\omega_{\mathrm{in}}+\omega_{\mathrm{out}})$-frequency components, which requires injecting larger circulating currents. The larger injected circulating currents lead to higher power losses and impose a higher voltage output capability on the clusters.

Sinusoidal-wave common-mode voltage

v^*_{com} can be set as a third-order harmonic [81], i.e.,

$$v^*_{\mathrm{com}} = \frac{\hat{V}_{\mathrm{in}}}{6}\sin\left(2\pi f_{\mathrm{com}}t\right), \quad (5.59)$$

where f_{com} is three times of the input side fundamental frequency.

Since the sinusoidal v^*_{com} has zero-crossing points, the commanded circulating current components to mitigate the SM capacitor voltage fluctuations, i.e., $i^{k*}_{\mathrm{cir,fm},j}$ cannot be set as

$p^k_{\mathrm{rmv},j}/v^*_{\mathrm{com}}$ directly. A solution to the singularity is to keep the average value of $v^*_{\mathrm{com}} i^{k*}_{\mathrm{cir,fm},j}$ equal to $p^k_{\mathrm{rmv},j}$ over the period of common-mode voltage, i.e.,

$$i^{k*}_{\mathrm{cir,fm},j} = \frac{12 p^k_{\mathrm{rmv},j}}{\hat{V}_{\mathrm{in}}} \sin\left(2\pi f_{\mathrm{com}} t\right). \tag{5.60}$$

The proposed method introduces a new form of circulating currents to overcome the singularity problem:

$$i^{k*}_{\mathrm{cir,fm},j} = \frac{v^*_{\mathrm{com}}}{\left(v^*_{\mathrm{com}}\right)^2 + \sigma} p^k_{\mathrm{rmv},j}, \tag{5.61}$$

where σ is an empirical ancillary factor. Based on (5.61), when $|v^*_{\mathrm{com}}| \gg \sqrt{\sigma}$, $i^{k*}_{\mathrm{cir,fm},j}$ approximately equals to $p^k_{\mathrm{rmv},j}/v^*_{\mathrm{com}}$. When $|v^*_{\mathrm{com}}| \ll \sqrt{\sigma}$, $i^{k*}_{\mathrm{cir,fm},j}$ approximately equals to zero. Besides, the transition between the two typical conditions is smooth.

Square-wave common-mode voltage

v^*_{com} can be set as a square wave with a third-order harmonic frequency, i.e.,

$$v^*_{\mathrm{com}} = \begin{cases} \frac{\hat{V}_{\mathrm{in}}}{6} & \left(0 < t < \frac{1}{2f_{\mathrm{com}}}\right) \\ -\frac{\hat{V}_{\mathrm{in}}}{6} & \left(\frac{1}{2f_{\mathrm{com}}} < t < \frac{1}{f_{\mathrm{com}}}\right) \end{cases}. \tag{5.62}$$

Since magnitude of the fundamental component is $\sqrt{2}\hat{V}_{\mathrm{in}}/6$, the square-wave-based method can reduce the peak value of the circulating current to $1/\sqrt{2}$ of the value based on (5.59) and (5.60). Therefore, (5.60) needs to be modified to be

$$i^{k*}_{\mathrm{cir,fm},j} = \frac{6\sqrt{2} p^k_{\mathrm{rmv},j}}{\hat{V}_{\mathrm{in}}} \sin\left(2\pi f_{\mathrm{com}} t\right). \tag{5.63}$$

Another advantage of the square-wave-based method is that the v^*_{com} is never zero. Therefore, the injected circulating current reference can be

$$i^{k*}_{\mathrm{cir,fm,j}} = \frac{p^k_{\mathrm{rmv},j}}{v^*_{\mathrm{com}}}. \tag{5.64}$$

In summary, the $\tilde{v}_C$-mitigation methods proposed in the section are listed and numbered in Table 5.3.

Table 5.3: Number of $\tilde{v}_C$-mitigation methods

No.	$p^k_{\mathrm{rmv},j}$	v^*_{com}	$i^{k*}_{\mathrm{cir,fm,j}}$	No.	$p^k_{\mathrm{rmv},j}$	v^*_{com}	$i^{k*}_{\mathrm{cir,fm,j}}$
1st	(5.57)	(5.59)	(5.60)	2nd	(5.57)	(5.59)	(5.61)
3rd	(5.57)	(5.62)	(5.63)	4th	(5.57)	(5.62)	(5.64)
5th	(5.58)	(5.59)	(5.61)	6th	(5.58)	(5.62)	(5.63)
7th	(5.58)	(5.62)	(5.64)				

5.3.2 Simulation results

In this section, simulation results conducted in the PSCAD/EMTDC software environment are presented to verify the effectiveness of the proposed methods. Fig. 5.7 presents the study system. The parameters of the study system are listed in Table 5.4. The permanent magnetic synchronous machine (PMSM) is loaded at the rated torque and the operation frequency, i.e., f_{out}, is 50 Hz, which equals to f_{in}. Flux-oriented control is applied to the PMSM. The overall control system is provided in Fig. 5.12. On the input side, decoupled dq-currents control is utilized, where the setpoint of the reactive power is zero VAr.

Table 5.4: Parameters of the study system

Quantity	Value
Nominal power of AC-AC MMC S_{b}	15 kVA
Ac system nominal voltage $V_{\mathrm{in,ll,rms}}$	400 V
Nominal frequency of AC system f_{in}	50 Hz
Series-connected inductance l	5 mH
Resistance of series-connected inductor r	1 mΩ
Number of SMs in each cluster N	4
Submodule capacitor C	1700 μF
Rated power of PMSM $P_{\mathrm{out,r}}$	15 kW
Unsaturated reactance in q-axis	20 mH
Unsaturated reactance in d-axis	20 mH
Rated voltage of PMSM $V_{\mathrm{out,ll,rms}}$	400 V
Rated frequency of PMSM f_{out}	75 Hz
Stator winding resistance	0.46 Ω
Stator leakage reactance	4 mH

Fig. 5.13 shows the converter waveforms under the proposed fault-tolerant strategy when the first $\tilde{v}_C$-mitigation method is employed. At $t = 2.5\ s$, one SM in the cluster connecting the input-side phase u and output-side phase a fails. Figures 5.13(d) and (e) show that, prior to the activation of the fault-tolerant strategy, output-side voltages and currents are significantly distorted. Subsequent to bypassing the faulty SM at $t = 2.55\ s$, the proposed fault-tolerant strategy is applied. Subsequently, based on (5.49), $\bar{v}_{Ca}^{u}$ is increased to 266.7 V while other $\bar{v}_{Cj}^{k}$ undergo negligible changes and are recovered to their normal value, as shown in Fig. 5.13(a). Figure 5.13(b) illustrates that, subsequent to activation of the fault-tolerant strategy, the cluster currents remain within the normal range. Meanwhile, the output-side voltages and currents recover to the normal waveforms as illustrated in Figs. 5.13(d) and (e), confirming that the proposed fault-tolerant strategy and first $\tilde{v}_C$-mitigation method are both effective. Figures 5.14 to 5.19 present the same waveforms under the other $\tilde{v}_C$-mitigation methods: $\bar{v}_{Cj}^{k}$ of the faulty and normal clusters are regulated as expected; cluster currents are limited in the normal range under the fault-tolerant strategy, and the output-side voltages and currents recover from the distortion, confirming the effectiveness of the proposed fault-tolerant strategy and all of the $\tilde{v}_C$-mitigation methods.

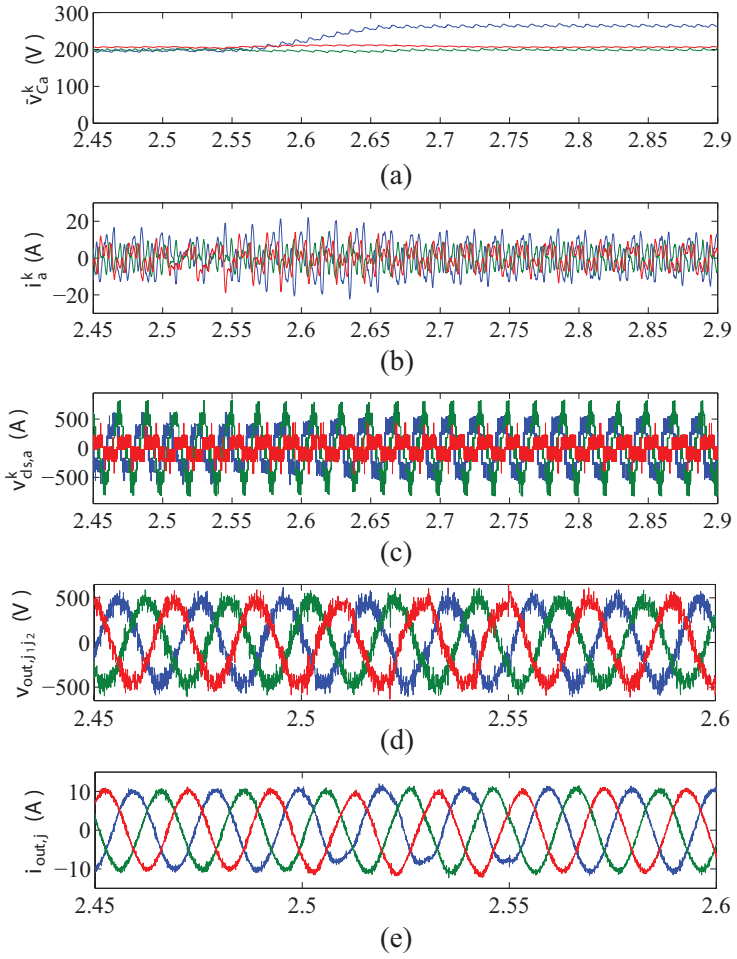

Figure 5.13: Converter waveforms under the proposed fault-tolerant strategy and the first capacitor voltage mitigation method: (a) v^k_{Ca} ($k = u, v, w$), (b) i^k_a ($k = u, v, w$), (c) $v^k_{\text{cls,a}}$ ($k = u, v, w$), (d) zoomed v_{out,j_1j_2} ($j_1j_2 = ab, bc, ca$), and (e) zoomed $i_{\text{out},j}$ ($j = a, b, c$).

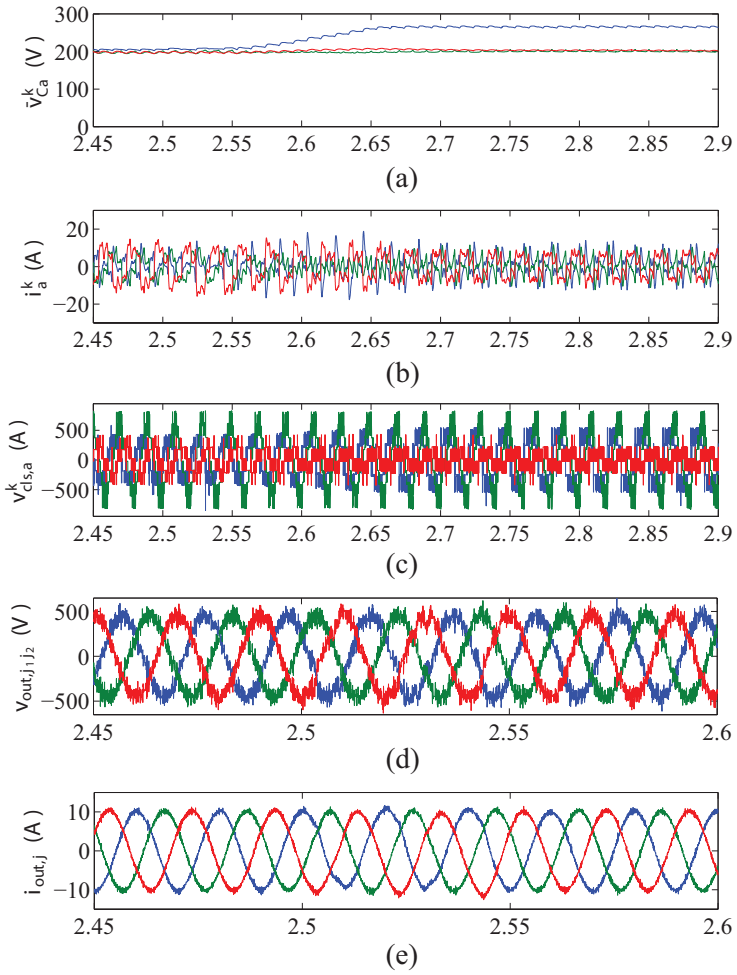

Figure 5.14: Converter waveforms under the proposed fault-tolerant strategy and the second capacitor voltage mitigation method: (a) v_{Ca}^k ($k = u, v, w$), (b) i_a^k ($k = u, v, w$), (c) $v_{\text{cls,a}}^k$ ($k = u, v, w$), (d) zoomed v_{out,j_1j_2} ($j_1j_2 = ab, bc, ca$), and (e) zoomed $i_{\text{out},j}$ ($j = a, b, c$).

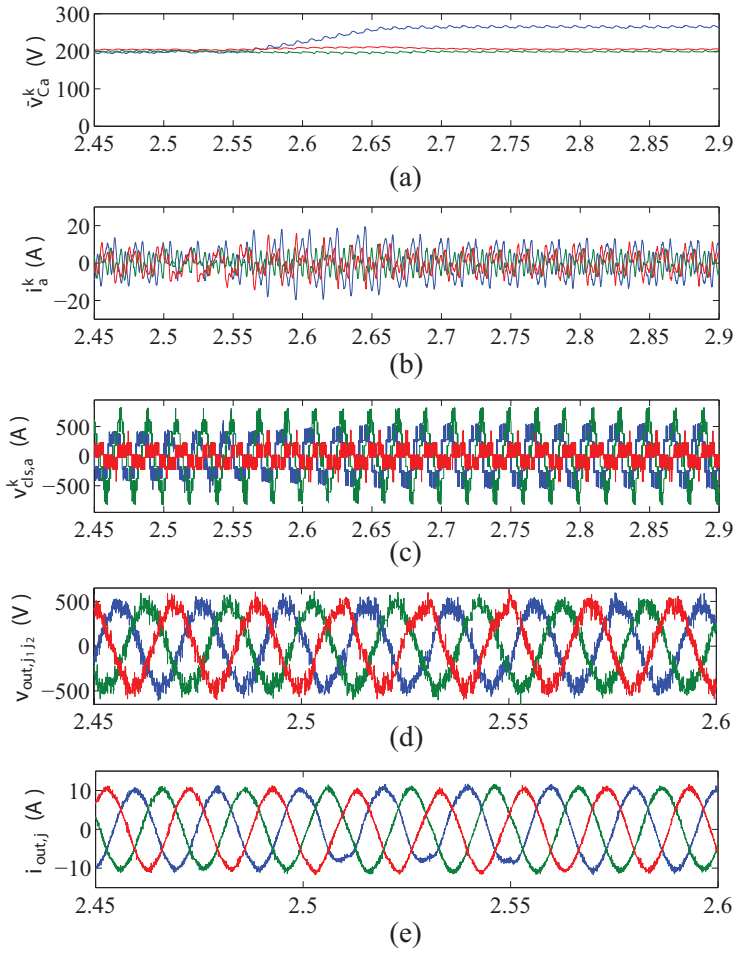

Figure 5.15: Converter waveforms under the proposed fault-tolerant strategy and the third capacitor voltage mitigation method: (a) v_{Ca}^k ($k = u, v, w$), (b) i_a^k ($k = u, v, w$), (c) $v_{\text{cls,a}}^k$ ($k = u, v, w$), (d) zoomed v_{out,j_1j_2} ($j_1j_2 = ab, bc, ca$), and (e) zoomed $i_{\text{out},j}$ ($j = a, b, c$).

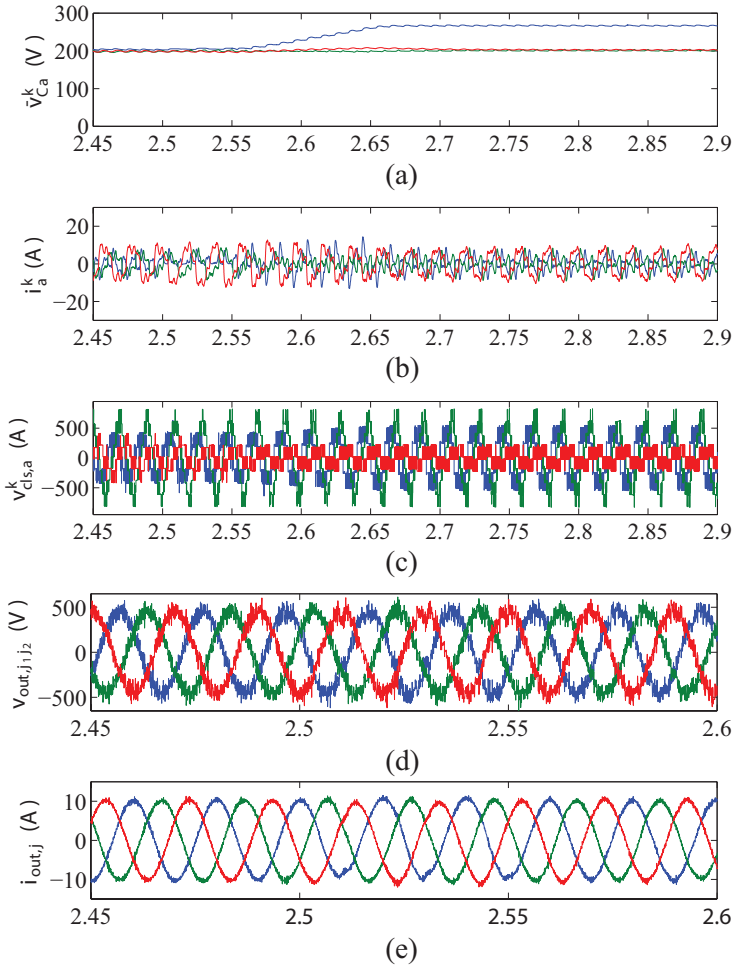

Figure 5.16: Converter waveforms under the proposed fault-tolerant strategy and the fourth capacitor voltage mitigation method: (a) v^k_{Ca} ($k = u, v, w$), (b) i^k_a ($k = u, v, w$), (c) $v^k_{\mathrm{cls,a}}$ ($k = u, v, w$), (d) zoomed v_{out,j_1j_2} ($j_1j_2 = ab, bc, ca$), and (e) zoomed $i_{\mathrm{out},j}$ ($j = a, b, c$).

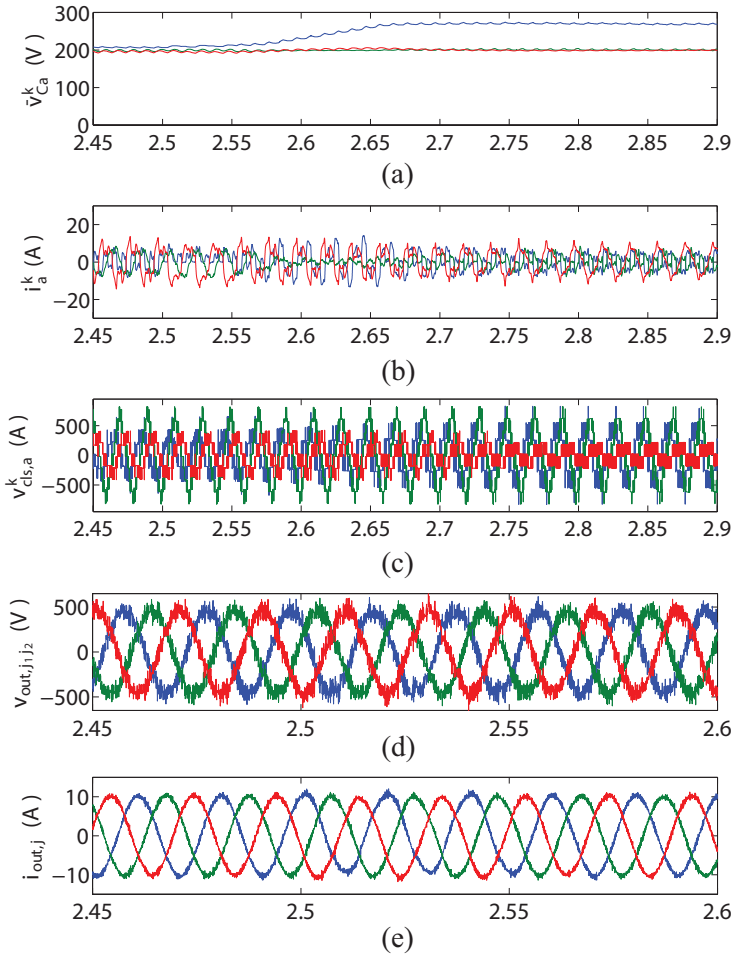

Figure 5.17: Converter waveforms under the proposed fault-tolerant strategy and the fifth capacitor voltage mitigation method: (a) v^k_{Ca} ($k = u, v, w$), (b) i^k_a ($k = u, v, w$), (c) $v^k_{\text{cls,a}}$ ($k = u, v, w$), (d) zoomed v_{out,j_1j_2} ($j_1j_2 = ab, bc, ca$), and (e) zoomed $i_{\text{out},j}$ ($j = a, b, c$).

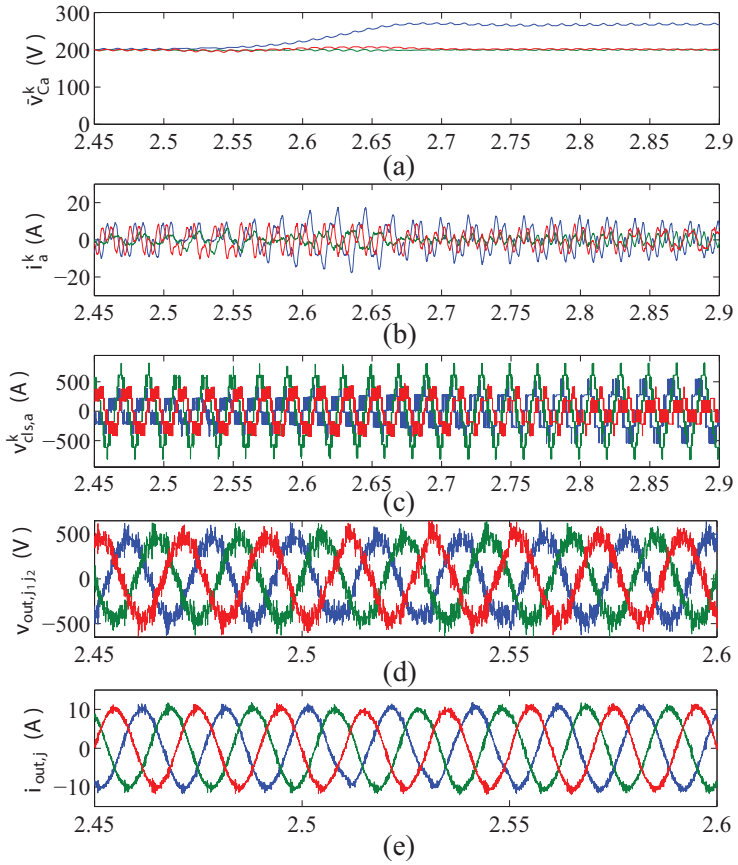

Figure 5.18: Converter waveforms under the proposed fault-tolerant strategy and the sixth capacitor voltage mitigation method: (a) v^k_{Ca} ($k = u, v, w$), (b) i^k_a ($k = u, v, w$), (c) $v^k_{\mathrm{cls,a}}$ ($k = u, v, w$), (d) zoomed v_{out,j_1j_2} ($j_1j_2 = ab, bc, ca$), and (e) zoomed $i_{\mathrm{out},j}$ ($j = a, b, c$).

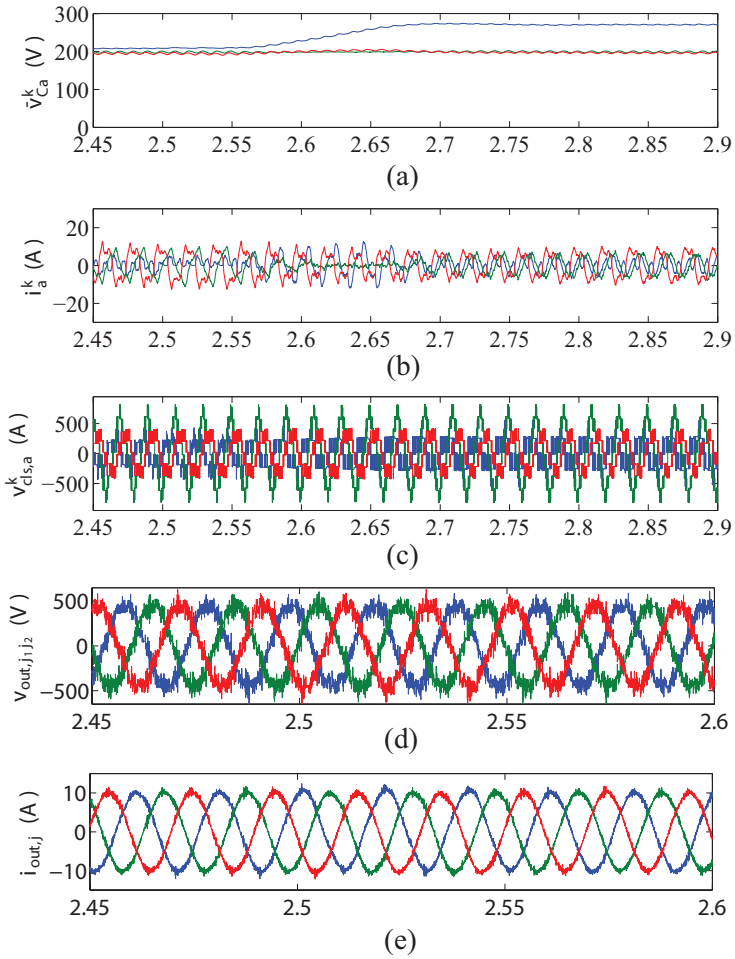

Figure 5.19: Converter waveforms under the proposed fault-tolerant strategy and the seventh capacitor voltage mitigation method: (a) v^k_{Ca} ($k = u, v, w$), (b) i^k_a ($k = u, v, w$), (c) $v^k_{\text{cls,a}}$ ($k = u, v, w$), (d) zoomed v_{out,j_1j_2} ($j_1j_2 = ab, bc, ca$), and (e) zoomed $i_{\text{out},j}$ ($j = a, b, c$).

CHAPTER 6

THE MMC SETUP AND THE EXPERIMENTAL RESULTS

In this chapter, the hardware design and OPAL-RT-based control system for the MMC setup are presented. Experimental results are provided to:

- verify the proposed SMC-based control method for the DC-AC MMC in Chapter 2,
- verify the proposed thermal loading optimization method for the DC-AC MMC in Chapter 3.

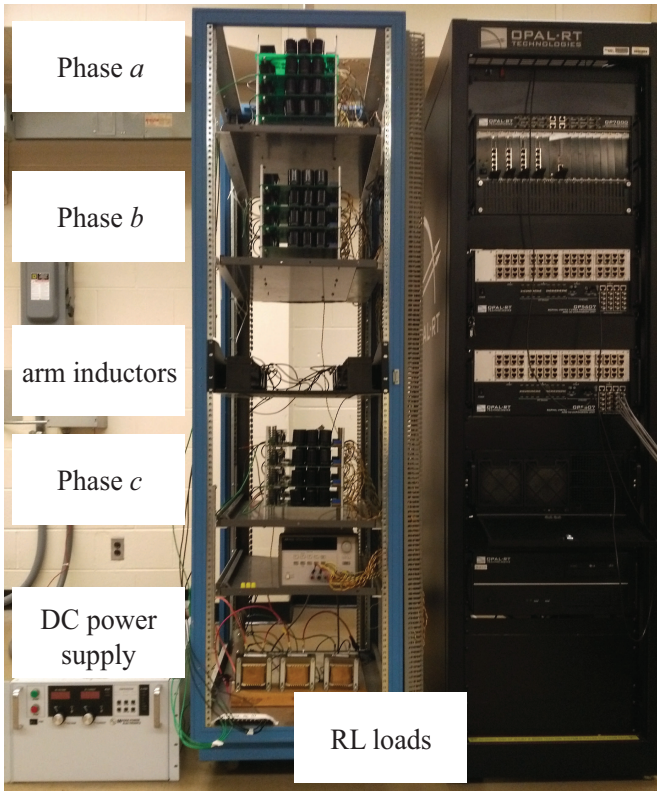

Figure 6.1: Experiment setup of the three-phase MMC prototype.

The parameters of the prototype, shown in Fig. 6.1, are listed in Table 6.1. In the experimental prototype, the DC-side of the three-phase MMC is supplied by a programmable

DC power supply while its AC side is connected to a three-phase RL load. The semiconductor devices are IXYS FII 30-06D. The control method is implemented in the RT-Lab and OPAL-RT rapid control prototyping tool with an integrated FPGA.

Table 6.1: Parameters of the experimental setup

Quantity	Value	Quantity	Value
DC source voltage V_{DC}	100 V	Nominal frequency	60 Hz
Number of SMs per arm N	4	Buffer inductance l	5 mH
Submodule capacitor C	1410 μF	Load L_{load}	4.5 mH
Switching frequency f_{sw}	480 Hz	Load R_{load}	6.7 Ω

6.1 SM Design for the DC-AC MMC Setup

As presented in the previous chapters, the common DC-AC MMC consists of six identical arms, and each arm consists of a series of SMs and a series-connected inductor. The hardware design focuses on the PCB of the SMs and current sensors. The printed circuit board (PCB) of the SM contains three function areas: dead-time generation area, gate driver area, and main power area. In the dead-time generation area, RC circuit and inverted op-amp are applied to generate dead-time. In the gate driver area, reserved positions for the gate resistors, gate-emitter capacitors, and protection Zener diodes are provided to adjust switching speed and protect the devices. In the main power area, the capacitors are connected in parallel with two large copper sheets and the capacitor bank is as close as possible to the devices, thereby minimizing the parasitic inductance in the main power loop.

6.2 OPAL-RT-based Control System

The control system is implemented by using OPAL-RT rapid control prototyping system. The OPAL-RT system consists of a real-time simulator, two Vertex 7 FPGA, and several I/O units. A host computer is interfaced with the simulator to monitor real-time signals and adjust controller parameters. The schematic of the control system is illustrated in Fig. 6.2,

where the control system is divided into four parts: pretreatment part, capacitor voltage regulation part (outer control loop), inductor current regulation part (inner control loop), and modulation part. The four parts are distributed into two subsystems. One subsystem includes the pretreatment, capacitor voltage regulation, and inductor current regulation parts, while the other subsystem is the phase-shifted (PS) modulation. The interface between the real-time controller and the MMC setup is made through the FPGA and I/O units. The measured voltage and current signals are transmitted to the CPU cores through the Analog In channels, and the gating signals are sent to the MMC setup through Digital Out channels.

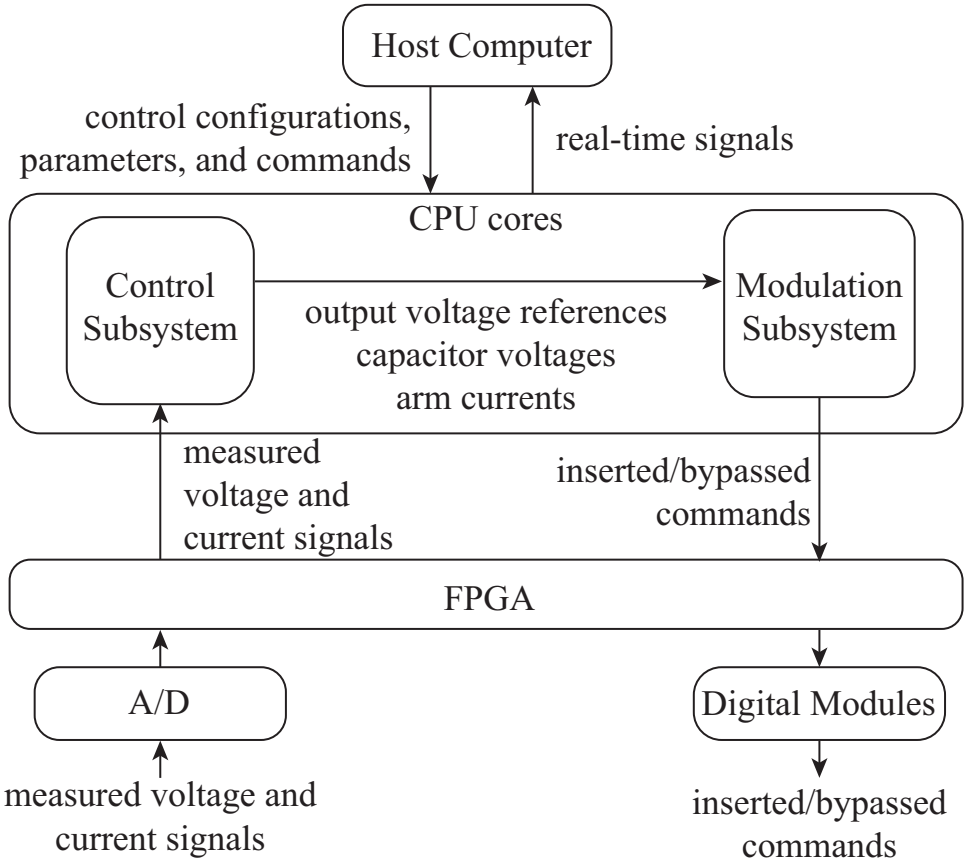

Figure 6.2: Control architecture for the MMC setup.

6.3 Experimental Result of the Proposed SMC-based Control Method

To verify the proposed SMC-based control method for the MMC in Chapter 2, the phase-shifted modulation [109] is applied in the experiment, where the $f_{\rm sw}$ is set to be 480 Hz. Fig. 6.3 presents the experimental waveforms under the proposed SMC-based method, where $i^{q,\rm ref}$ steps up from 1.5 A to 4 A at $t = 100$ ms while $i^{d,\rm ref}$ remains to be zero. Figures 6.3(a), (b), and (c) present the three-phase line currents, SM capacitor voltages of phase a, and arm currents of phase a are well controlled during the transients. Figure 6.3(d) illustrates that i^q and i^d closely track their references under the SMC-based method. Figure 6.3(e) shows gating signals of lower switches of the four SMs in the lower arm of phase a. The pulses of two adjacent SMs has 90° phase shift and frequency of the pulses are kept to be 480 Hz. Based on Fig. 6.3(f), the rise time of i^q is about 1.7 ms (from 1.75 A, i.e., 10% the $\Delta I^{q,\rm ref}$, to 3.75 A, i.e., 90% the $\Delta I^{q,\rm ref}$). Fig. 6.3(g) illustrates the zoomed-in gating signals when i^q rises. Fig. 6.4 presents the corresponding experimental waveforms under the conventional PI-based control with the same scenario, where $i^{q,\rm ref}$ steps up from 1.5 A to 4 A. As shown in Fig. 6.4(f), under the PI-based control, the rise time for i^q is 2.6 ms, which is longer than that under the SMC-based method by 53%. The SMC-based method shortens the rising time by 35%, which verifies that the proposed SMC-based method can provide higher speed of dynamic response.

6.4 Experimental Result of the Proposed Thermal Loading Control Strategy

In this section, performance of the thermal loading optimization method, which is proposed in Chapter 3, is presented. The IXYS FII 30-06D package include the two IGBTs and two anti-parallel diodes. Therefore, the temperatures of semiconductor devices cannot be measured separately and only the objective of minimizing the total semiconductor power loss is carried out. The optimized and conventional operating conditions are presented in Table 6.2. The parameters of the prototype are listed in Table 6.1.

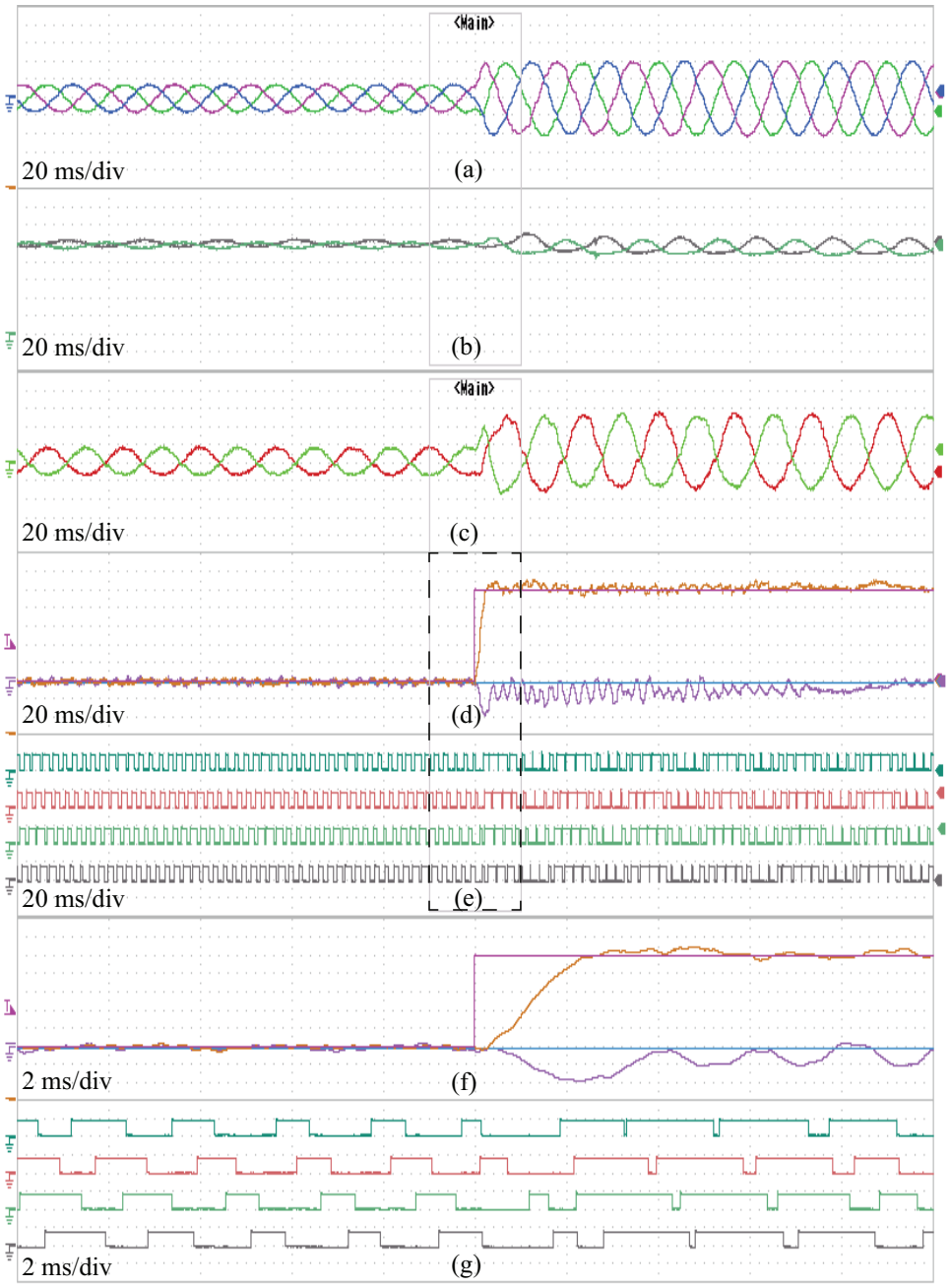

Figure 6.3: Experimental MMC waveforms under the proposed SMC-based method: (a) three-phase line currents, (b) average SM capacitor voltages of phase a, (c) arm currents of phase a, (d) q- and d-axis components of the line currents and their references, (e) gating signals of lower switches of the four SMs in the lower arm of phase a, (f) zoomed-in q- and d-axis components of the line currents and their references during the transient process, and (g) zoomed-in gating signals of lower switches of the four SMs in the lower arm of phase a during the transient process.

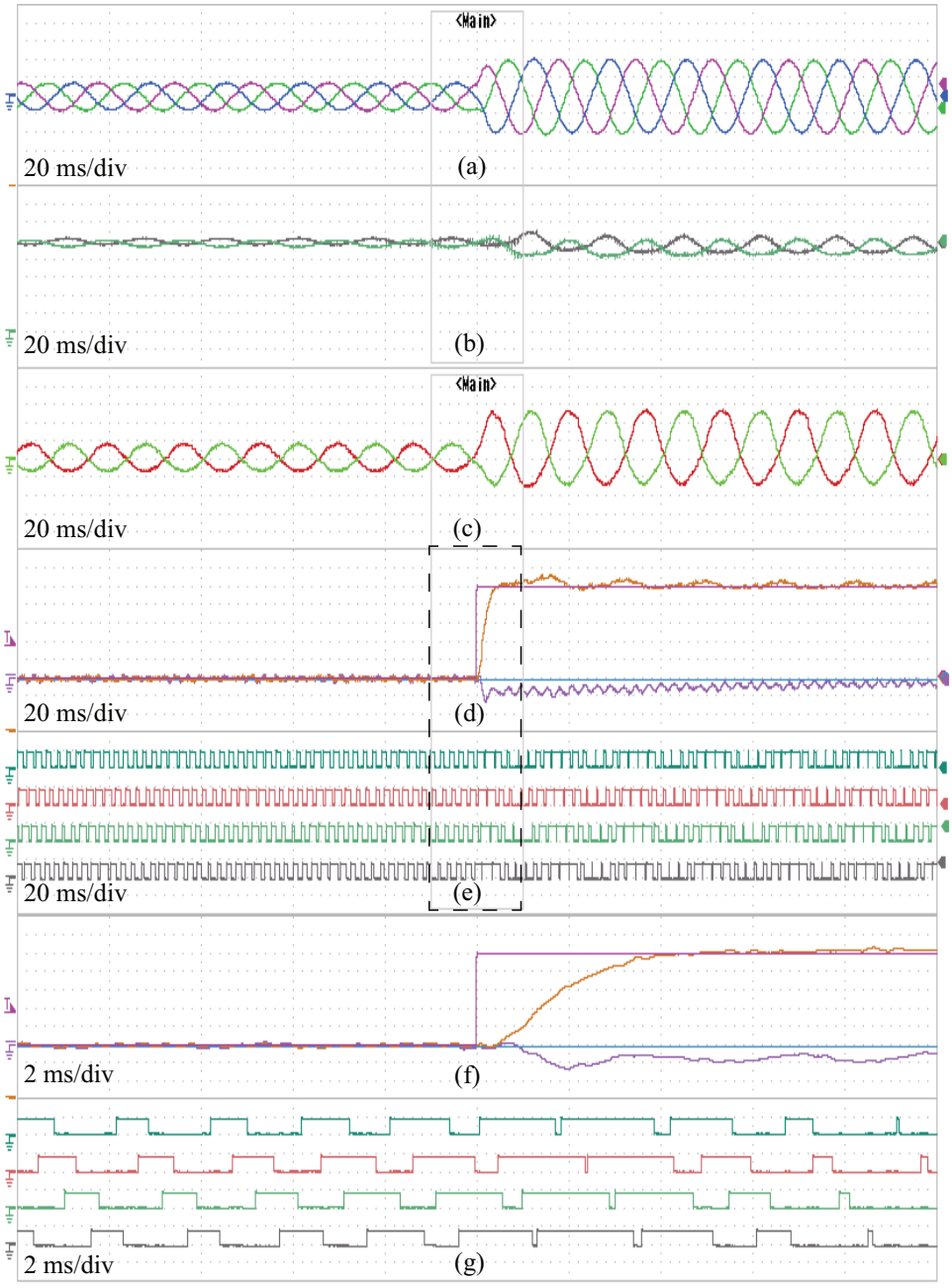

Figure 6.4: Experimental MMC waveforms under the conventional PI-based control: (a) three-phase line currents, (b) average SM capacitor voltages of phase a, (c) arm currents of phase a, (d) q- and d-axis components of the line currents and their references, (e) gating signals of lower switches of the four SMs in the lower arm of phase a, (f) zoomed-in q- and d-axis components of the line currents and their references during the transient process, and (g) zoomed-in gating signals of lower switches of the four SMs in the lower arm of phase a during the transient process.

Table 6.2: Experimental operating conditions

Cond.	$\hat{I}_2$	ϕ_{I2}	$\hat{V}_{\text{com}}^{\text{out}}$	ϕ_{Vocm}	V_C^{ref}
Conv.	0	0	0	0	30 V
Opt.	0.45 A	106°	5.4 V	8°	23.6 V

Figure 6.5 presents the waveforms corresponding to the optimized and conventional operating conditions. Figures 6.5(a), (b), (e), and (f) illustrate the arm currents and capacitor voltages. Figures. 6.5(c), (d), (g), and (h) show the line-to-line voltage and line currents of the MMC. Figure 6.6 shows the heat sink temperature of the semiconductor devices in steady state, confirming that the heat sink temperature is reduced by 2.4 $^{\circ}C$ when operating under the optimal operating condition.

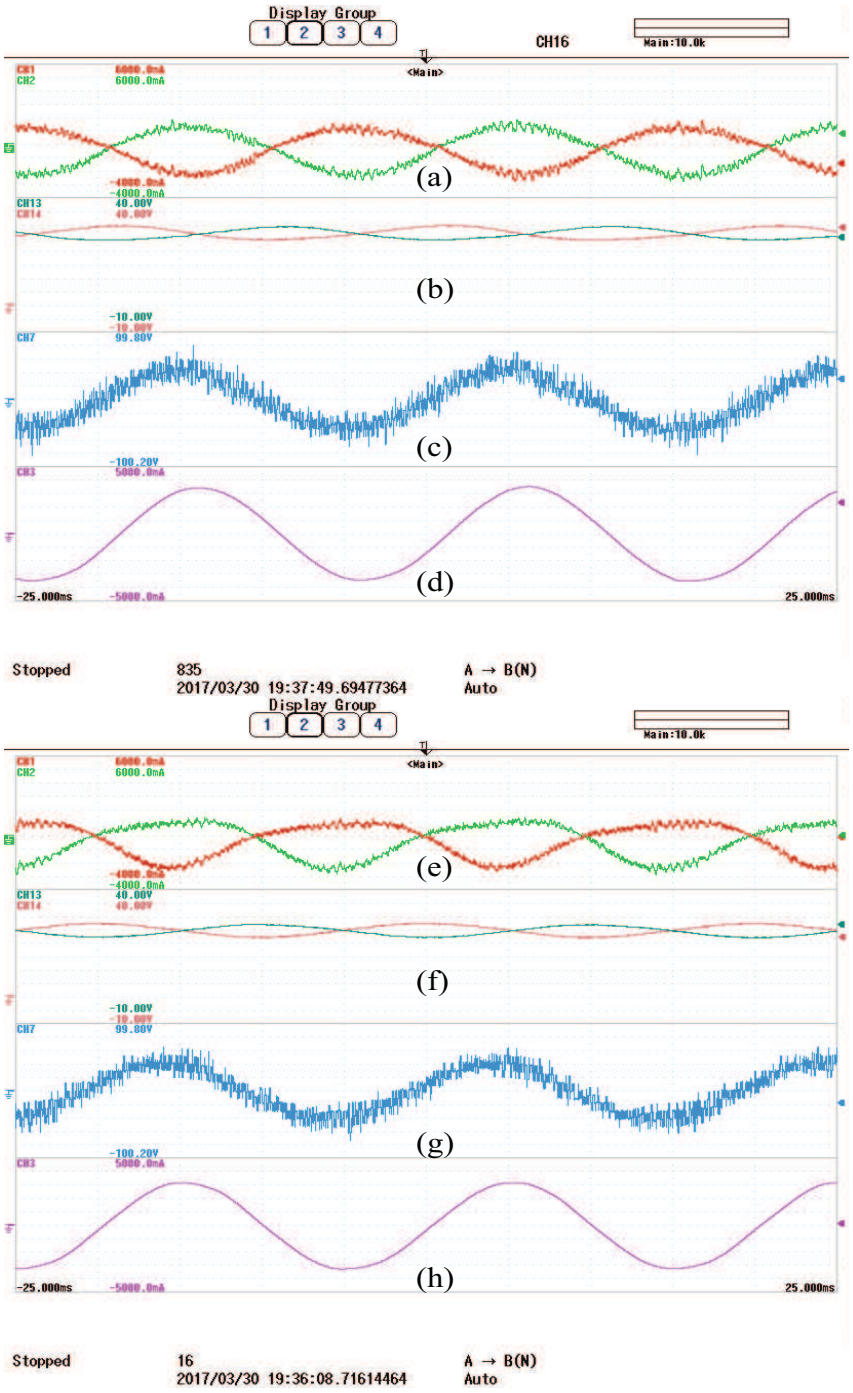

Figure 6.5: Experimental MMC waveforms under different operating conditions: (a)-(d) $i^{p,a}$ and $-i^{n,a}$, capacitor voltages of first SM of the upper and lower arms of phase a, line-to-line voltage $v_{\mathrm{t},ab}$, and line current of phase a under the conventional operating condition, (e)-(h) $i^{p,a}$ and $-i^{n,a}$, capacitor voltages of first SM of the upper and lower arms of phase a, line-to-line voltage $v_{\mathrm{t},ab}$, and line current of phase a under the optimized operating condition.

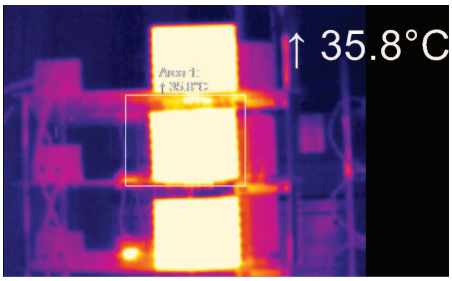

(a)

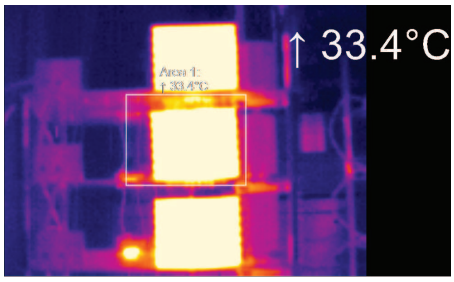

(b)

Figure 6.6: SM heat sink temperature under: (a) the conventional condition, and (b) the optimized condition.

CHAPTER 7
HYBRID MMC-BASED CONFIGURATIONS FOR LOW-FREQUENCY OPERATION

In this chapter, a hybrid MMC-based topology along with its supporting control strategy are proposed to suppress the large SM capacitor voltage fluctuations without injecting any load-side common-mode voltage. The main concept is to add high-frequency AC components into the DC-link voltage, which interact with high-frequency output currents of each phase to cancel out the unbalanced power between the upper and lower arms. To prevent the added high-frequency currents from flowing into the load, an auxiliary MMC converter is required to be connected in parallel with the load. The proposed method is capable of eliminating the injected voltage between the three-phase load neutral point and ground, which is beneficial to the load and does not depend on any special $V - I$ characteristic of the load.

7.1 Topology and Operation Principle

Figure 7.1(a) illustrates the circuit of the proposed converters based on a back-to-back MMC, which is composed of a rectifier, an inverter, and an auxiliary converter. Topologies of the rectifier and inverter are the same as the half-bridge (HB) SM-based DC-AC MMC, while the auxiliary converter is a full-bridge (FB) SM-based single-star converter. Fig. 7.1(b) illustrates the circuit diagram of another proposed converter, which is based on a diode or thyristor-based rectifier. In Fig. 7.1(b), the inverter and the auxiliary converter are the same as those in Fig. 7.1(a), while a pair of FB SM-based series-connected converter is inserted in the link.

Common- and differential-mode components of the arm currents, i.e., $i^{x,j}$ ($x = p, n;\ j = a, b, c$), the average SM capacitor voltages, i.e., $v_C^{x,j}$, and the voltages across arms, i.e., $v^{x,j}$

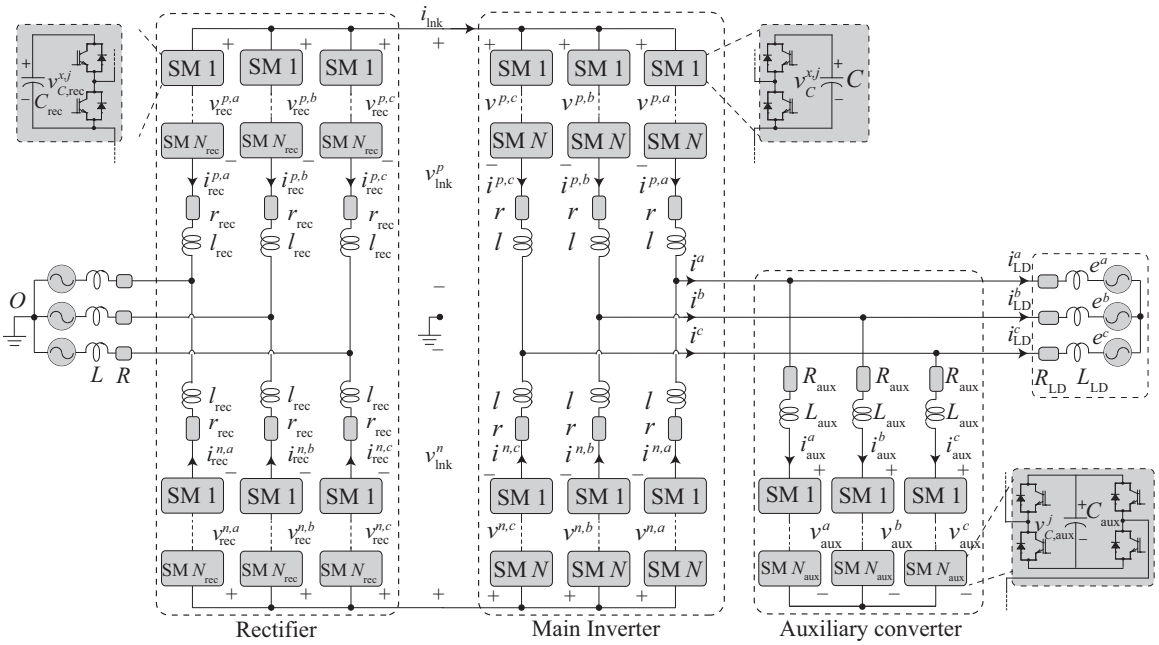

(a)

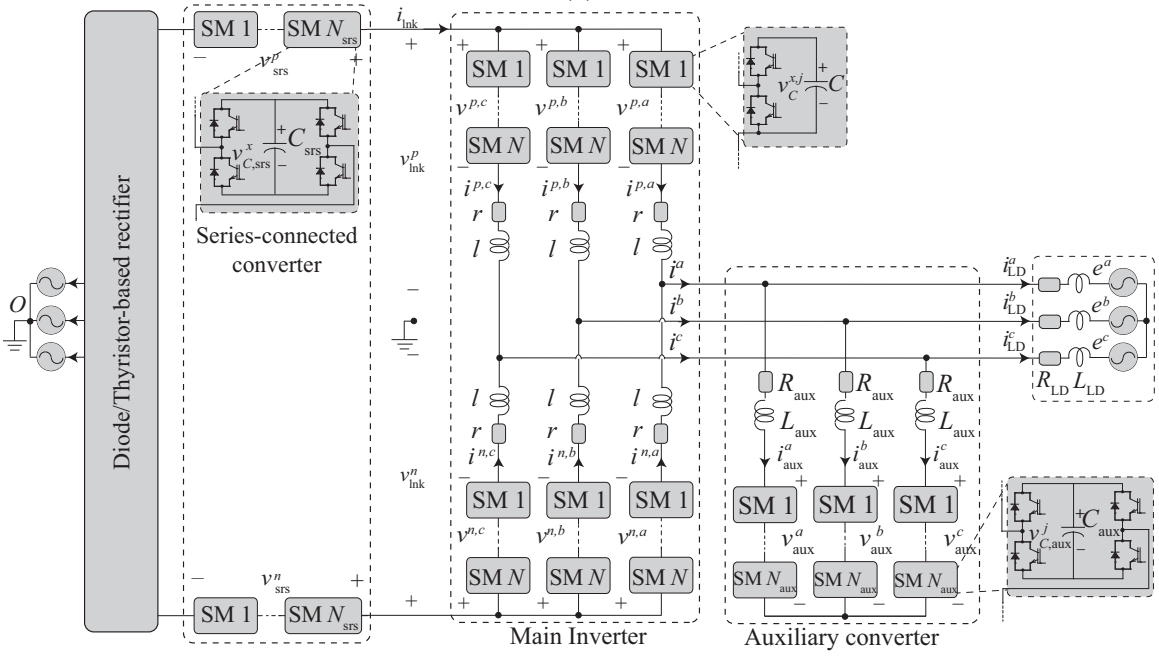

(b)

Figure 7.1: Circuit diagram of the MMC based on the proposed high-frequency AC voltage-based method: (a) MMC-based rectifier, (b) diode/thyristor-based rectifier

are:

$$z^j_{\text{com}} = \tfrac{1}{2}\left(z^{p,j} + z^{n,j}\right),\ z^j_{\text{dif}} = \tfrac{1}{2}\left(z^{p,j} - z^{n,j}\right), \tag{7.1}$$

where $z^{x,j}$ denotes $i^{x,j}$, $v_C^{x,j}$, and $v^{x,j}$, z^j_{com} and z^j_{dif} denote the corresponding common- and differential-mode components. In the conventional strategy for low-frequency operation of the MMC, higher-frequency common-mode components of the voltages across the arms and differential-mode currents are injected, which transfer power between the upper and lower arms of each phase-leg to guarantee the energy of the upper and lower arms stay balanced [21]. However, the zero-sequence voltage increases the insulation requirements of the load. The limited insulation level of the load limits the magnitude of the zero-sequence voltage, which requires large circulating currents and, therefore, increases the power losses and thermal load of each device.

In the proposed converters, the AC differential-mode voltage and a common-mode current are injected to each phase-leg to transfer energy between the upper and lower arms and to suppress the large energy fluctuation. If the rectifier is an MMC, as illustrated in Fig. 7.1(a), the AC voltage components can be injected into the DC-link by adjusting the number of inserted SMs in both rectifier and inverter. For the converter in Fig. 7.1(b), the AC voltage components can be injected by inserting SMs of the series-connected converter and inverter. Besides, the auxiliary converter is added to absorb the injected common-mode currents. In this way, the injected common-mode currents do not interfere with the load currents.

7.2 Dynamics of the System and Current Control Strategy

Dynamics of variables in the rectifier MMC, as illustrated in Fig. 7.1(a), are the same as those in the conventional DC-AC MMC. Based on KVL, dynamics of i^j_{aux} and i^j_{LD} is:

$$v_{0,\text{LD}} + e^j + R_{\text{LD}} i^j_{\text{LD}} + L_{\text{LD}} \tfrac{\mathrm{d}i^j_{\text{LD}}}{\mathrm{d}t} = v_{0,\text{aux}} + v^j_{\text{aux}} + R_{\text{aux}} i^j_{\text{aux}} + L_{\text{aux}} \tfrac{\mathrm{d}i^j_{\text{aux}}}{\mathrm{d}t}, \tag{7.2a}$$

$$v_{0,\text{LD}} + e^j + R_{\text{LD}} i^j_{\text{LD}} + L_{\text{LD}} \tfrac{\mathrm{d}i^j_{\text{LD}}}{\mathrm{d}t} = -v^j_{\text{com}} - \tfrac{1}{2} r i^j - \tfrac{1}{2} l \tfrac{\mathrm{d}i^j}{\mathrm{d}t}, \tag{7.2b}$$

where $v_{0,\text{LD}}$ is the load-side zero-sequence voltage, e^j is the electro-motive of the load, i^j_{LD} is the load current of phase j, $v_{0,\text{aux}}$ is the zero-sequence voltage of the auxiliary converter, i^j_{aux} is the arm current of phase j of auxiliary converter, and i^j is the output current of phase j at AC terminal of MMC-based inverter. Based on (7.2),

$$\begin{bmatrix} \frac{\mathrm{d}i^j_{\text{LD}}}{\mathrm{d}t} \\ \frac{\mathrm{d}i^j_{\text{aux}}}{\mathrm{d}t} \end{bmatrix} = A^{-1} \begin{bmatrix} v^j_{\text{aux}} - e^j + v_{0,\text{aux}} + R_{\text{aux}} i^j_{\text{aux}} - v_{0,\text{LD}} - R_{\text{LD}} i^j_{\text{LD}} \\ -v^j_{\text{com}} - e^j - \frac{1}{2} r i^j - v_{0,\text{LD}} - R_{\text{LD}} i^j_{\text{LD}} \end{bmatrix}, \tag{7.3}$$

where

$$A = \begin{bmatrix} L_{\text{LD}} & -L_{\text{aux}} \\ L_{\text{LD}} + \frac{1}{2} l & \frac{1}{2} l \end{bmatrix}, \tag{7.4}$$

$$A^{-1} = \frac{1}{M} \begin{bmatrix} \frac{1}{2} l & L_{\text{aux}} \\ -L_{\text{LD}} - \frac{1}{2} l & L_{\text{LD}} \end{bmatrix}, \tag{7.5}$$

and

$$M = L_{\text{LD}} \frac{l}{2} + L_{\text{LD}} L_{\text{aux}} + L_{\text{aux}} \frac{l}{2}. \tag{7.6}$$

Based on (7.3), dynamics of i^j_{LD} is

$$\begin{aligned} \tfrac{\mathrm{d}i^j_{\text{LD}}}{\mathrm{d}t} = \tfrac{l}{2M} \left(v^j_{\text{aux}} - e^j + v_{0,\text{aux}} + R_{\text{aux}} i^j_{\text{aux}} - v_{0,\text{LD}} - R_{\text{LD}} i^j_{\text{LD}} \right) \\ - \tfrac{L_{\text{aux}}}{M} \left(v^j_{\text{com}} - e^j + \tfrac{1}{2} r i^j + v_{0,\text{LD}} - R_{\text{LD}} i^j_{\text{LD}} \right). \end{aligned} \tag{7.7}$$

Neglecting $R_{\rm aux}$ and r in (7.7) and applying qd transformation to (7.7) yields

$$\begin{aligned}&\tfrac{{\rm d}i^{\xi}_{\rm LD}}{{\rm d}t}+\left(\tfrac{l}{2M}-\tfrac{L_{\rm aux}}{M}\right)R_{\rm LD}i^{\xi}_{\rm LD}\mp\omega i^{\eta}_{\rm LD}+\left(\tfrac{l}{2M}-\tfrac{L_{\rm aux}}{M}\right)e^{\xi}\\&=\left(\tfrac{l}{2M}v^{\xi}_{\rm aux}-\tfrac{L_{\rm aux}}{M}v^{\xi}_{\rm com}\right)\triangleq x^{\xi}_{i\rm LD}\ \ (\xi=q,d;\ \eta=d,q)\,.\end{aligned}\tag{7.8}$$

Therefore, proportional-integral (PI)-based controller can be applied to control $i^{j}_{\rm LD}$:

$$x^{\xi,{\rm ref}}_{i\rm LD}=(K_{\rm p1}+\frac{K_{\rm i1}}{s})(i^{\xi,{\rm ref}}_{\rm LD}-i^{\xi}_{\rm LD})-\left(\frac{l}{2M}-\frac{L_{\rm aux}}{M}\right)e^{\xi}\pm\omega i^{\eta}_{\rm LD}\ \ (\xi=q,d;\ \eta=d,q)\,,\tag{7.9}$$

where the superscript "ref" of $x^{\xi,{\rm ref}}_{i\rm LD}$ means the variable is the reference of $x^{\xi}_{i\rm LD}$. Based on (7.3), dynamics of $i^{j}_{\rm aux}$ is

$$\tfrac{{\rm d}i^{j}_{\rm aux}}{{\rm d}t}=x^{j}_{i\rm aux}+\tfrac{L_{\rm LD}}{M}e^{j}+\tfrac{L_{\rm LD}}{M}R_{\rm LD}i^{j}_{\rm LD}+x_{i\rm aux,v0}+x^{j}_{i\rm aux,r},\tag{7.10}$$

where

$$x^{j}_{i\rm aux}=-\frac{L_{\rm LD}v^{j}_{\rm aux}}{M}-\frac{lv^{j}_{\rm aux}}{2M}-\frac{lv^{j}_{\rm com}}{2M},\tag{7.11}$$

$$x_{i\rm aux,v0}=-\frac{L_{\rm LD}v_{0,\rm aux}}{M}-\frac{lv_{0,\rm aux}}{2M}+\frac{L_{\rm LD}v_{0,\rm LD}}{M},\tag{7.12}$$

and

$$x^{j}_{i\rm aux,r}=-\frac{L_{\rm LD}R_{\rm aux}i^{j}_{\rm aux}}{M}-\frac{lR_{\rm aux}i^{j}_{\rm aux}}{2M}-\frac{lri^{j}}{4M}.\tag{7.13}$$

Since $i^{j}_{\rm aux}$ contains multiple frequency components, proportional-based controller is used to control $i^{j}_{\rm aux}$. Neglecting $R_{\rm aux}$, r, i.e., $x^{j}_{i\rm aux,r}$ in (7.11), the reference of $x^{j}_{i\rm aux}$, i.e., $x^{j,{\rm ref}}_{i\rm aux}$ can be obtained, as shown in (7.14). Furthermore, voltage references can be obtained based on (7.15).

$$x^{j,{\rm ref}}_{i\rm aux}=K_{\rm p2}\left(i^{j,{\rm ref}}_{\rm aux}-i^{j}_{\rm aux}\right)-\frac{L_{\rm LD}}{M}e^{j}-\frac{L_{\rm LD}}{M}R_{\rm LD}i^{j}_{\rm LD}-x_{i\rm aux,v0}\tag{7.14}$$

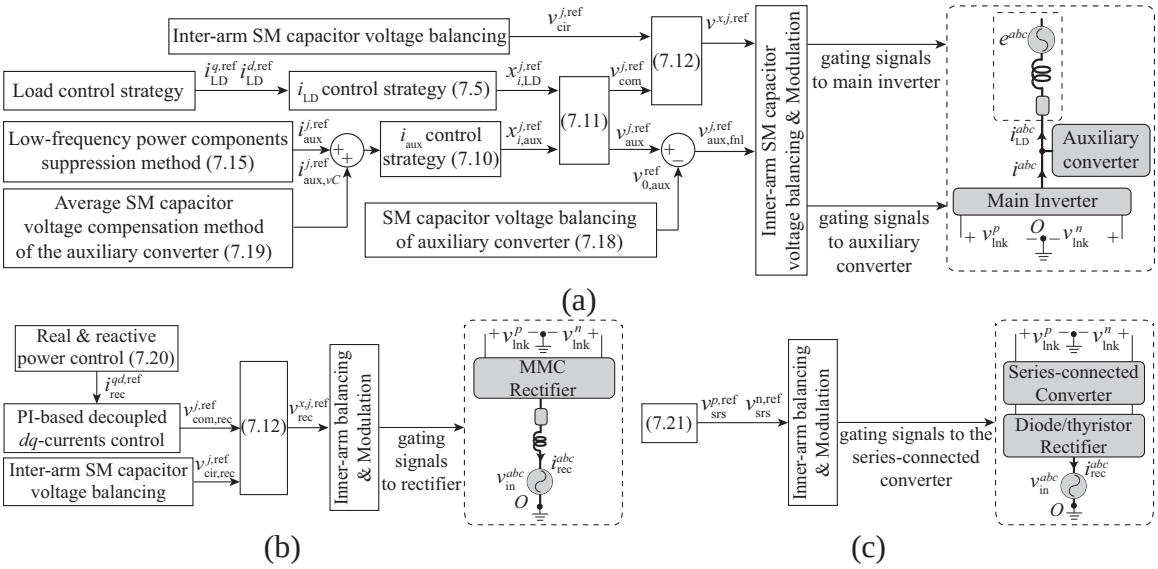

Figure 7.2: The proposed control method for the converter circuits in Fig. 7.1: (a) inverter and auxiliary converter in Fig. 7.1, (b) MMC-based rectifier in Fig. 7.1(a), and (c) series-connected converter in Fig. 7.1(b).

$$\begin{bmatrix} v_{\text{aux}}^{j,\text{ref}} \\ -v_{\text{com}}^{j,\text{ref}} \end{bmatrix} = A \begin{bmatrix} x_{i\text{LD}}^{j,\text{ref}} \\ x_{i\text{aux}}^{j,\text{ref}} \end{bmatrix} \tag{7.15}$$

7.3 Low-Frequency Suppression Method

Since an AC voltage component is injected into $v_{\text{lnk,P}}$ and $v_{\text{lnk,N}}$, voltages across the upper and lower arms are

$$\begin{aligned} v^{p,j,\text{ref}} &= \tfrac{1}{2}V_{\text{DC}} + V_{\text{AC,lnk}}\cos(\theta_{\text{AC,lnk}}) + v_{\text{com}}^{j} - v_{\text{cir}}^{j}, \\ v^{n,j,\text{ref}} &= -\tfrac{1}{2}V_{\text{DC}} - V_{\text{AC,lnk}}\cos(\theta_{\text{AC,lnk}}) + v_{\text{com}}^{j} + v_{\text{cir}}^{j}, \end{aligned} \tag{7.16}$$

where V_{DC} is the DC component of voltage between the positive and negative poles, $V_{\text{AC,lnk}}$ is magnitude of AC component of voltage between the positive/negative pole and ground, $\theta_{\text{AC,lnk}}$ is the phase of AC component of voltage between the positive/negative pole and ground, and v_{cir}^{j} is the voltage component to control the circulating current of phase j.

Currents through the upper and lower arms are

$$\begin{aligned} i^{p,j} &= \tfrac{1}{2} i^{j}_{\mathrm{LD}} + \tfrac{1}{2} i^{j}_{\mathrm{aux}} + \tfrac{1}{3} i_{\mathrm{lnk}} + i^{j}_{\mathrm{cir}}, \\ i^{n,j} &= \tfrac{1}{2} i^{j}_{\mathrm{LD}} + \tfrac{1}{2} i^{j}_{\mathrm{aux}} - \tfrac{1}{3} i_{\mathrm{lnk}} - i^{j}_{\mathrm{cir}}, \end{aligned} \tag{7.17}$$

where i_{lnk} is the current through the link, and i^{j}_{cir} is the circulating current of phase j. Based on (7.16) and (7.17), low-frequency power components of the upper and lower arms are expressed by

$$p^{p,j}_{\mathrm{LF}} = -p^{n,j}_{\mathrm{LF}} = \frac{1}{4} V_{\mathrm{DC}} i^{j}_{\mathrm{LD}} + \frac{1}{3} i_{\mathrm{lnk}} v^{j}_{\mathrm{com}}. \tag{7.18}$$

To remove $p^{p,j}_{\mathrm{LF}}$ and $p^{n,j}_{\mathrm{LF}}$, the reference of the injected auxiliary current is

$$i^{j,\mathrm{ref}}_{\mathrm{aux}} = -\frac{4 p^{p,j}_{\mathrm{LF}}}{V_{\mathrm{AC,lnk}}} \cos(\theta_{\mathrm{AC,lnk}}). \tag{7.19}$$

7.4 Capacitor Voltage Balancing Strategy

Since the current dynamics of the MMC-based rectifier and inverter is the same as those of the conventional DC-AC MMC, the existing SM capacitor voltage balancing method for the conventional DC-AC MMC is applicable to the rectifier and inverter. In addition, since an AC component is injected into $v_{\mathrm{lnk,P}}$ and $v_{\mathrm{lnk,N}}$, one more method can be applied to remove the error between $v^{j}_{C,\mathrm{com}}$ and $V_{C,\mathrm{ref}}$:

$$i^{j}_{\mathrm{cir}} = (K_{\mathrm{p2}} + \frac{K_{\mathrm{i2}}}{s})(V^{\mathrm{ref}}_{C} - v^{j}_{C,\mathrm{com}}) \cos(\theta_{\mathrm{AC,lnk}}), \tag{7.20}$$

where V^{ref}_{C} is reference of SM capacitor voltage. Capacitor voltage balancing of the auxiliary converter is based on $\alpha\beta$ transformation:

$$\begin{bmatrix} z^{\alpha}_{\mathrm{aux}} \\ z^{\beta}_{\mathrm{aux}} \\ z^{0}_{\mathrm{aux}} \end{bmatrix} = \sqrt{\tfrac{2}{3}} \begin{bmatrix} 1 & -\frac{1}{2} & -\frac{1}{2} \\ 0 & \frac{\sqrt{3}}{2} & -\frac{\sqrt{3}}{2} \\ \frac{1}{\sqrt{2}} & \frac{1}{\sqrt{2}} & \frac{1}{\sqrt{2}} \end{bmatrix} \begin{bmatrix} z^{a}_{\mathrm{aux}} \\ z^{b}_{\mathrm{aux}} \\ z^{c}_{\mathrm{aux}} \end{bmatrix}, \tag{7.21}$$

where $z^j_{\rm aux}$ denotes $v^j_{\rm aux}$, $i^j_{\rm aux}$, $v^j_{C,\rm aux}$, and $p^j_{\rm aux}$. Based on (7.21),

$$\begin{aligned} p^{\alpha}_{\rm aux} &= \tfrac{\sqrt{3}}{2}\left(v^0_{\rm aux} i^{\alpha}_{\rm aux} + v^{\alpha}_{\rm aux} i^0_{\rm aux}\right) + \tfrac{\sqrt{6}}{4}\left(v^{\alpha}_{\rm aux} i^{\alpha}_{\rm aux} - v^{\beta}_{\rm aux} i^{\beta}_{\rm aux}\right), \\ p^{\beta}_{\rm aux} &= \tfrac{\sqrt{3}}{2}\left(v^0_{\rm aux} i^{\beta}_{\rm aux} + v^{\beta}_{\rm aux} i^0_{\rm aux}\right) - \tfrac{\sqrt{6}}{4}\left(v^{\alpha}_{\rm aux} i^{\beta}_{\rm aux} + v^{\beta}_{\rm aux} i^{\alpha}_{\rm aux}\right). \end{aligned} \tag{7.22}$$

Therefore, the SM capacitor voltages of the auxiliary converter can be balanced by injecting a zero-sequence voltage:

$$\begin{aligned} v^{\rm ref}_{0,\rm aux} &= -\tfrac{1}{\sqrt{3}} v^0_{\rm aux} \\ &= -K_{\rm p2} v^{\alpha}_{C,\rm aux} \cos(\theta_{\rm LD} + \phi_{\rm LD}) p^{p,a}_{\rm LF} \cos(\theta_{\rm AC,lnk}) \\ &\quad - K_{\rm p2} v^{\beta}_{C,\rm aux} \sin(\theta_{\rm LD} + \phi_{\rm LD}) p^{p,a}_{\rm LF} \cos(\theta_{\rm AC,lnk}). \end{aligned} \tag{7.23}$$

In addition, the average capacitor voltage of all the SMs of the auxiliary converter can be maintained based on

$$i^{j,\rm ref}_{\rm aux,vC} = K_{\rm p3}(V^{\rm ref}_{C,\rm aux} - \tfrac{1}{\sqrt{3}} v^0_{C,\rm aux}) \cos(\theta^j_{\rm com}), \tag{7.24}$$

where $V^{\rm ref}_{C,\rm aux}$ is the SM capacitor voltage reference of the auxiliary converter and $v^0_{C,\rm aux}$ is the zero-sequence component of three-phase average SM capacitor voltages of the auxiliary converter. For the MMC rectifier, as illustrated in Fig. 7.1(a), the average capacitor voltage of all the SMs is maintained based on

$$P^{\rm ref}_{\rm rec} = P^{\rm ref}_{\rm LD} + (K_{\rm p4} + \tfrac{K_{\rm i4}}{s})(V^{\rm ref}_{C} - \bar{v}_{C,\rm rec}), \tag{7.25}$$

where $\bar{v}_{C,\rm rec}$ is the average SM capacitor voltage of the MMC-based rectifier. For the series-connected converter, as illustrated in Fig. 7.1(b), references of output voltages of the series-connected converters in the positive and negative poles are

$$v^{x,\rm ref}_{\rm srs} = \pm V_{\rm AC,lnk} \cos(\theta_{\rm AC,lnk}) \mp (K_{\rm p4} + \frac{K_{\rm i4}}{s})(V^{\rm ref}_{C,\rm srs} - v^{x}_{C,\rm srs}) \ \ (x = p, n), \tag{7.26}$$

where $V_{C,\mathrm{srs}}^{\mathrm{ref}}$ is the reference of the SM capacitor voltage. The proposed control method is shown in Fig. 7.2.

7.5 Simulation Results

In this section, the study results conducted in the PSCAD/EMTDC software environment are presented to verify the effectiveness of the proposed strategies. Fig. 7.1(b) presents the study system. The parameters of the study system are listed in Table 7.1. The permanent magnet synchronous machine (PMSM) is loaded at the rated torque. Flux-oriented control is applied to the PMSM. The overall control system is provided in Figs. 7.2(a) and (c).

Table 7.1: Parameters of the study system of Fig. 7.1(b)

Main Inverter	Value
Number of SMs in each arm N	6
Submodule capacitor C	8000 μF
Inductance of arm inductor l	6 mH
Auxiliary Converter and Series-connected converter	**Value**
Number of SMs in each arm N_{aux} and N_{srs}	4
Submodule capacitor C_{aux} and C_{srs}	8000 μF
Inductance of arm inductor L_{aux}	7 mH
Rating	**Value**
V_{DC}	40 kV
$V_{\mathrm{AC,lnk}}$	6 kV
$f_{\mathrm{AC,lnk}}$	120 Hz
V_C^{ref}	6 kV

Figure 7.3 illustrates waveforms of the proposed converter in Fig. 7.1(b) during one period of the load-side fundamental frequency voltage, i.e., T_{LD} under the conditions of $f_{\mathrm{LD}} = 0.05$ Hz and $f_{\mathrm{lnk}} = 120$ Hz. Figure 7.3(a) shows the link voltage, which contains both DC and AC components. Figure 7.3(b) shows the current flowing through the link, which is dominated by a DC component. Figure 7.3(c) shows q- and d-axis components of load currents and their references, which verifies that the load current is properly controlled. Figure 7.3(d) illustrates balanced line-to-line voltages of the load. Figure 7.3(e) shows the arm currents of phase a, which contain both f_{LD} and $f_{\mathrm{AC,lnk}}$ components. Fig-

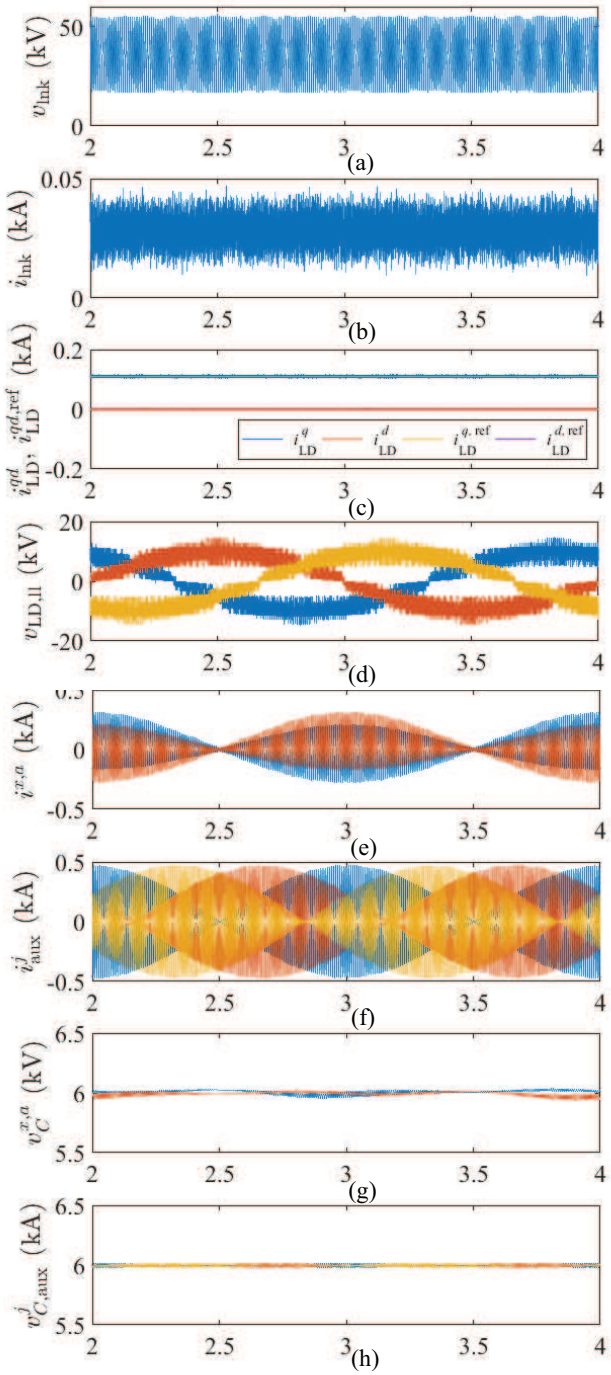

Figure 7.3: Waveforms of the proposed MMC: (a) voltage across the link, (b) current through the link, (c) the q- and d-axis components of the load currents and their references, (d) line-to-line voltages at the AC terminal of the main inverter, (e) arm currents of phase a of the inverter, (f) arm current of phase a of the auxiliary converter, (g) SM capacitor voltages of phase a of the inverter, and (h) SM capacitor voltages of phase a of the auxiliary converter.

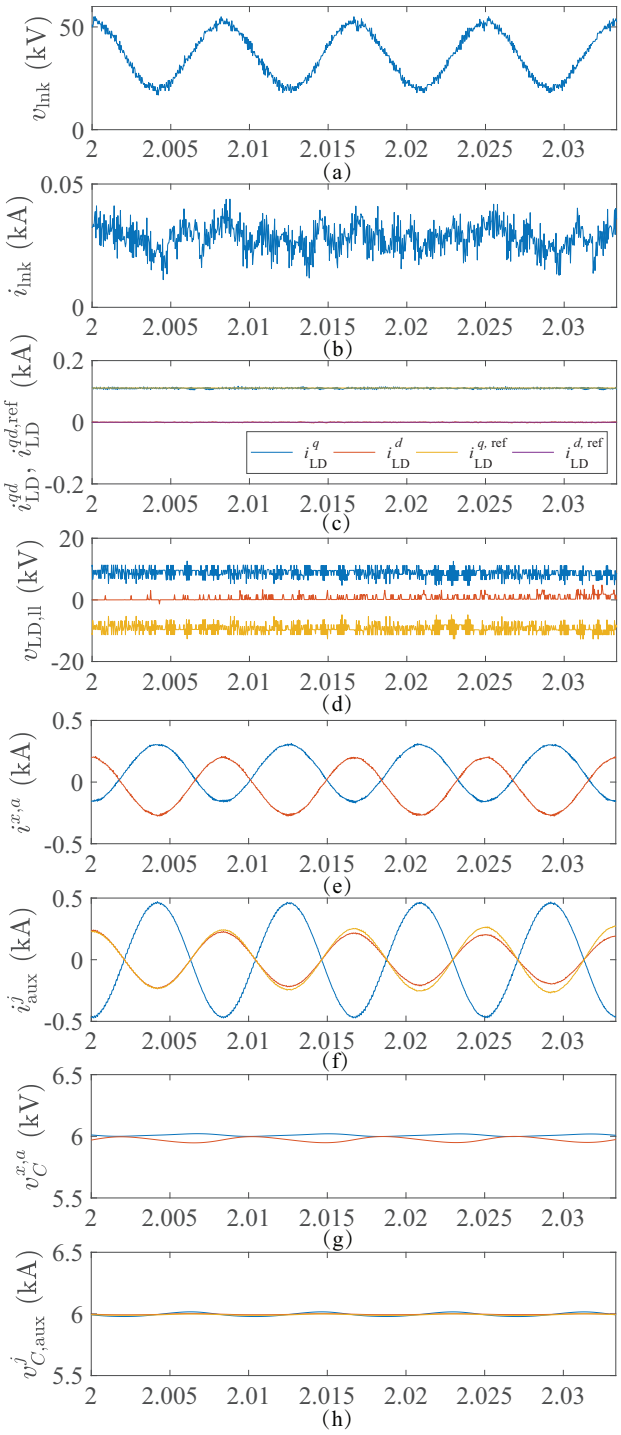

Figure 7.4: Zoomed-in waveforms of the proposed MMC: (a) voltage across the link, (b) current through the link, (c) q- and d-axis components of the load currents and their references, (d) line-to-line voltages at the AC terminal of the main inverter, (e) arm currents of phase a of the inverter, (f) arm current of phase a of the auxiliary converter, (g) SM capacitor voltages of phase a of the inverter, and (h) SM capacitor voltages of phase a of the auxiliary converter.

ure 7.3(f) shows the three-phase arm currents of the auxiliary converter, which contain both f_{LD} and $f_{\mathrm{AC,lnk}}$ components as well. Figures 7.3(g) and (f) show the SM capacitor voltages of phase a of the inverter and the three-phase SM capacitor voltages of the auxiliary converter, respectively, which are well regulated around their references. Figure 7.4 illustrates the corresponding zoomed-in waveforms of the proposed converter in Fig. 7.2(b) during several $T_{\mathrm{AC,lnk}}$. Figure 7.4(a) shows the zoomed-in link voltage, where the AC component is presented clearly. Figures 7.4(b) and (c) illustrate the zoomed-in DC-component-dominated link current and well-regulated load currents respectively. Figure 7.4(d) illustrates the zoomed-in line-to-line voltages at the AC terminal of the inverter. Figures 7.4(e) and (f) illustrate the zoomed-in arm currents of phase a of the inverter and three-phase arm currents of the auxiliary converter, respectively, where the high-frequency AC components can be observed clearly. Figures 7.4(g) and (h) illustrate the zoomed-in well-regulated SM capacitor voltages of phase a of the inverter and the three-phase SM capacitor voltages of the auxiliary converter, respectively.

CHAPTER 8

AC-AC MMC-BASED PARTIALLY-RATED SOLID-STATE TRANSFORMER

In this chapter, an MMC-based partially-rated solid-state transformer (PSST) along with its supporting control strategies is proposed and investigated for power flow control. The proposed PSST borrows the features of the MMC and combines them with new control strategies to enable the MMC-based PSST. Figure 8.1 illustrates a simplified schematic of a power system as well as examples of typical voltage ratings [110]. The proposed MMC-based PSST can be applied as a replacement for the transformers in the red dashed circles in Fig. 8.1, where the AC-AC MMC can be integrated in either the primary- or secondary-side of the transformer. Simulation studies in the PSCAD/EMTDC software environment are carried out to validate the performance and effectiveness of the proposed MMC-based PSSTs and their supporting control methods.

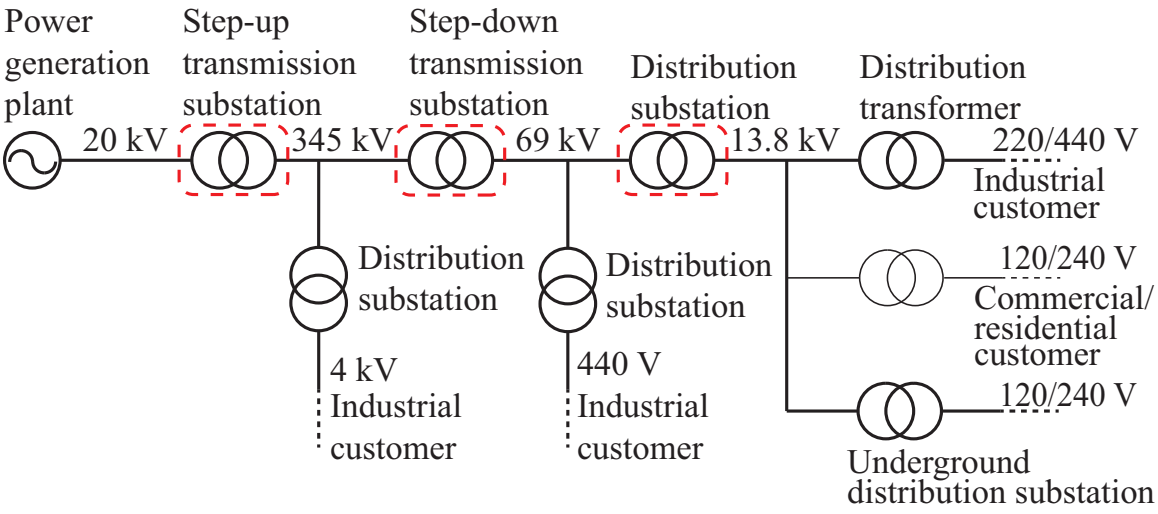

Figure 8.1: Potential examples of the PSST used in the power system.

8.1 The Proposed AC-AC MMC

8.1.1 Circuit topology

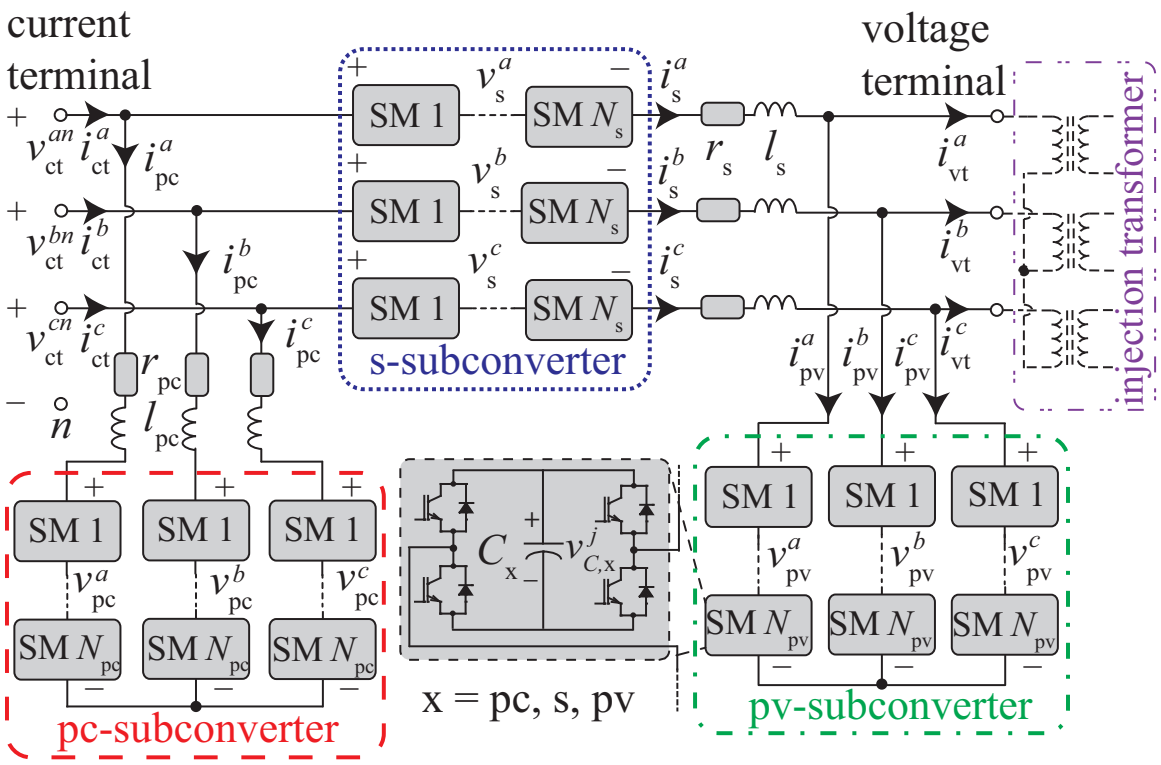

Figure 8.2: Circuit diagram of the proposed AC-AC MMC.

The circuit diagram of the proposed AC-AC MMC, i.e., the power electronics part of the PSST, is illustrated in Fig. 8.2. The MMC consists of three subconverters, i.e., the parallel-voltage (pv-) subconverter, the series (s-) subconverter, and the parallel-current (pc-) subconverter, which are illustrated in the red dashed, blue dotted, and green dashed dotted blocks of Fig. 8.2, respectively. Each subconverter consists of three SM clusters. The pc- and s-subconverters have series-connected inductors, while the pv-subconverter has no series-connected inductor. The terminal at the side of the pc-subconverter is termed current terminal (ct), which is connected in parallel with the conventional magnetic transformer to adjust the grid current. The virtual neutral point of the current terminal is illustrated by point "n" in Fig. 8.2. The other terminal at the side of the pv-subconverter is termed

voltage terminal (vt). The voltage terminal is connected in series with the main magnetic part of the PSST through an injection transformer. The injection transformer is illustrated in the purple dashed double-dotted block of Fig. 8.2. Since the line-to-line primary-side voltage of the injection transformer is determined by v_{pv}^{j}, the secondary-side voltage of the injection transformer can be controlled to adjust the output voltage of the PSST.

8.1.2 Internal dynamics and current control

Based on the averaged model, dynamics of currents through pc- and s-subconverter, i.e., i_{pc}^{j} and i_{s}^{j} in the AC-AC MMC can be summarized by

$$v_{\mathrm{ct}}^{jn} - \left(v_{\mathrm{pc}}^{j} - v_{\mathrm{pc}}^{z}\right) = \left(r_{\mathrm{pc}} + l_{\mathrm{pc}}\tfrac{\mathrm{d}}{\mathrm{d}t}\right) i_{\mathrm{pc}}^{j}, \tag{8.1a}$$

$$v_{\mathrm{ct}}^{jn} + v_{\mathrm{s}}^{j} - \left(v_{\mathrm{pv}}^{j} - v_{\mathrm{pv}}^{z}\right) = \left(r_{\mathrm{s}} + l_{\mathrm{s}}\tfrac{\mathrm{d}}{\mathrm{d}t}\right) i_{\mathrm{s}}^{j}, \tag{8.1b}$$

where v_{ct}^{jn} is the voltage between phase j and the virtual neutral point "n" of the ct-terminal, v_{x}^{j} is the voltage across phase j cluster of x-subconverter (x = pc, s, pv), and v_{pc}^{z} is the zero-sequence component of v_{x}^{j}.

Based on (8.1a) and (8.1b), i_{pc}^{j} and i_{s}^{j} can be controlled by

$$v_{\mathrm{pc}}^{j,\mathrm{ref}} - v_{\mathrm{pc}}^{z,\mathrm{ref}} = -K_{\mathrm{p}}\left(i_{\mathrm{pc}}^{j,\mathrm{ref}} - i_{\mathrm{pc}}^{j}\right) + v_{\mathrm{ct}}^{jn}, \tag{8.2a}$$

$$v_{\mathrm{s}}^{j,\mathrm{ref}} = K_{\mathrm{p}}\left(i_{\mathrm{s}}^{j,\mathrm{ref}} - i_{\mathrm{s}}^{j}\right) + \left(v_{\mathrm{pv}}^{jn} - v_{\mathrm{pv}}^{z,\mathrm{ref}}\right) - v_{\mathrm{ct}}^{jn}, \tag{8.2b}$$

where the superscript ref denotes the references of the variables, and v_{pv}^{j} is determined by power flow references. If $i_{\mathrm{s}}^{j,\mathrm{ref}}$ or $i_{\mathrm{pc}}^{j,\mathrm{ref}}$ only contains fundamental-frequency components (positive- and negative-sequence components), the proportional-integral (PI) controller can be applied to control i_{s}^{j} or i_{pc}^{j} [106]. In addition, since i_{vt}^{j} is determined by the load of the PSST, i_{pv}^{j} is regulated through controlling i_{s}^{j}.

8.1.3 Inter-subconverter energy adjustment strategy

To regulate the average SM capacitor voltages of the subconverters at their references, the power flows among the subconverters need to be controlled. The positive-sequence component of $i_{\rm pc}^{j}$ can be decomposed into the in-phase and quadrature components with respect to the phase angle of $v_{\rm ct}^{j,\rm pos}$. The in-phase component, i.e., $i_{\rm pc}^{q,\rm pos}$, is regulated to adjust $\bar{v}_{C,\rm pc}$, based on:

$$i_{\rm pc}^{q,\rm pos,ref} = \left(K_{\rm p} + \frac{K_{\rm i}}{s}\right)\left(V_{C,\rm pc}^{\rm ref} - \bar{v}_{C,\rm pc}\right), \tag{8.3}$$

where $V_{C,\rm pc}^{\rm ref}$ is the reference of $\bar{v}_{C,\rm pc}$. The quadrature component, i.e., $i_{\rm pc}^{d,\rm pos}$, is regulated to control $i_{\rm ct}^{d}$ based on:

$$i_{\rm pc}^{d,\rm pos,ref} = i_{\rm ct}^{d,\rm ref} - i_{\rm s}^{d,\rm ref}, \tag{8.4}$$

where $Q_{\rm ct}^{\rm ref}$ is the reference of $Q_{\rm ct}$, $V_{\rm ct}^{q}$ is the q-axis component of $v_{\rm ct}^{j}$, and $i_{\rm s}^{d}$ is the d-axis component of $i_{\rm s}^{j}$.

Similar to $i_{\rm pc}^{j}$, the three-phase balanced set of $i_{\rm s}^{j}$ can be decomposed into the in-phase and quadrature components with respect to the phase angle of $v_{\rm pv}^{j,\rm pos}$. The in-phase component, i.e., $i_{\rm s}^{q,\rm pos}$, is regulated to adjust $\bar{v}_{C,\rm pv}$ based on:

$$i_{\rm s}^{q,\rm pos,ref} = \left(K_{\rm p} + \frac{K_{\rm i}}{s}\right)\left(V_{C,\rm pv}^{\rm ref} - \bar{v}_{C,\rm pv}\right), \tag{8.5}$$

where $V_{C,\rm pv}^{\rm ref}$ is the reference of $\bar{v}_{C,\rm pv}$. The quadrature component, i.e., $i_{\rm s}^{d,\rm pos}$, is regulated to adjust the average SM capacitor voltage of the s-subconverter, i.e., $\bar{v}_{C,\rm s}$, based on

$$\begin{aligned} i_{\rm s}^{d,\rm pos,ref} = {} & \mathrm{sgn}\left(\cos\left(\phi_{v,\rm pv}^{\rm pos} - \tfrac{\pi}{2} - \phi_{v,\rm s}^{\rm pos}\right)\right) \\ & \left(K_{\rm p} + \tfrac{K_{\rm i}}{s}\right)\left(V_{C,\rm s}^{\rm ref} - \bar{v}_{C,\rm s}\right), \end{aligned} \tag{8.6}$$

where $\phi_{v,\rm pv}^{\rm pos}$ is the initial phase angle of $v_{\rm pv}^{j,\rm pos}$, $\phi_{v,\rm s}^{\rm pos}$ is the initial phase angle of $v_{\rm s}^{j,\rm pos}$, and

$V_{C,\mathrm{s}}^{\mathrm{ref}}$ is the reference of $\bar{v}_{C,\mathrm{s}}$. The validity condition of (8.6) is that the phase difference between $\phi_{v,\mathrm{pv}}^{\mathrm{pos}}$ and $\phi_{v,\mathrm{s}}^{\mathrm{pos}}$ should be between 45° and 135°. To obtain the safety margin, the phase difference between $\phi_{v,\mathrm{pv}}^{\mathrm{pos}}$ and $\phi_{v,\mathrm{s}}^{\mathrm{pos}}$ should be between $\gamma_{\min}$ and $\pi - \gamma_{\min}$, where $\gamma_{\min}$ must be between 45° and 90°. In addition, to decrease the reactive power in both the s- and pv-subconverters, $\left|\phi_{v,\mathrm{pv}}^{\mathrm{pos}} - \phi_{v,\mathrm{s}}^{\mathrm{pos}}\right|$ should be as close as possible to 90°.

8.1.4 Inner-subconverter energy balancing strategy

To maintain the SM capacitor voltages balanced within each subconverter, the dynamics of each subconverter are transferred to the $\alpha\beta$-frame by using the $\alpha\beta$-transformation:

$$\begin{bmatrix} f_{\mathrm{x}}^{\alpha} \\ f_{\mathrm{x}}^{\beta} \\ f_{\mathrm{x}}^{z} \end{bmatrix} = \sqrt{\frac{2}{3}} \begin{bmatrix} 1 & -\frac{1}{2} & -\frac{1}{2} \\ 0 & \frac{\sqrt{3}}{2} & -\frac{\sqrt{3}}{2} \\ \frac{1}{\sqrt{2}} & \frac{1}{\sqrt{2}} & \frac{1}{\sqrt{2}} \end{bmatrix} \begin{bmatrix} f_{\mathrm{x}}^{a} \\ f_{\mathrm{x}}^{b} \\ f_{\mathrm{x}}^{c} \end{bmatrix}, \tag{8.7}$$

where the subscript x indicates pv, s, and pc and f_{x}^{j} denotes v_{x}^{j}, i_{x}^{j}, and $\bar{v}_{C,\mathrm{x}}^{j}$. For the pv- and pc-subconverters, the zero-sequence component of v_{x}^{j}, i.e., v_{x}^{z} is used to maintain the energy of the three-phase clusters balanced within each subconverter, i.e.,

$$v_{\mathrm{x}}^{\mathrm{z,ref}} = -K_{\mathrm{p}} \left(\bar{v}_{C,\mathrm{x}}^{\alpha} \cos(\theta_{i,\mathrm{x}}^{\mathrm{pos}}) + \bar{v}_{C,\mathrm{x}}^{\beta} \sin(\theta_{i,\mathrm{x}}^{\mathrm{pos}}) \right), \tag{8.8}$$

where $\theta_{i,\mathrm{x}}$ is the phase angle of $i_{\mathrm{x}}^{j,\mathrm{pos}}$, i.e., $\omega t + \phi_{i,\mathrm{x}}$. For the s-subconverter, the negative-sequence component of i_{s}^{j} is regulated to maintain energy of the three clusters balanced based on:

$$\begin{aligned} i_{\mathrm{s}}^{\alpha,\mathrm{neg,ref}} &= -K_{\mathrm{p}} \bar{v}_{C,\mathrm{s}}^{\alpha} \cos\left(\theta_{v,\mathrm{s}}^{\mathrm{pos}}\right) + K_{\mathrm{p}} \bar{v}_{C,\mathrm{s}}^{\beta} \sin\left(\theta_{v,\mathrm{s}}^{\mathrm{pos}}\right), \\ i_{\mathrm{s}}^{\beta,\mathrm{neg,ref}} &= K_{\mathrm{p}} \bar{v}_{C,\mathrm{s}}^{\alpha} \sin\left(\theta_{v,\mathrm{s}}^{\mathrm{pos}}\right) + K_{\mathrm{p}} \bar{v}_{C,\mathrm{s}}^{\beta} \cos\left(\theta_{v,\mathrm{s}}^{\mathrm{pos}}\right), \end{aligned} \tag{8.9}$$

where $\theta_{v,\mathrm{s}}^{\mathrm{pos}}$ is the phase angle of $v_{\mathrm{s}}^{j,\mathrm{pos}}$, i.e., $\omega t + \phi_{v,\mathrm{s}}^{\mathrm{pos}}$. To prevent the injected negative-sequence current components from flowing into the grid, $i_{\mathrm{s}}^{\alpha,\mathrm{neg,ref}}$ and $i_{\mathrm{s}}^{\beta,\mathrm{neg,ref}}$ should be added into the $i_{\mathrm{pc}}^{j,\mathrm{ref}}$. To prevent the injected negative-sequence current components from

flowing into the grid, $i_{\mathrm{s}}^{\alpha,\mathrm{neg,ref}}$ and $i_{\mathrm{s}}^{\beta,\mathrm{neg,ref}}$ should be added to $i_{\mathrm{pc}}^{j,\mathrm{ref}}$.

8.2 Operation of the Proposed MMC-based PSST to Control Power Flow

Figure 8.3 illustrates the proposed MMC-based PSST in Scenario A, where the PSST should be able to adjust real and reactive power flows. The AC-AC MMC in Fig. 8.3 is developed based on the AC-AC MMC in Fig. 8.2, where another pair of s- and pv-subconverters is added.

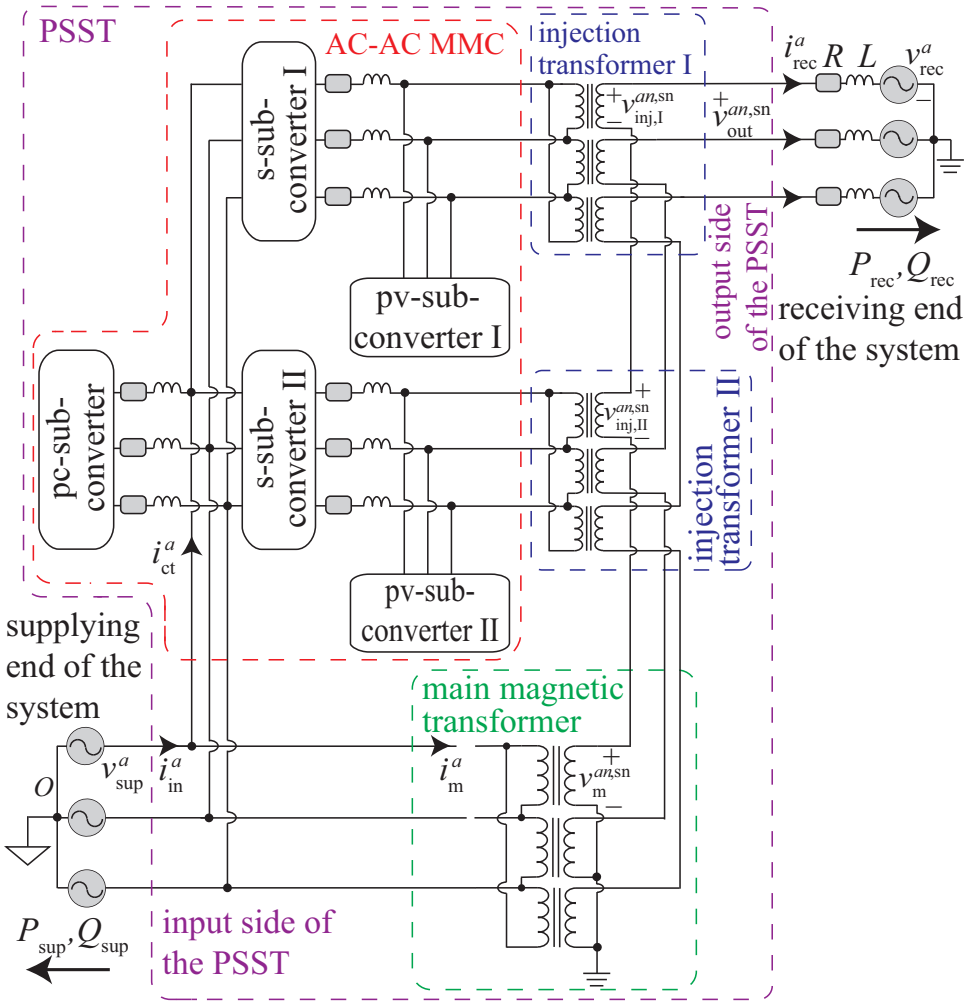

Figure 8.3: Circuit diagram of the proposed MMC-based PSST in Scenario A.

As illustrated in Fig. 8.3, the two pairs of the s- and pv-subconverters are connected in parallel at the common current terminal and in series through two injection transformers. The two series-connected injection transformers are connected in series with the secondary

side of the main magnetic transformer to constitute the output side of the PSST. The output side of the PSST is connected to the receiving end of the system through series connected inductor and resistor. The current terminal of the AC-AC MMC and the primary side of the conventional magnetic transformer are connected in parallel to form the input side of the PSST. The input side of the PSST is directly connected to the supplying end of the system.

8.2.1 Power flow control strategy

To adjust the receiving-end real and reactive powers, v_{pv}^{j} is controlled to regulate the receiving-end currents. Based on Fig. 8.3, the references of the secondary-side voltage of the injection transformers are generated by

$$\begin{aligned} v_{\mathrm{inj,I}}^{q,\mathrm{sn,ref}} + v_{\mathrm{inj,II}}^{q,\mathrm{sn,ref}} &= \left(K_{\mathrm{p}} + \tfrac{K_{\mathrm{i}}}{s}\right)\left(i_{\mathrm{rec}}^{q,\mathrm{ref}} - i_{\mathrm{rec}}^{q}\right) - \omega L i_{\mathrm{rec}}^{d} - v_{\mathrm{m}}^{q,\mathrm{sn}}, \\ v_{\mathrm{inj,I}}^{d,\mathrm{sn,ref}} + v_{\mathrm{inj,II}}^{d,\mathrm{sn,ref}} &= \left(K_{\mathrm{p}} + \tfrac{K_{\mathrm{i}}}{s}\right)\left(i_{\mathrm{rec}}^{d,\mathrm{ref}} - i_{\mathrm{rec}}^{d}\right) + \omega L i_{\mathrm{rec}}^{q} - v_{\mathrm{m}}^{d,\mathrm{sn}}, \end{aligned} \tag{8.10}$$

where the superscript sn indicates secondary-side of the transformers, $v_{\mathrm{pv,I}}^{\xi,\mathrm{sn,ref}}$ and $v_{\mathrm{pv,II}}^{\xi,\mathrm{sn,ref}}$ are the references of the ξ-axis components of the three-phase secondary-side voltages of injection transformer I and II ($\xi = q, d$), $v_{\mathrm{m}}^{\xi,\mathrm{sn}}$ is the ξ-axis component of the three-phase secondary-side voltages of the main magnetic transformer, and i_{rec}^{ξ} is the ξ-axis current component of the receiving end. For the supplying end, i_{ct}^{d} of the AC-AC MMC is controlled to adjust the reactive power based on

$$i_{\mathrm{ct}}^{d,\mathrm{ref}} = -\frac{Q_{\mathrm{sup}}^{\mathrm{ref}}}{V_{\mathrm{sup}}^{q}} - i_{\mathrm{m}}^{d}, \tag{8.11}$$

where $i_{\mathrm{ct}}^{d,\mathrm{ref}}$ is the reference of the d-axis current of the current terminal of the MMC, $Q_{\mathrm{sup}}^{\mathrm{ref}}$ is the reference of the reactive power of the supplying end, V_{sup}^{q} is the q-axis voltage component of the supplying end, and i_{m}^{d} is the d-axis component of the three-phase primary-side currents of the main magnetic transformer.

8.2.2 Energy adjustment strategy for the s-subconverter

As presented in Section 8.1.3, the validity condition for (8.6) is that the phase angle difference between $\phi_{v,\mathrm{pv}}^{\mathrm{pos}}$ and $\phi_{v,\mathrm{s}}^{\mathrm{pos}}$ should be between $\gamma_{\min}$ and $\pi - \gamma_{\min}$. However, if the AC-AC MMC has only one pair of s- and pv-subconverters, as illustrated in Fig. 8.2, both $\phi_{v,\mathrm{pv}}^{\mathrm{pos}}$ and $\phi_{v,\mathrm{s}}^{\mathrm{pos}}$ are determined by the references of the receiving-end real and reactive powers. Therefore, the validity condition may not be satisfied under certain conditions, e.g., the condition in Fig. 8.4(a). To solve the problem, as illustrated in Fig. 8.3, two pairs of s- and pv-subconverters are integrated. For the condition in Fig. 8.4(a), the phasor diagram can be modified into Fig. 8.4(b). Therefore, the validity condition can be guaranteed in each pair of s- and pv-subconverters.

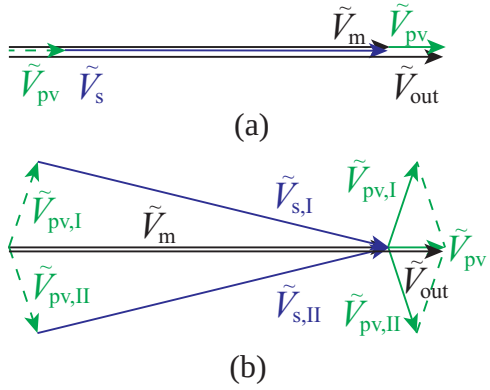

Figure 8.4: Phasor diagrams of $\tilde{V}_{\mathrm{s}}$ and $\tilde{V}_{\mathrm{pv}}$: (a) an example of invalid energy adjustment strategy for the s-subconverter, (b) solution to the problem shown in Fig. 8.4(a).

8.2.3 Compensation range of the output voltage

To simplify expressions, in Section 8.2.3, the ratio and configuration of the main magnetic transformer is assumed to be the same as those of the injection transformers. Based on Fig. 8.3 and the s-subconverter energy adjustment strategy in Section 8.2.2, the output-side voltage compensation range of the PSST is illustrated by the shaded and striped areas in

Fig. 8.5. In Fig. 8.5, the critical angles are

$$\begin{aligned}\delta_1 &= \arcsin\left(y_1 \sin(\gamma_{\min})\right), \\ \delta_2 &= \pi - \arcsin\left(y_2 \sin(\gamma_{\min})\right),\end{aligned} \tag{8.12}$$

where

$$\begin{aligned}y_1 &= -\cos(\gamma_{\min})\eta + \sqrt{1-\sin^2(\gamma_{\min})\eta^2}, \\ y_2 &= \cos(\gamma_{\min})\eta + \sqrt{1-\sin^2(\gamma_{\min})\eta^2},\end{aligned} \tag{8.13}$$

and η is the ratio of the maximum $\left|v_{\mathrm{pv}}^{j,\mathrm{pos}}\right|$ to $|v_{\mathrm{m}}^{jn,\mathrm{pm}}|$. Based on Fig. 8.5, the compensation range contains two sectors, i.e., shaded area X in Fig. 8.5, and two rhombuses, i.e., striped area Y in Fig. 8.5. The radius of the sectors is twice the maximum $\left|v_{\mathrm{pv}}^{j,\mathrm{pos}}\right|$ while the side length of the rhombuses is the maximum $\left|v_{\mathrm{pv}}^{j,\mathrm{pos}}\right|$. If the phasor reference of the sum of the two pv-subconverters, i.e., $\tilde{V}_{\mathrm{pv}}^{\mathrm{ref}}$ is in the shaded area X, each pair of s- and pv-subconverters can individually achieve a valid energy adjustment strategy. Therefore, $\tilde{V}_{\mathrm{pv}}^{\mathrm{ref}}$ can be distributed into the two pv-subconverters evenly, i.e.,

$$\tilde{V}_{\mathrm{pv,I}}^{\mathrm{ref}} = \tilde{V}_{\mathrm{pv,II}}^{\mathrm{ref}} = \frac{1}{2}\tilde{V}_{\mathrm{pv}}^{\mathrm{ref}}. \tag{8.14}$$

If $\tilde{V}_{\mathrm{pv}}^{\mathrm{ref}}$ is in the striped area Y, based on the parallelogram law, $\tilde{V}_{\mathrm{pv}}^{\mathrm{ref}}$ needs to be formed by $\tilde{V}_{\mathrm{pv,I}}^{\mathrm{ref}}$ and $\tilde{V}_{\mathrm{pv,II}}^{\mathrm{ref}}$. The minimum distance from the neutral to the boundary of the shaded area, i.e., $\left|\tilde{V}_{\mathrm{pv,min}}\right|$ in Fig. 8.5, is

$$\left|\tilde{V}_{\mathrm{pv,min}}\right| = \sin\left(2\delta_2 - \pi\right)\eta\left|\tilde{V}_{\mathrm{m}}\right|. \tag{8.15}$$

The overall control strategy for the PSST in Scenario A is summarized in Fig. 8.6.

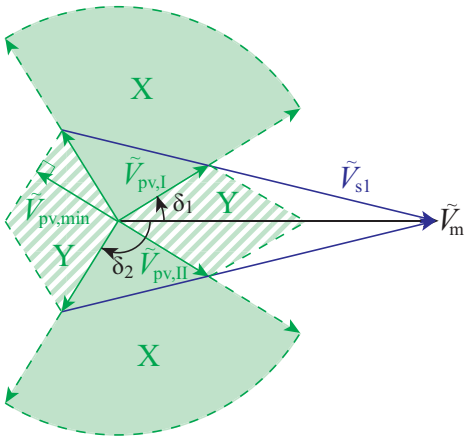

Figure 8.5: Output-side voltage compensation range of the PSST in Fig. 8.3.

8.3 Simulation Results

To demonstrate the performance and effectiveness of the proposed control strategies in Scenario A, the proposed MMC-based PSST illustrated in Fig. 8.3, is simulated in the PSCAD/EMTDC software environment. Parameters of the study system are listed in Table 8.1. The setpoint of the receiving-end real power is ramped down from 40 MW to 10 MW. The setpoints of the reactive powers of the receiving and supplying ends are 10 MVAr and 30 MVAr, respectively.

Table 8.1: Parameters of the study system of Fig. 8.3

main transformer	Value	pv-subconverter	Value
capacity	50 MVA	N_{pv}	4
primary-winding voltage	34.5 kV	C_{pv}	10000 μF
secondary-winding voltage	6.9 kV	s-subconverter	Value
leakage reactance	0.03 pu	N_{s}	12
basic operation frequency	60 Hz	C_{s}	1000 μF
injection transformer (1-ph)	Value	l_{s}	2.5 mH
capacity	1.7 MVA	r_{s}	0.5 mΩ
primary-winding voltage	2.0 kV	pc-subconverter	Value
secondary-winding voltage	400 V	N_{pc}	12
leakage reactance	0.03 pu	C_{pc}	3000 μF
basic operation frequency	60 Hz	l_{pc}	5.0 mH
receive end	Value	r_{pc}	1.0 mΩ
V_{rcv}	6.9 kV	supply end	Value
L	2.5 mH	V_{sup}	34.5 kV
R	1.2 mΩ		

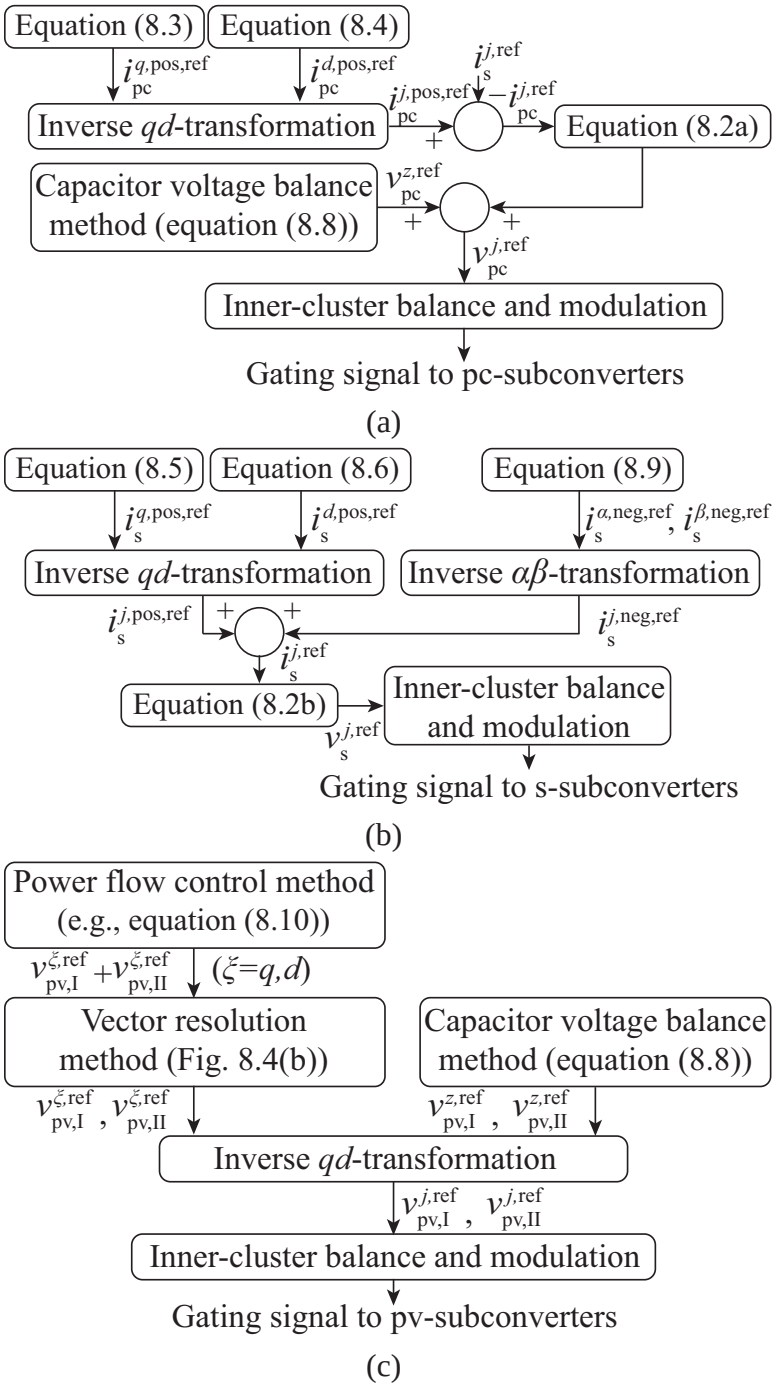

Figure 8.6: Control block diagrams of the proposed MMC-based PSST in Scenario A (Fig. 8.3): (a) control of the pc-subconverter, (b) control of the s-subconverters, and (c) control of the pv-subconverters.

As illustrated in Fig. 8.7(a), the transfered real power is well-regulated to follow its reference. Fig. 8.7(b) illustrates reactive powers of the supplying and receiving ends, which are controlled at their references. Fig. 8.7(c) shows the secondary-side voltage of the magnetic transformer, the sum of the secondary-side voltages of the two injection transformers, and the output voltage of the MMC-based PSST. As illustrated in Fig. 8.7(c), the output voltage of the PSST is actively adjusted by controlling the AC-AC MMC. Fig. 8.7(d) shows the primary-side current of the magnetic transformer, the current-terminal current of the MMC, and the input current of the PSST. As illustrated, the input current of the PSST is actively regulated by controlling the AC-AC MMC. Figs. 8.7(e)-(g) illustrate the average SM capacitor voltages of the pv-, s-, and pc-subconverters, respectively. As shown, all the SM capacitor voltages are maintained balanced during the real power ramping process.

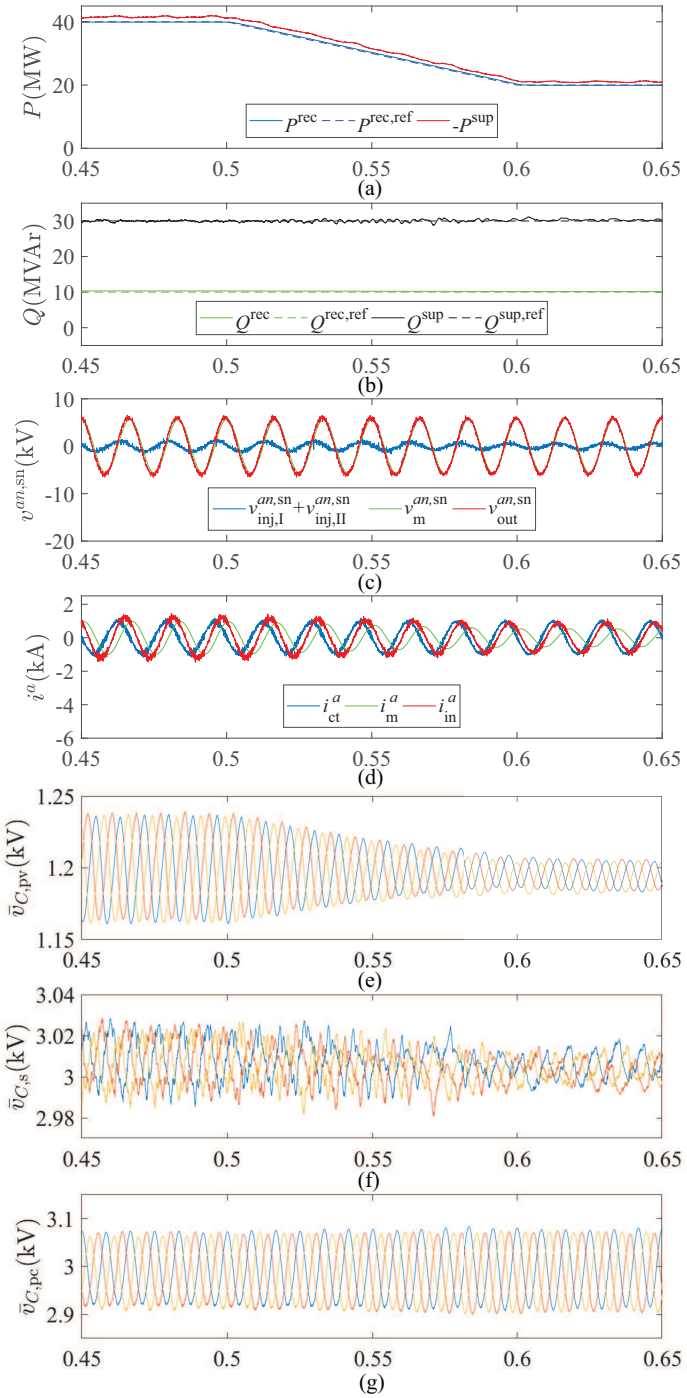

Figure 8.7: Simulated waveforms of the proposed AC-AC MMC-based PSST (Fig. 8.3) in Scenario A: (a) supplying- and receiving-end real powers, (b) supplying- and receiving-end reactive powers, (c) output-side voltages of the proposed PSST (phase a), (d) input-side currents of the proposed PSST (phase a), (e) average SM capacitor voltages of phases a, b, and c in the pv-subconverter, (f) average SM capacitor voltages of phases a, b, and c in the s-subconverter, and (g) average SM capacitor voltages of phases a, b, and c in the pc-subconverter.

CHAPTER 9

CONCLUSION AND FUTURE WORK

In this chapter, the contributions of this research are summarized and future work is discussed.

9.1 Conclusions

The main contributions and conclusions of this work are:

• The proposed sliding mode control-based control method is capable of increasing the dynamic response speed without degrading the noise immunity;

• The proposed optimized thermal-loading control method reduces the total power losses and unequal power loss distribution of the semiconductor devices simultaneously;

• The proposed clustering algorithm-based method effectively detects open-circuit faults in the active switches of the MMC;

• The proposed neutral shift-based fault-tolerant control method for the DC-AC MMC is capable of maximizing the output line-to-line voltages and the power transfer capability, subsequent to bypassing the faulty SMs;

• The proposed fault-tolerant control methods for the AC-AC MMC under both an external line-to-ground fault and internal SM faults are capable of guaranteeing proper operation of the AC-AC MMC as close as possible to its normal one;

• The proposed hybrid topology for the DC-AC MMC is capable of operating under low-frequency conditions, eliminating the injected high-frequency common-mode voltage, and reducing the magnitude of the injected high-frequency currents.

• The proposed MMC-based partially-rated solid-state transformer along with its supporting control strategies is capable of conditioning the power in the grid and maintaining the capacitor voltages balanced.

9.2 Future Work

The research presented in the dissertation is potential to be improved from the following aspects:

• Stability of the MMC and its interaction with its surroundings under different control methods need to be analyzed further;

• The behaviors of the MMC subsequent to an open-circuit fault need to be explored to prevent the open-circuit fault make any secondary damage to the MMC;

• The hardware and software-based fault-tolerant strategies for the MMC and the MMC-connceted systems, e.g., HVDC, MV drive, need to be explored further;

• The proposed hybrid topologies of the MMC can be improved to remove the common-mode voltage of the load and decrease the number of devices further, and more hybrid topologies could be explored to solve the operational challenges associated with low-frequency conditions.

Appendices

APPENDIX A

K-MEANS CLUSTERING ALGORITHM IN CHAPTER 4

Algorithm 1 is the pseudo code of K-means clustering algorithm, where $O^{x,j}$ is the set of vectors for the SMs within the upper or lower arm of phase j; $C_{\zeta}^{x,j}(\nu)$ is ζ-th cluster at the ν-th iteration.

Algorithm 1 K-means Clustering Algorithm

Input:

Set $K^{x,j} =$ the expected number of clusters;

$O^{x,j} = \{\mathbf{o}^{x1,j}, \mathbf{o}^{x2,j}, \ldots, \mathbf{o}^{xN,j}\}$;

Iteration:

$\nu = 1$;

repeat

for all i **do**

for all ζ **do**

calculate $d\left(\mathbf{o}^{xi,j}, \mathbf{c}_{\zeta}^{x,j}\right)$ based on (4.6);

end for

end for

for all i **do**

$p = \arg\min_{\zeta}\{d\left(\mathbf{o}^{xi,j}, \mathbf{c}_{\zeta}^{x,j}\right)\}$;

$C_{p}^{x,j}(\nu) \leftarrow C_{p}^{x,j}(\nu) \cup \{\mathbf{o}^{xi,j}\}$;

end for

for all ζ **do**

calculate $\mathbf{c}_{\zeta}^{x,j}$ based on (4.5);

end for

$\nu \leftarrow \nu + 1$;

until $C_{\zeta}^{x,j}(\nu - 1) = C_{\zeta}^{x,j}(\nu)$, for all ζ;

Output: $C_{\zeta}^{x,j}(\zeta = 1, \cdots, K)$;

REFERENCES

[1] S. Debnath, J. Qin, B. Bahrani, M. Saeedifard, and P. Barbosa, "Operation, control, and applications of the modular multilevel converter: A review," *IEEE Trans. Power Electron.*, vol. 30, no. 1, pp. 37–53, 2015.

[2] G. Kish, M. Ranjram, and P. Lehn, "A modular multilevel DC/DC converter with fault blocking capability for HVDC interconnects," *IEEE Trans. Power Electron.*, vol. 30, no. 1, pp. 148–162, 2015.

[3] W. Kawamura, K.-L. Chen, M. Hagiwara, and H. Akagi, "A low-speed, high-torque motor drive using a modular multilevel cascade converter based on triple-star bridge cells (MMCC-TSBC)," *IEEE Trans. Ind. Appl.*, vol. 51, no. 5, pp. 3965–3974, 2015.

[4] S. Allebrod, R. Hamerski, and R. Marquardt, "New transformerless, scalable modular multilevel converters for HVDC-transmission," in *Proc. IEEE Electronics Specialists Conf.*, 2008, pp. 174–179.

[5] J. Dorn, H. Huang, and D. Retzmann, "Novel voltage-sourced converters for HVDC and FACTS applications," in *Conf. Cigre Symposium Osaka*, 2007.

[6] B. Gemmell, J. Dorn, D. Retzmann, and D. Soerangr, "Prospects of multilevel VSC technologies for power transmission," in *Proc. IEEE Transmission and Distribution Conf. Expo.*, Paris, 2008.

[7] R. Marquardt, "Modular multilevel converter: An universal concept for HVDC-networks and extended DC-bus-applications," in *International Power Electronics Conf.*, Paris, 2010.

[8] M. Saeedifard and R. Iravani, "Dynamic performance of a modular multilevel back-to-back HVDC system," *IEEE Trans. Power Del.*, vol. 25, no. 4, pp. 2903–2912, 2010.

[9] S. Rohner, S. Bernet, M. Hiller, and R. Sommer, "Modulation, losses, and semiconductor requirements of modular multilevel converters," *IEEE Trans. Ind. Electron.*, vol. 57, no. 8, pp. 2633–2642, 2010.

[10] M. A. Perez, S. Bernet, J. Rodriguez, S. Kouro, and R. Lizana, "Circuit topologies, modeling, control schemes, and applications of modular multilevel converters," *IEEE Trans. Power Electron.*, vol. 30, no. 1, pp. 4–17, 2015.

[11] A. Nami, J. Liang, F. Dijkhuizen, and G. D. Demetriades, “Modular multilevel converters for hvdc applications: Review on converter cells and functionalities,” *IEEE Trans. Power Electron.*, vol. 30, no. 1, pp. 18–36, 2015.

[12] P. Bakas, L. Harnefors, S. Norrga, A. Nami, K. Ilves, F. Dijkhuizen, and H. P. Nee, “A review of hybrid topologies combining line-commutated and cascaded full-bridge converters,” *IEEE Trans. Power Electron.*, vol. 32, no. 10, pp. 7435–7448, 2017.

[13] G. P. Adam, I. A. Gowaid, S. J. Finney, D. Holliday, and B. W. Williams, “Review of dc-dc converters for multi-terminal HVDC transmission networks,” *IET Power Electron.*, vol. 9, no. 2, pp. 281–296, 2016.

[14] Z. Zhao, K. Li, Y. Jiang, S. Lu, and L. Yuan, “Overview on reliability of modular multilevel cascade converters,” *Chinese Journal of Electrical Engineering*, vol. 1, no. 1, pp. 37–49, 2015.

[15] Q. Tu, Z. Xu, and L. Xu, “Reduced switching-frequency modulation and circulating current suppression for modular multilevel converters,” *IEEE Trans. Power Del.*, vol. 26, no. 3, pp. 2009–2017, 2011.

[16] S. Debnath and M. Saeedifard, “A new hybrid modular multilevel converter for grid connection of large wind turbines,” *IEEE Trans. Sust. Energy*, vol. 4, no. 4, pp. 1051–1064, 2013.

[17] L. Harnefors, A. Antonopoulos, S. Norrga, L. Angquist, and H.-P. Nee, “Dynamic analysis of modular multilevel converters,” *IEEE Trans. Ind. Electron.*, vol. 60, no. 7, pp. 2526–2537, 2013.

[18] X. She, A. Huang, X. Ni, and R. Burgos, “Ac circulating currents suppression in modular multilevel converter,” in *Proc. Conf. IEEE Ind. Electron. Soc.*, 2012, pp. 191–196.

[19] M. Vasiladiotis, N. Cherix, and A. Rufer, “Accurate capacitor voltage ripple estimation and current control considerations for grid-connected modular multilevel converters,” *IEEE Trans. Power Electron.*, vol. 29, no. 9, pp. 4568–4579, 2014.

[20] B. Bahrani, S. Debnath, and M. Saeedifard, “Circulating current suppression of the modular multilevel converter in a double-frequency rotating reference frame,” *IEEE Trans. Power Electron.*, vol. 31, no. 1, pp. 783–792, 2016.

[21] A. J. Korn, M. Winkelnkemper, and P. Steimer, “Low output frequency operation of the modular multi-level converter,” in *Proc. IEEE Energy Convers. Congr. Expo.*, 2010, pp. 3993–3997.

[22] M. Hagiwara, I. Hasegawa, and H. Akagi, "Start-up and low-speed operation of an electric motor driven by a modular multilevel cascade inverter," *IEEE Trans. Ind. Appl.*, vol. 49, no. 4, pp. 1556–1565, 2013.

[23] K. Wang, Y. Li, Z. Zheng, and L. Xu, "Voltage balancing and fluctuation-suppression methods of floating capacitors in a new modular multilevel converter," *IEEE Trans. Ind. Electron.*, vol. 60, no. 5, pp. 1943–1954, 2013.

[24] A. Antonopoulos, L. Angquist, S. Norrga, K. Ilves, L. Harnefors, and H. P. Nee, "Modular multilevel converter AC motor drives with constant torque from zero to nominal speed," *IEEE Trans. Ind. Appl.*, vol. 50, no. 3, pp. 1982–1993, 2014.

[25] S. Debnath, J. Qin, and M. Saeedifard, "Control and stability analysis of modular multilevel converter under low-frequency operation," *IEEE Trans. Ind. Appl.*, vol. 62, no. 9, pp. 5329–5339, 2015.

[26] S. Debnath, J. Qin, B. Bahrani, M. Saeedifard, and P. Barbosa, "Operation, control, and applications of the modular multilevel converter: A review," *IEEE Trans. Power Electron.*, vol. 30, no. 1, pp. 37–53, 2015.

[27] K. Sharifabadi, L. Harnefors, H.-P. Nee, S. Norrga, and R. Teodorescu, "Dynamics and control," in *Design, Control and Application of Modular Multilevel Converters for* HVDC *Transmission Systems*. Wiley-IEEE Press, 2016, pp. 133–213, ISBN: 9781118851555.

[28] R. Teodorescu, F. Blaabjerg, M. Liserre, and P. C. Loh, "Proportional-resonant controllers and filters for grid-connected voltage-source converters," *Proc. IEE EPA*, vol. 153, no. 5, pp. 750–762, 2006.

[29] G. Konstantinou, J. Pou, S. Ceballos, R. Picas, J. Zaragoza, and V. G. Agelidis, "Control of circulating currents in modular multilevel converters through redundant voltage levels," *IEEE Trans. Power Electron.*, vol. 31, no. 11, pp. 7761–7769, 2016.

[30] X. Shi, Z. Wang, B. Liu, Y. Liu, L. M. Tolbert, and F. Wang, "Characteristic investigation and control of a modular multilevel converter-based HVDC system under single-line-to-ground fault conditions," *IEEE Trans. Power Electron.*, vol. 30, no. 1, pp. 408–421, 2015.

[31] J. Qin and M. Saeedifard, "Predictive control of a modular multilevel converter for a back-to-back HVDC system," *IEEE Trans. Power Del.*, vol. 27, no. 3, pp. 1538–1547, 2012.

[32] M. Vatani, B. Bahrani, M. Saeedifard, and M. Hovd, "Indirect finite control set model predictive control of modular multilevel converters," *IEEE Trans. Smart Grid*, vol. 6, no. 3, pp. 1520–1529, 2015.

[33] B. S. Riar, T. Geyer, and U. K. Madawala, "Model predictive direct current control of modular multilevel converters: Modeling, analysis, and experimental evaluation," *IEEE Trans. Power Electron.*, vol. 30, no. 1, pp. 431–439, 2015.

[34] L. Ben-Brahim, A. Gastli, M. Trabelsi, K. A. Ghazi, M. Houchati, and H. Abu-Rub, "Modular multilevel converter circulating current reduction using model predictive control," *IEEE Trans. Ind. Electron.*, vol. 63, no. 6, pp. 3857–3866, 2016.

[35] G. Bergna, A. Garces, E. Berne, P. Egrot, A. Arzande, J. C. Vannier, and M. Molinas, "A generalized power control approach in ABC frame for modular multilevel converter HVDC links based on mathematical optimization," *IEEE Trans. Power Del.*, vol. 29, no. 1, pp. 386–394, 2014.

[36] H. Barnklau, A. Gensior, and J. Rudolph, "A model-based control scheme for modular multilevel converters," *IEEE Trans. Ind. Electron.*, vol. 60, no. 12, pp. 5359–5375, 2013.

[37] L. Harnefors, A. Antonopoulos, K. Ilves, and H. P. Nee, "Global asymptotic stability of current-controlled modular multilevel converters," *IEEE Trans. Power Electron.*, vol. 30, no. 1, pp. 249–258, 2015.

[38] S. Yang, P. Wang, and Y. Tang, "Feedback linearization based current control strategy for modular multilevel converters," *IEEE Trans. Power Electron.*, vol. PP, no. 99, pp. 1–1, 2017.

[39] K. Ma, M. Liserre, F. Blaabjerg, and T. Kerekes, "Thermal loading and lifetime estimation for power device considering mission profiles in wind power converter," *IEEE Trans. on Power Electron.*, vol. 30, no. 2, pp. 590–602, 2015.

[40] S. Yang, A. Bryant, P. Mawby, D. Xiang, L. Ran, and P. Tavner, "An industry-based survey of reliability in power electronic converters," *IEEE Trans. on Ind. Appl.*, vol. 47, no. 3, pp. 1441–1451, 2011.

[41] J. Due, S. Munk-Nielsen, and R. Nielsen, "Lifetime investigation of high power IGBT modules," in *Proc. IEEE EPE*, 2011, pp. 1–8.

[42] J. Berner, "Load-cycling capability of hipak IGBT modules," in *ABB Application Note 5SYA 2043-02*, 2012.

[43] K. Wang, Y. Li, Z. Zheng, and L. Xu, "Voltage balancing and fluctuation-suppression methods of floating capacitors in a new modular multilevel converter," *IEEE Trans. on Ind. Electron.*, vol. 60, no. 5, pp. 1943–1954, 2013.

[44] M. Andresen, M. Liserre, and G. Buticchi, “Review of active thermal and lifetime control techniques for power electronic modules,” in *Proc. IEEE EPE*, 2014, pp. 1–10.

[45] L. Popova, J. Pyrhonen, K. Ma, and F. Blaabjerg, “Device loading of modular multilevel converter MMC in wind power application,” in *Proc. IEEE ECCE ASIA*, 2014, pp. 548–554.

[46] H. Liu, K. Ma, Z. Qin, P. C. Loh, and F. Blaabjerg, “Lifetime estimation of MMC for offshore wind power HVDC application,” *IEEE J. Sel. Topics in Power Electron.*, vol. 4, no. 2, pp. 504–511, 2016.

[47] M. K. Bakhshizadeh, K. Ma, P. C. Loh, and F. Blaabjerg, “Indirect thermal control for improved reliability of modular multilevel converter by utilizing circulating current,” in *Proc. Appl. Power Electron. Conf. and Expo.*, 2015, pp. 2167–2173.

[48] U.-M. Choi, F. Blaabjerg, and K.-B. Lee, “Study and handling methods of power IGBT module failures in power electronic converter systems,” *IEEE Trans. Power Electron.*, vol. 30, no. 5, pp. 2517–2533, 2015.

[49] H. Oh, B. Han, P. McCluskey, C. Han, and B. Youn, “Physics-of-failure, condition monitoring, and prognostics of insulated gate bipolar transistor modules: A review,” *IEEE Trans. Power Electron.*, vol. 30, no. 5, pp. 2413–2426, 2015.

[50] T.-J. Kim, W.-C. Lee, and D.-S. Hyun, “Detection method for open-circuit fault in neutral-point-clamped inverter systems,” *IEEE Trans. Ind. Electron.*, vol. 56, no. 7, pp. 2754–2763, 2009.

[51] B. Mirafzal, “Survey of fault-tolerance techniques for three-phase voltage source inverters,” *IEEE Trans. Ind. Electron.*, vol. 61, no. 10, pp. 5192–5202, 2014.

[52] N. Freire, J. Estima, and A. Marques Cardoso, “Open-circuit fault diagnosis in PMSG drives for wind turbine applications,” *IEEE Trans. Ind. Electron.*, vol. 60, no. 9, pp. 3957–3967, 2013.

[53] B. Lu and S. Sharma, “A literature review of IGBT fault diagnostic and protection methods for power inverters,” *IEEE Trans. Ind. Appl.*, vol. 45, no. 5, pp. 1770–1777, 2009.

[54] R. de Araujo Ribeiro, C. Jacobina, E. Cabral da Silva, and A. Lima, “Fault detection of open-switch damage in voltage-fed PWM motor drive systems,” *IEEE Trans. Power Electron.*, vol. 18, no. 2, pp. 587–593, 2003.

[55] P. Lezana and G. Ortiz, “Extended operation of cascade multicell converters under fault condition,” *IEEE Trans. Ind. Electron.*, vol. 56, no. 7, pp. 2697–2703, 2009.

[56] S. Khomfoi and L. Tolbert, "Fault diagnosis and reconfiguration for multilevel inverter drive using AI-based techniques," *IEEE Trans. Ind. Electron.*, vol. 54, no. 6, pp. 2954–2968, 2007.

[57] S. Shao, P. Wheeler, J. Clare, and A. Watson, "Fault detection for modular multilevel converters based on sliding mode observer," *IEEE Trans. Power Electron.*, vol. 28, no. 11, pp. 4867–4872, 2013.

[58] F. Deng, Z. Chen, M. Khan, and R. Zhu, "Fault detection and localization method for modular multilevel converters," *IEEE Trans. Power Electron.*, vol. 30, no. 5, pp. 2721–2732, 2015.

[59] P. Lezana, J. Pou, T. Meynard, J. Rodriguez, S. Ceballos, and F. Richardeau, "Survey on fault operation on multilevel inverters," *IEEE Trans. Ind. Electron.*, vol. 57, no. 7, pp. 2207–2218, 2010.

[60] B. Lu and S. Sharma, "A literature review of IGBT fault diagnostic and protection methods for power inverters," in *in Proc. IEEE IAS Annu. Meet. Ind. Appl. Conf.*, 2008, pp. 1–8.

[61] B. Li, S. Shi, B. Wang, G. Wang, W. Wang, and D. Xu, "Fault diagnosis and tolerant control of single IGBT open-circuit failure in modular multilevel converters," *IEEE Trans. Power Electron.*, vol. PP, no. 99, pp. 1–1, 2015.

[62] G. T. Son, H.-J. Lee, T. S. Nam, Y.-H. Chung, U.-H. Lee, S.-T. Baek, K. Hur, and J.-W. Park, "Design and control of a modular multilevel HVDC converter with redundant power modules for noninterruptible energy transfer," *IEEE Trans. Power Del.*, vol. 27, no. 3, pp. 1611–1619, 2012.

[63] G. Konstantinou, J. Pou, S. Ceballos, and V. Agelidis, "Active redundant submodule configuration in modular multilevel converters," *IEEE Trans. Power Del.*, vol. 28, no. 4, pp. 2333–2341, 2013.

[64] P. Hu, D. Jiang, Y. Zhou, Y. Liang, J. Guo, and Z. Lin, "Energy-balancing control strategy for modular multilevel converters under submodule fault conditions," *IEEE Trans. Power Electron.*, vol. 29, no. 9, pp. 5021–5030, 2014.

[65] P. Hammond, "Enhancing the reliability of modular medium-voltage drives," *IEEE Trans. Ind. Electron.*, vol. 49, no. 5, pp. 948–954, 2002.

[66] J. Rodriguez, P. Hammond, J. Pontt, R. Musalem, P. Lezana, and M.-J. Escobar, "Operation of a medium-voltage drive under faulty conditions," *IEEE Trans. Ind. Electron.*, vol. 52, no. 4, pp. 1080–1085, 2005.

[67] F. Carnielutti, H. Pinheiro, and C. Rech, "Generalized carrier-based modulation strategy for cascaded multilevel converters operating under fault conditions," *IEEE Trans. Ind. Electron.*, vol. 59, no. 2, pp. 679–689, 2012.

[68] D. Busse, J. Erdman, R. J. Kerkman, D. Schlegel, and G. Skibinski, "System electrical parameters and their effects on bearing currents," *IEEE Trans. Ind. Appl.*, vol. 33, no. 2, pp. 577–584, 1997.

[69] A. Antonopoulos, L. Angquist, L. Harnefors, and H. P. Nee, "Optimal selection of the average capacitor voltage for variable-speed drives with modular multilevel converters," *IEEE Trans. Power Electron.*, vol. 30, no. 1, pp. 227–234, 2015.

[70] S. Du, B. Wu, K. Tian, N. R. Zargari, and Z. Cheng, "An active cross-connected modular multilevel converter (AC-MMC) for a medium-voltage motor drive," *IEEE Trans. Ind. Electron.*, vol. 63, no. 8, pp. 4707–4717, 2016.

[71] S. Du, B. Wu, and N. Zargari, "Common-mode voltage elimination for variable-speed motor drive based on flying-capacitor modular multilevel converter," *IEEE Trans. Power Electron.*, vol. PP, no. 99, pp. 1–1, 2017.

[72] S. Du, B .WU, and N. Zargari, "A star-channel modular multilevel converter for zero/low fundamental frequency operation without injecting common-mode voltage," *IEEE Trans. Power Electron.*, 2017.

[73] S. Du, B. Wu, and N. Zargari, "A delta-channel modular multilevel converter for zero/low-fundamental-frequency operation," *IEEE Trans. Ind. Electron.*, 2017.

[74] B. Li, S. Zhou, D. Xu, S. J. Finney, and B. W. Williams, "A hybrid modular multilevel converter for medium-voltage variable-speed motor drives," *IEEE Trans. Power Electron.*, vol. 32, no. 6, pp. 4619–4630, 2017.

[75] W. Kawamura and H. Akagi, "Control of the modular multilevel cascade converter based on triple-star bridge-cells (MMCC-TSBC) for motor drives," in *Proc. IEEE Energ. Convers. Congr. Expo.*, 2012, pp. 3506–3513.

[76] F. Kammerer, J. Kolb, and M. Braun, "A novel cascaded vector control scheme for the modular multilevel matrix converter," in *Proc. Conf. IEEE Ind. Electron. Soc.*, 2011, pp. 1097–1102.

[77] F. Kammerer, M. Gommeringer, J. Kolb, and M. Braun, "Energy balancing of the modular multilevel matrix converter based on a new transformed arm power analysis," in *Proc. EPE*, 2014, pp. 1–10.

[78] M. Vasiladiotis, N. Cherix, and A. Rufer, "Operation and control of single-to-three-phase direct AC/AC modular multilevel converters under asymmetric grid conditions," in *Proc. IEEE Int. Power Electron. Conf.*, 2015, pp. 1061–1066.

[79] A. Korn, M. Winkelnkemper, P. Steimer, and J. Kolar, "Direct modular multi-level converter for gearless low-speed drives," in *Proc. EPE*, 2011, pp. 1–7.

[80] W. Kawamura, M. Hagiwara, and H. Akagi, "A broad range of frequency control for the modular multilevel cascade converter based on triple-star bridge-cells (MMCC-TSBC)," in *Proc. IEEE Energ. Convers. Congr. Expo.*, 2013, pp. 4014–4021.

[81] W. Kawamura, Y. Chiba, M. Hagiwara, and H. Akagi, "Experimental verification of tsbc-based electrical drives when the motor frequency is passing through, or equal to, the supply frequency," in *Proc. IEEE Energ. Convers. Congr. Expo.*, 2015, pp. 5490–5497.

[82] E. R. Ronan, S. D. Sudhoff, S. F. Glover, and D. L. Galloway, "A power electronic-based distribution transformer," *IEEE Trans. Power Del.*, vol. 17, no. 2, pp. 537–543, 2002.

[83] T. Zhao, G. Wang, S. Bhattacharya, and A. Q. Huang, "Voltage and power balance control for a cascaded h-bridge converter-based solid-state transformer," *IEEE Trans. Power Electron.*, vol. 28, no. 4, pp. 1523–1532, 2013.

[84] J. E. Huber and J. W. Kolar, "Applicability of solid-state transformers in today and future distribution grids," *IEEE Trans. Smart Grid*, pp. 1–1, 2017.

[85] E. C. Aeloiza, P. N. Enjeti, L. A. Moran, and I. Pitel, "Next generation distribution transformer: To address power quality for critical loads," in *Proc. IEEE PESC*, vol. 3, 2003, pp. 1266–1271.

[86] S. Bala, D. Das, E. Aeloiza, A. Maitra, and S. Rajagopalan, "Hybrid distribution transformer: Concept development and field demonstration," in *Proc. IEEE ECCE*, 2012, pp. 4061–4068.

[87] J. Burkard and J. Biela, "Evaluation of topologies and optimal design of a hybrid distribution transformer," in *Proc. IEEE EPE*, 2015, pp. 1–10.

[88] J. Kaniewski, Z. Fedyczak, and G. Benysek, "Ac voltage sag/swell compensator based on three-phase hybrid transformer with buck-boost matrix-reactance chopper," *IEEE Trans. Ind. Electron.*, vol. 61, no. 8, pp. 3835–3846, 2014.

[89] P. Szczesniak and J. Kaniewski, "Hybrid transformer with matrix converter," *IEEE Trans. Power Del.*, vol. 31, no. 3, pp. 1388–1396, 2016.

[90] N. Yousefpoor, B. Parkhideh, A. Azidehak, S. Bhattacharya, and B. Fardanesh, "Modular transformer converter-based convertible static transmission controller for transmission grid management," *IEEE Trans. Power Electron.*, vol. 29, no. 12, pp. 6293–6306, 2014.

[91] T. Kang, S. Choi, A. S. Morsy, and P. N. Enjeti, "Series voltage regulator for a distribution transformer to compensate voltage sag/swell," *IEEE Trans. Ind. Electron.*, vol. 64, no. 6, pp. 4501–4510, 2017.

[92] J. Sastry and S. Bala, "Considerations for the design of power electronic modules for hybrid distribution transformers," in *Proc. IEEE ECCE*, 2013, pp. 1422–1428.

[93] V. I. Utkin, "Sliding mode control design principles and applications to electric drives," *IEEE Trans. Ind. Electron.*, vol. 40, no. 1, pp. 23–36, 1993.

[94] S. C. Tan, Y. M. Lai, and C. K. Tse, "General design issues of sliding-mode controllers in DC-DC converters," *IEEE Trans. Ind. Electron.*, vol. 55, no. 3, pp. 1160–1174, 2008.

[95] D. Ludois and G. Venkataramanan, "Simplified terminal behavioral model for a modular multilevel converter," *IEEE Trans. Power Electron.*, vol. 29, no. 4, pp. 1622–1631, 2014.

[96] Q. Tu and Z. Xu, "Impact of sampling frequency on harmonic distortion for modular multilevel converter," *IEEE Trans. Power Del.*, vol. 26, no. 1, pp. 298–306, 2011.

[97] J. Qin and M. Saeedifard, "Reduced switching-frequency voltage-balancing strategies for modular multilevel HVDC converters," *IEEE Trans. Power Del.*, vol. 28, no. 4, pp. 2403–2410, 2013.

[98] Y. Li, E. A. Jones, and F. Wang, "The impact of voltage-balancing control on switching frequency of the modular multilevel converter," *IEEE Trans. Power Electron.*, vol. 31, no. 4, pp. 2829–2839, 2016.

[99] A. Yazdani and R. Iravani, "Grid-imposed frequency vsc system: Control in dq-frame," in *Voltage-Sourced Converters in Power Systems:Modeling, Control, and Applications*. Wiley-IEEE Press, 2010, pp. 204–244, ISBN: 9780470551578.

[100] M. Hagiwara and H. Akagi, "Control and experiment of pulsewidth-modulated modular multilevel converters," *IEEE Trans. Power Electron.*, vol. 24, no. 7, pp. 1737–1746, 2009.

[101] S. Sudhoff, "Genetic optimization system engineering tool (GOSET) 2.6. (2014)," 2014.

[102] Q. Tu, Z. Xu, and L. Xu, "Reduced switching-frequency modulation and circulating current suppression for modular multilevel converters," *IEEE Trans. on Power Del.*, vol. 26, no. 3, pp. 2009–2017, 2011.

[103] S. Theodoridis and K. Koutroumbas, "Chapter 14 - clustering algorithms iii: Schemes based on function optimization," in *Pattern Recognition (Fourth Edition)*, S. Theodoridis and K. Koutroumbas, Eds., Fourth Edition, Boston: Academic Press, 2009, pp. 701 –763, ISBN: 978-1-59749-272-0.

[104] A. Yazdani and R. Iravani, "A unified dynamic model and control for the voltage-sourced converter under unbalanced grid conditions," *IEEE Trans. Power Del.*, vol. 21, no. 3, pp. 1620–1629, 2006.

[105] Y. Zhou, D. Jiang, J. Guo, P. Hu, and Y. Liang, "Analysis and control of modular multilevel converters under unbalanced conditions," *IEEE Trans. Power Del.*, vol. 28, no. 4, pp. 1986–1995, 2013.

[106] A. Yazdani and R. Iravani, "A unified dynamic model and control for the voltage-sourced converter under unbalanced grid conditions," *IEEE Trans. Power Del.*, vol. 21, no. 3, pp. 1620–1629, 2006.

[107] W. Kawamura, M. Hagiwara, and H. Akagi, "Control and experiment of a modular multilevel cascade converter based on triple-star bridge cells," *IEEE Trans. Ind. Appl.*, vol. 50, no. 5, pp. 3536–3548, 2014.

[108] T. Nakamori, M. A. Sayed, Y. Hayashi, T. Takeshita, S. Hamada, and K. Hirao, "Independent control of input current, output voltage, and capacitor voltage balancing for a modular matrix converter," *IEEE Trans. Ind. Appl.*, vol. 51, no. 6, pp. 4623–4633, 2015.

[109] N. Thitichaiworakorn, M. Hagiwara, and H. Akagi, "Experimental verification of a modular multilevel cascade inverter based on double-star bridge cells," *IEEE Trans. Ind. Appl.*, vol. 50, no. 1, pp. 509–519, 2014.

[110] "United states electricity industry primer," Office of Electricity Delivery and Energy Reliability, U.S. Department of Energy, Tech. Rep., 2015.